The Astrophysical Journal, 853:191 (30pp), 2018 February 1 https://doi.org/10.3847/1538-4357/aaa3dc

Hubble Space Telescope Wide Field Camera 3 Observations of Escaping Lyman Continuum Radiation from Galaxies and Weak AGN at Redshifts $z \sim 2.3$–4.1

Brent M. Smith[1], Rogier A. Windhorst[1], Rolf A. Jansen[1], Seth H. Cohen[1], Linhua Jiang[1,2], Mark Dijkstra[3], Anton M. Koekemoer[4], Richard Bielby[5], Akio K. Inoue[6], John W. MacKenty[4], Robert W. O'Connell[7], and Joseph I. Silk[8]
[1] School of Earth & Space Exploration, Arizona State University, Tempe, AZ 85287-1404, USA; Brent.Smith.1@asu.edu
[2] Kavli Institute for Astronomy and Astrophysics, Peking University, Beijing 100871, People's Republic of China
[3] Institute of Theoretical Astrophysics, University of Oslo, Postboks 1029, NO-0858 Oslo, Norway
[4] Space Telescope Science Institute, Baltimore, MD 21218, USA
[5] University of Durham, South Road, Durham DH1 3LE, UK
[6] Osaka Sangyo University, Osaka, Japan
[7] Department of Astronomy, University of Virginia, Charlottesville, VA 22904-4325, USA
[8] The Johns Hopkins University, Baltimore, MD 21218, USA
Received 2016 February 3; revised 2017 December 15; accepted 2017 December 18; published 2018 February 5

Abstract

We present observations of escaping Lyman Continuum (LyC) radiation from 34 massive star-forming galaxies (SFGs) and 12 weak AGN with reliably measured spectroscopic redshifts at $z \simeq 2.3$–4.1. We analyzed *Hubble Space Telescope* (*HST*) Wide Field Camera 3 (WFC3) mosaics of the Early Release Science (ERS) field in three UVIS filters to sample the rest-frame LyC over this redshift range. With our best current assessment of the WFC3 systematics, we provide 1σ upper limits for the average LyC emission of galaxies at $\langle z\rangle = 2.35$, 2.75, and 3.60 to ~28.5, 28.1, and 30.7 mag in image stacks of 11–15 galaxies in the WFC3/UVIS F225W, F275W, and F336W, respectively. The LyC flux of weak AGN at $\langle z\rangle = 2.62$ and 3.32 are detected at 28.3 and 27.4 mag with S/Ns of ~2.7 and 2.5 in F275W and F336W for stacks of 7 and 3 AGN, respectively, while AGN at $\langle z\rangle = 2.37$ are constrained to $\gtrsim$27.9 mag at 1σ in a stack of 2 AGN. The stacked AGN LyC light profiles are flatter than their corresponding non-ionizing UV continuum profiles out to radii of $r \lesssim 0\farcs9$, which may indicate a radial dependence of porosity in the ISM. With synthetic stellar SEDs fit to UV continuum measurements longward of Lyα and IGM transmission models, we constrain the absolute LyC escape fractions to $f_{\rm esc}^{\rm abs} \simeq 22^{+44}_{-22}\%$ at $\langle z\rangle = 2.35$ and $\lesssim$55% at $\langle z\rangle = 2.75$ and 3.60, respectively. All available data for galaxies, including published work, suggests a more sudden increase of $f_{\rm esc}$ with redshift at $z \simeq 2$. Dust accumulating in (massive) galaxies over cosmic time correlates with increased H I column density, which may lead to reducing $f_{\rm esc}$ more suddenly at $z \lesssim 2$. This may suggest that SFGs collectively contributed to maintaining cosmic reionization at redshifts $z \gtrsim$ 2–4, while AGN likely dominated reionization at $z \lesssim 2$.

Key words: cosmology: observations – dark ages, reionization, first stars – galaxies: active – galaxies: statistics – intergalactic medium – ultraviolet: galaxies

1. Introduction

At the end of the cosmic dark ages, radiation emitted by the first luminous objects in the universe began to reionize the intergalactic medium (IGM). The far-ultraviolet (FUV) ionizing radiation, specifically the Lyman continuum (LyC; $\lambda \leqslant 912$ Å), emitted by massive stars in the first star-forming galaxies (SFGs), or accretion disks around supermassive black holes in early active galactic nuclei (AGNs), may have initiated the epoch of cosmic reionization (e.g., Madau et al. 2004). Additional sources of LyC radiation and high-energy particles within galaxies, such as high mass X-ray binaries, galactic outflows/inflows and superwinds, accretion onto dark matter halos, massive pre-galactic Pop III stars, and young globular clusters may have contributed to the reionization of the IGM as well (e.g., Ricotti 2002; Sternberg et al. 2002; Mirabel et al. 2011; Kulkarni et al. 2014). This LyC radiation would have formed bubbles of ionized hydrogen around these UV bright galaxies, which then expanded and merged until the IGM became completely ionized (e.g., Gnedin 2000; MiraldaEscudé et al. 2000; Loeb & Barkana 2001; Fan et al. 2002). This phase transition of the neutral IGM began somewhere in the epoch $z \simeq$ 10–20 (Hinshaw et al. 2013; Ade et al. 2014; Planck Collaboration et al. 2016), and completed when the IGM was fully ionized by $z \simeq 6$ (Mesinger & Haiman 2004; Fan et al. 2006a, 2006b; Schroeder et al. 2012; McGreer et al. 2014; Becker et al. 2015). Observations of Lyα emitting galaxies also favor (volume averaged) neutral fractions in excess of $\langle x_{\rm H\,I}\rangle > 0.3$ at $z \sim 7$ (e.g., Dijkstra et al. 2011; Jensen et al. 2012; Mesinger et al. 2014; Choudhury et al. 2015).

Because neutral hydrogen and dust are opaque to FUV radiation, LyC photons can only escape from galaxies in regions where the surrounding H I column density, $N_{\rm H}$, and dust extinction are low. Thus, in order for a fraction of the produced LyC photons to escape ($f_{\rm esc}$), the interstellar medium (ISM) in the galaxy and its surrounding circumgalactic medium must be cleared. This can be accomplished by supernova winds (Fujita et al. 2003), which can also suppress the formation of low mass stars and increase the formation of LyC-producing high mass stars, and can be further enhanced by AGN outflows (Silk & Norman 2009). High star formation rates (SFRs) can also increase the porosity of the ISM (Clarke & Oey 2002). Semi-analytical models of Dove et al. (2000) show that LyC emitted by OB associations can become trapped in superbubbles until they expand outside of the disk. Once the surrounding medium is either cleared or fully ionized, it

becomes transparent to LyC radiation, which can then escape through these regions of the galaxy, or be Thomson scattered by free electrons and/or dust. The escaping LyC can then be observed along some lines of sight, which can be distributed randomly in a galaxy, and is, in some cases, offset from the galactic center (e.g., Iwata et al. 2009; Vanzella et al. 2010a, 2012).

Stacks of ground-based spectra have shown that AGN produce more LyC than star-forming Lyman Break Galaxies (LBG; Vanden Berk et al. 2001; Shapley et al. 2003), though LBGs selected via drop-out techniques may have fainter LyC emission due to their selection compared to other UV bright SFGs (Vanzella et al. 2015). Rest-frame UV spectra of AGN taken with *HST* and the *Far-Ultraviolet Spectroscopic Explorer* (*FUSE*; Moos et al. 2000) have shown significant detections of escaping LyC flux at $0.5 \lesssim z \lesssim 2.5$ (e.g., Telfer et al. 2002; Scott et al. 2004; Shull et al. 2012; Lusso et al. 2015), but only upper limits of $f_{\rm esc} \lesssim 1$–2% from galaxies at the same redshifts (e.g., Bridge et al. 2010; Siana et al. 2010; Rutkowski et al. 2016; Sandberg et al. 2015). AGN contributed the majority of LyC photons to the ionizing background from their peak epoch at $z \simeq 2$ until today, and maintain the ionized state of the IGM (Cowie et al. 2009). However, because AGN are much more rare than galaxies, and their space density decreases at $z \gtrsim 2$ (Silverman et al. 2008; Ebrero et al. 2009; Aird et al. 2015), AGN likely did not reionize the IGM at $z \gtrsim 3$ (Willott et al. 2010; Glikman et al. 2011; Masters et al. 2012), though they are believed to be the only sources responsible for He II reionization at $z \simeq 3$ (Haardt & Madau 2012; Worseck et al. 2016). Therefore, SFGs are regarded as the most likely candidates that started the reionization of the IGM at $z \gtrsim 6$ (but see, e.g., Madau & Haardt 2015).

Since higher IGM opacity at $z \gtrsim 6$ prevents a direct study of LyC emission from SFGs at this epoch, we must study lower redshift analogs in order to understand the sources of reionization of the IGM. Despite many attempts, rest-frame FUV observations of SFGs at $0.5 \lesssim z \lesssim 2.5$ have so far not yielded significant detections of escaping LyC flux (e.g., Ferguson 2001; Giallongo et al. 2002; Fernández-Soto et al. 2003; Malkan et al. 2003; Inoue et al. 2005; Siana et al. 2007, 2010; Cowie et al. 2009; Bridge et al. 2010; Rutkowski et al. 2016; Sandberg et al. 2015; Grazian et al. 2016; Guaita et al. 2016). Ground-based spectra (Steidel et al. 2001; Shapley et al. 2006; Cooke et al. 2014; de Barros et al. 2016) and optical narrow-band and broadband imaging of SFGs at $3 \lesssim z \lesssim 4$ (Iwata et al. 2009; Vanzella et al. 2010a, 2012; Boutsia et al. 2011; Nestor et al. 2011, 2013; Mostardi et al. 2013) have revealed evidence for escaping LyC photons along several sight lines, with $f_{\rm esc} \simeq 1\%$–40% despite higher IGM opacities at these higher redshifts (Haardt & Madau 1996, 2012). Furthermore, Vanzella et al. (2012) estimate $f_{\rm esc}$ for one LBG (GDS J033216.64−274253.3 at $z = 3.795$) to be >25%, although ground-based measurements of escaping LyC may be contaminated with non-ionizing flux from blended lower redshift foreground interlopers due to the lower resolution of ground-based seeing (Vanzella et al. 2010b; Nestor et al. 2013; Mostardi et al. 2015; Siana et al. 2015). Spectroscopy of gamma-ray burst afterglows from $2 < z < 8$ have also been used to constrain $f_{\rm esc}$ to <6% at these redshifts (Chen et al. 2007; Fynbo et al. 2009; Wyithe et al. 2010).

Observations of some local starburst galaxies have shown significant, yet varying $f_{\rm esc}$ values (Leitherer et al. 1995; Hurwitz et al. 1997; Tumlinson et al. 1999; Deharveng et al. 2001; Heckman et al. 2001; Borthakur et al. 2014; Izotov et al. 2016), although Hanish et al. (2010) find that local starburst galaxies do not exhibit higher escape fractions compared to ordinary local SFGs. H II regions in nearby galaxies have been observed to release 40%–75% of the LyC photons produced by massive stars into the local IGM (Ferguson et al. 1996; Leitherer et al. 1996; Oey & Kennicutt 1997; Zurita et al. 2002). In the local group, Bland-Hawthorn & Maloney (1999) and Putman et al. (2003) find LyC escape fractions of only 1%–2%.

In the hierarchical formation scenario of galaxy assembly, the inflow of cold gas and merging of high redshift compact galaxies plays a role in the formation of massive young starburst galaxies. The number density of those Luminous Compact Blue Galaxies is also known to increase strongly with redshift (Lilly et al. 1998; Mallén-Ornelas et al. 1999). *FUSE* observations of analogous nearby, young, starbursting dwarf galaxies have shown that the $f_{\rm esc}$ values of these galaxies reach $\lesssim$4%, and can collectively contribute a significant fraction to the ionizing background at high redshift (Bergvall et al. 2006; Grimes et al. 2007, 2009; Leitet et al. 2011, 2013). Most theoretical models also predict that low mass galaxies abundant at high redshifts are more likely to have higher $f_{\rm esc}$ values than the larger galaxies at low to moderate redshift (Razoumov & Sommer-Larsen 2010; Yajima et al. 2011; Wise et al. 2014). Hence, it is likely that different classes of objects dominated reionization at different cosmic epochs, i.e., the combined FUV output from (dwarf) SFGs may have started to reionize the IGM at $z \gtrsim 6.5$–7, then, along with more massive galaxies, completed and maintained its ionized state at $z \lesssim 6$ until AGN started to dominate at FUV wavelengths at $z \lesssim 2$–2.5.

In this work, we describe our analysis of *HST* rest-frame UV observations of LyC escaping from massive SFGs and weak AGN at $z \simeq 2.3$–4.1 in three UVIS filters with the Wide Field Camera 3 (WFC3), taken shortly after installation onto *HST*. We compare the measured LyC fluxes of our sample to their modeled intrinsic LyC fluxes using stellar population synthesis models and Monte Carlo (MC) simulated line of sight IGM transmission models.

This paper is organized as follows. In Section 2, we describe the data that we used for our analysis and how it was reduced. In Section 3 we give our assessment of the available spectra for our galaxy samples and their reliability and completeness. In Section 4, we outline the method we implemented to create the stacked LyC images of our samples of galaxies, how we perform photometry on the stacks, the observed LyC flux that we measure, and the significance of these detections. In Section 5, we introduce the stacked LyC escape fraction, how we calculated the $f_{\rm esc}$ values, their implications, and the observed and modeled radial profiles of the escaping LyC from our samples. In Sections 6 and 7, we discuss our results and present our conclusions. We use Planck (Planck Collaboration et al. 2016) cosmology throughout: $H_0 = 67.8\,{\rm km\,s^{-1}\,Mpc^{-1}}$, $\Omega_m = 0.308$ and $\Omega_\Lambda = 0.692$. All flux densities (referred to as "fluxes" throughout) quoted are in the AB magnitude system (Oke & Gunn 1983), unless stated otherwise.

2. WFC3/UVIS and ACS/WFC Observations and Data Reduction

2.1. ERS/GOODS-S WFC3/UVIS and ACS/WFC Data

Our UV data was taken with *HST*'s WFC3/UVIS camera in the Early Release Science (ERS) field in September 2009

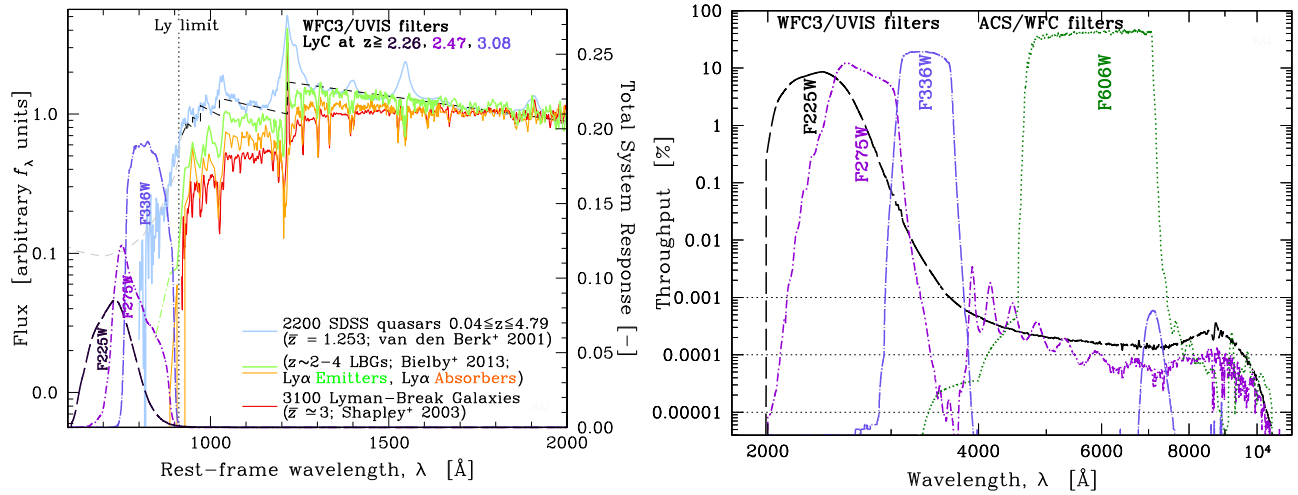

Figure 1. (a) Example composite rest-frame FUV spectra of SDSS QSOs at $\langle z \rangle \sim 1.3$ (Vanden Berk et al. 2001 (blue)) and of LBGs at $z \simeq 2$–4 (Bielby et al. 2013 (green and orange); Shapley et al. 2003 (red)). The WFC3/UVIS F225W, F275W, and F336W filter transmission curves are ideally positioned to capture Lyman continuum emission ($\lambda < 912$ Å) at $z \geqslant 2.26$, $z \geqslant 2.47$, and $z \geqslant 3.08$, respectively. The combined SEDs of SDSS QSOs suggest a strong LyC signal, whereas the SEDs of LBGs suggest fainter LyC flux. (b) Total system throughput curves (observed wavelengths) of the same WFC3/UVIS and ACS/WFC filters (Avila et al. 2015; Dressel et al. 2015) are shown on a logarithmic scale to emphasize their out of band transmission ("red-leak"). These WFC3 UVIS filters were designed to simultaneously maximize throughput and minimize such red-leaks. In Appendix B.1 we assess the percentage of non-ionizing UVC flux with $\lambda > 912$ Å leaking in the filter. We include the ACS/WFC F606W filter as a UVC filter reference.

Table 1
Summary of *HST* WFC3/UVIS Images and Image Stacks in the ERS Field

Filter	$\lambda/\Delta\lambda$[a]	$z_{\rm LyC}$[b]	Obs. Date	$t_{\rm exp}$[c]	PSF[d]	SB(obs)[e]
F225W	2359/467	2.26–2.47	2009 Sep 7–11	5,688	0.″087	29.80
F275W	2704/398	2.47–3.08	2009 Sep 7–11	5,688	0.″087	29.82
F336W	3355/511	3.08–4.35	2009 Sep 7–12	2,778	0.″088	29.76

Notes.
[a] Central wavelength/bandwidth of filter in Å.
[b] Redshift range over which rest-frame LyC emission can in principle be sampled. The high end of each bin occurs at the redshift where the next redder filter can better sample LyC emission at the same or higher redshift.
[c] Average integration time of the mosaics in seconds.
[d] Typical stellar PSF FWHM.
[e] Measured 1σ surface brightness sensitivity limit of our mosaics for a source of uniform SB in a 2.″00 diameter aperture in AB mag arcsec^{-2} (see W11 and Table 4 in Appendix A).

(Windhorst et al. 2011, hereafter W11), less than four months after Shuttle Servicing Mission SM4 that installed WFC3 onto *HST*, at a point when the WFC3/UVIS CCDs have not yet suffered from significant CTE degradation. Complementary optical ACS/WFC data was taken in 2002 July–2003 May as part of the Great Observatories Origins Deep Survey (GOODS; Dickinson et al. 2003). Figures 1(a) and (b) show the WFC3/UVIS F225W, F275W, and F336W filter transmission curves, which are ideally positioned to capture LyC emission with negligible red-leak at $z \gtrsim 2.26$, $z \gtrsim 2.47$, and $z \gtrsim 3.08$, respectively (see Appendix B.1 for a detailed discussion on red-leak). The corresponding rest-frame non-ionizing ultraviolet continuum (UVC) imaging of our galaxies were taken with ACS/WFC in the F606W, F606W, and F775W, respectively. These filters sample rest-frame $\lambda_{\rm eff} \sim$ 1400–1800 Å for each of our redshift intervals. When we model the rest-frame UVC absolute magnitudes ($M_{\rm AB}$) from the spectral energy distribution (SED) fits, we integrate over the interval 1500 ± 100 Å (see Section 5.1). We also utilized photometry from WFC3/IR F098M, F125W, and F160W imaging in the ERS field (W11) and CANDELS WFC3/IR F105W, F125W, and F160W (Grogin et al. 2011; Koekemoer et al. 2011) photometric catalogs in GOODS-South (Guo et al. 2013) for object selection and SED fitting (see Sections 3.1 and 5.1).

Table 1 summarizes the data in the ERS and GOODS South fields available for studying LyC emission, and the redshift range over which each of these filters can sample LyC emission with negligible contamination from non-ionizing flux. Each lower redshift bound was carefully chosen such that *no* light with $\lambda > 912$ Å is sampled below the filter's red edge (defined at 0.5% of the filter's peak transmission, as tabulated in Dressel et al. (2015) and references therein). The upper redshift bound of each bin in Table 1 occurs at the redshift where the next redder filter can trace LyC emission more sensitively. Figure 1(a) suggests that the observed escaping LyC emission strongly declines toward shorter wavelengths. For this reason, the broadband filters we use are most sensitive to LyC emission at the low redshift end of each of the three redshift ranges of Table 1.

2.2. Image Calibration, Drizzling and Astrometric Accuracy

The photometric and astrometric calibration and drizzling of the ACS/WFC mosaics are described in Giavalisco et al. (2004). The

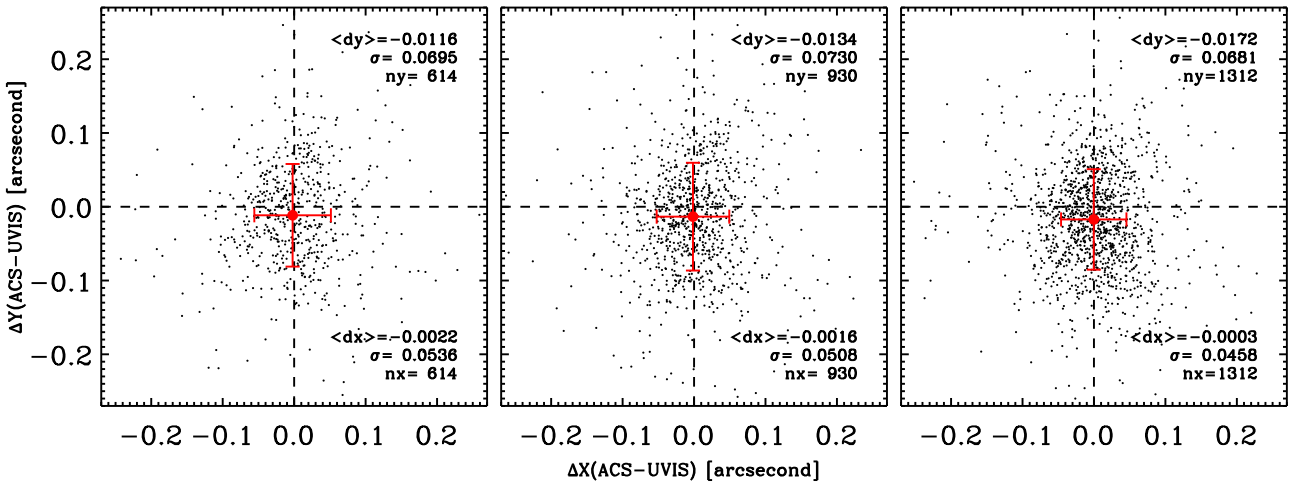

Figure 2. Residual astrometric errors in the improved WFC3/UVIS ERS mosaics in F225W (left), F275W (middle), and F336W (right), respectively, as measured relative to the ACS/WFC F435W ERS mosaic. The new WFC3/UVIS geometric distortion corrections provided a significantly improved registration of all eight WFC3/UVIS tiles to the ACS/WFC F435W mosaics compared to the 2009 ERS mosaics of W11. The measured residual systematic offsets are $\langle \Delta X \rangle \lesssim 0\farcs0022$ and $\langle \Delta Y \rangle \lesssim 0\farcs0172$ compared to ACS (indicated by the dashed lines), and random deviations less than $0\farcs054$ in X and $0\farcs073$ in Y.

initial astrometric calibration of the WFC3/UVIS ERS mosaics, described in W11, left systematic offsets between individual WFC3 CCDs of up to ∼5 drizzled pixels (∼0.″5) compared to the GOODS v2.0[9] F435W mosaics, especially at the edges of each UVIS mosaic tile (see Appendix A of W11). These offsets occurred in part due to the way the ERS UVIS exposures were taken, but were primarily due to the rather uncertain geometric instrument distortion correction (IDC) tables available at the time (Kozhurina-Platais et al. 2009). The lack of UV bright astrometric reference sources in the shallow (∼900–1400 s) individual exposures further prevented accurate registration and drizzling of the F225W, F275W, and F336W images. This issue was resolved with the improved IDC Tables of Kozhurina-Platais et al. (2013) and Kozhurina-Platais (2014). Using these new IDC tables, we re-drizzled the UVIS ERS images into mosaics at a plate scale of $0\farcs03\ \mathrm{pix}^{-1}$.

Figure 2 shows the residual astrometric errors of the new ERS mosaics (which we refer to as ERS "v2.0") for the F225W, F275W, and F336W filters, measured relative to the ACS/WFC F435W mosaics. Residual systematic offsets from the ACS/WFC F435W GOODS v2.0 mosaics for the 8 WFC3/UVIS ERS tiles are now measured to be $\langle \Delta X \rangle \lesssim 0\farcs0022$ (0.024 pix) and $\langle \Delta Y \rangle \lesssim 0\farcs0172$ (0.19 pix), with 1σ random deviations less than $0\farcs054$ (0.60 pix) in X and $0\farcs073$ (0.81 pix) in Y. Any remaining systematic astrometric offsets are at the sub-pixel level, and are sufficiently small that they no longer affect our SB sensitivity to LyC flux, nor do they add contamination from neighboring sources that can potentially blend in with the LyC signal due to astrometric uncertainties.

2.3. WFC3/UVIS Residual Sky-background

The original ground-based WFC3/UVIS thermal vacuum flats left residual gradients and patterns in the sky-background at the 5%–10% level (Sabbi 2009; W11). For the reprocessing of the ERS data, we use the flat-fields from Mack et al. (2013), which include on-orbit "delta-flat" corrections to the ground-based thermal vacuum flat-fields, significantly reducing the large-scale flat-field patterns seen in earlier ERS mosaics.

[9] http://archive.stsci.edu/pub/hlsp/goods/v2/h_goods_v2.0_rdm.html

W11 measured zodiacal sky-background SB levels in the ERS of 25.46, 25.64, and 24.82 mag arcsec^{-2} in the WFC3/UVIS F225W, F275W, and F336W respectively. When drizzling the data, this sky-background is subtracted (see Koekemoer et al. 2013). For the 5688, 5688, and 2788 s total exposure times in these filters, this corresponds to a subtraction of ∼0.00219, 0.00202, and $0.00704\ e^-/0\farcs09$ pixel. To determine the best fit *residual* sky-background level across the WFC3/UVIS ERS mosaics, we follow Freedman & Diaconis (1981), who define the sampled bin width for optimal histogram fitting as $2 \times \mathrm{IQR} \times N^{-1/3}$, where IQR is the inner quartile range of the pixel distribution (i.e., the range within 75% and 25%, or $\pm 1.349\sigma/2$ for a Gaussian distribution), and N is the total number of pixels used in the image to construct that histogram. We fit the logarithm of the sky pixel histogram between -3σ and $+1\sigma$ to a Gaussian function by least squares to obtain the peak value of the fitted functions.

Figure 3 shows the sky pixel histograms and best fit *residual* sky-background levels in the WFC3/UVIS F225W, F275W, and F336W ERS mosaics of W11 in black, while the red curves and measurements indicate the best fit to the data in the current, improved v2.0 mosaics. The slight narrowing of the negative tail of the Gaussian noise distributions in the new mosaics reflects the better flat-fielding. Our best fit *residual* sky-background values and uncertainties thereon are $(2.62 \pm 0.09) \times 10^{-5}$, $(3.71 \pm 0.10) \times 10^{-5}$, and $(31.94 \pm 0.18) \times 10^{-5}\ e^-/\mathrm{s}$ in the F225W, F275W, and F336W filters, respectively, which corresponds to residual sky SB levels of 30.29, 29.99, and 28.15 mag arcsec^{-2} left in the UVIS images *after* drizzling, which subtracted the sky-background to first order. Compared to the observed ERS sky-backgrounds measured in W11, these residual sky SB level values are 4.84, 4.35, and 3.33 mag fainter than the UV sky (1.2%, 1.8%, 4.7% of the UV sky), respectively. These residual sky-background levels can be accurately determined locally and subsequently subtracted, which we employed in our sub-image stacking technique to further increase our sensitivity to extended, low SB LyC signal (see Section 4.1).

3. Spectroscopic Redshifts and Sample Selection

3.1. Spectroscopic Sample Selection

In order to obtain accurate estimates of LyC escape fractions as low as $f_{\mathrm{esc}} \lesssim 1.0\%$, we must require the interloper fraction

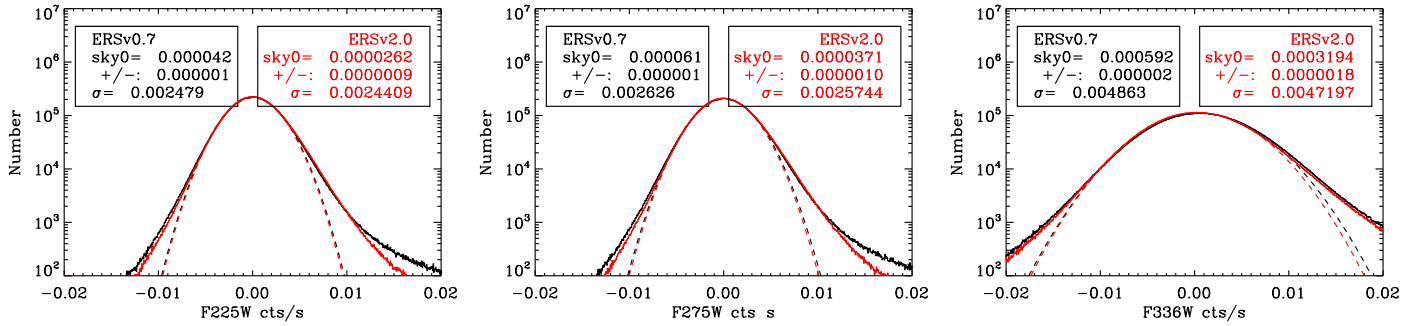

Figure 3. Residual sky-background levels in the drizzled WFC3/UVIS ERS mosaics in the F225W (left), F275W (middle), and F336W (right) filters, determined as described in Section 2.3. The best fit to the 2009 ERS mosaics of W11 ("v0.7") is shown in black, while the improved mosaics discussed here ("v2.0") are shown in red. Dashed lines show Gaussian fits to the two histograms. Each panel lists the best fit *residual sky-background level* (in ADU/sec), equivalent to 30.29, 29.99, and 28.15 mag arcsec^{-2}, respectively, and the uncertainties thereon across the entire WFC3 ERS mosaic.

to be very small. Thus, any potentially contaminating, low redshift, interloping galaxies that might create a false-positive LyC signal must be identified and removed from our sample. We therefore require each galaxy that we include in our analysis to have a highly reliable spectroscopic redshift.

Several wide field ground-based spectroscopic surveys have been performed in the GOODS fields, including the ERS region, at low and high redshift with the Very Large Telescope (VLT) (e.g., Cristiani et al. 2000; Le Fèvre et al. 2004, 2015; Szokoly et al. 2004; Wolf et al. 2004; Vanzella et al. 2008; Popesso et al. 2009; Wuyts et al. 2009; Balestra et al. 2010; Silverman et al. 2010; Fiore et al. 2011; Kurk et al. 2012; Tasca et al. 2017) as well as *HST* (Momcheva et al. 2016). We retrieved the reduced one-dimensional FITS spectral data from the ESO archives[10] along with their corresponding 3D-*HST* grism spectra[11] for galaxies at $z \geqslant 2.26$ in order to verify the designated redshifts of these galaxies. We plotted each spectrum at both the original spectral resolution and smoothed with a $\sigma = 3$ Å Gaussian convolution kernel to reduce the noise in the spectrum for inspection. Typical spectral emission or absorption features for SFGs and AGN were indicated, and portions of the spectra around these features were magnified for closer examination. Specifically, these emission or absorption features include the Lyman Break at 912 Å, Lyα 1216 Å, Si II 1260 Å, O I 1304 Å, C II 1335 Å, Si IV 1398 Å, C IV 1549 Å, and C III] 1909 Å, and when present, C II] 2326 Å, Fe II 2344 Å, and sometimes N V 1240 Å, Fe II 2600 Å, Mg II 2798 Å, O II 3727 Å, [Ne III] 3869 Å, He II 4686 Å, H β 4861 Å, and [O III] 4959+5007 Å. In addition, we included high contrast cutout images of the galaxies in the filter sampling the rest-frame LyC emission, and all available longer wavelength filters for inspection and removal of contaminating objects.

Five of us (B.M.S., R.A.W., S.H.C., R.A.J., and L.J.) visually inspected all spectra and unanimously selected the highest quality spectra available from the spectroscopic surveys and composed our spectroscopic sample of galaxies and AGN. We found that including objects with spectra that had less reliable redshifts improved our formal signal-to-noise ratio (S/N), but likely added contaminating flux rather than true escaping LyC flux. Hence, we *only* included galaxies with the highest quality spectra that coincided with their predicted emission/absorption lines exactly.

[10] http://archive.eso.org/, http://www.eso.org/sci/activities/garching/projects/goods/MasterSpectroscopy.html, and http://cesam.lam.fr/vuds/DR1/

[11] http://3dhst.research.yale.edu/Home.html

Note that 12 of the 46 objects in our spectroscopic sample are galaxies hosting a *weak* AGN, as evidenced by the (broad) emission lines in their spectra, for example Lyα, N V, Si IV, C IV, He II, C III], and Mg II. We also cross-correlated the positions of our galaxy sample with *Chandra* 4 Ms and Very Large Array 1.4 GHz source catalogs to identify possible obscured/type II AGN using their radio/X-ray luminosities and photon indices (e.g., Xue et al. 2011; Fiore et al. 2012; Miller et al. 2013; Rangel et al. 2013; Xue et al. 2016). We identified five of the 12 galaxies hosting AGN from their X-ray emission. In our analysis, we will consider the subsamples of 34 galaxies without AGN signatures, and 12 galaxies with weak AGN, both separately and combined. A list of the galaxies in our sample can be found in Table 4 of Appendix D.

3.2. Completeness and Representativeness of the Spectroscopic Samples

Initially, our sample of galaxies was limited to those with *known* spectroscopic redshifts. Our selection of galaxies with high quality spectra in GOODS-S, which solely determined which objects were included in our analysis, reduced our sample to galaxies that can be observed with ground-based spectroscopy at a high S/N. This, of course, can bias our results and their subsequent interpretations, e.g., if $f_{\rm esc}$ is a strong function of luminosity ($M_{\rm AB}$), dust extinction (A_V), metallicity, and/or age. We therefore must consider how representative the characteristics of our selected galaxy samples are in order to understand differences in the results of our analyses of the populations.

In Figure 4, we plot the distribution of observed apparent magnitudes ($m_{\rm AB}$), and the corresponding absolute magnitudes ($M_{\rm AB}$) of the rest-frame non-ionizing UVC flux ($\lambda_{\rm eff} = 1500 \pm 100$ Å) of our samples. We consider all galaxies (Figure 4(a)), galaxies hosting weak AGN (Figure 4(b)), and galaxies without AGN (Figure 4(c)). These values were derived from the apparent flux of the galaxies at the same rest-frame wavelengths, using their best fit SED models (see Section 5.1 and Appendix D.1), so no k-correction is necessary to directly compare the $M_{\rm AB}$ values of the galaxies at various redshifts.

If the spectroscopic samples were complete, their apparent magnitude distributions would resemble the galaxy count distributions of the full V and i band mosaics (Giavalisco et al. 2004; W11) to a given AB magnitude limit, since these filters sample the UVC emission indicated in Figure 4, and because the spectroscopic samples were r band or i band selected. Their $M_{\rm AB}$ distribution would also reflect the galaxy

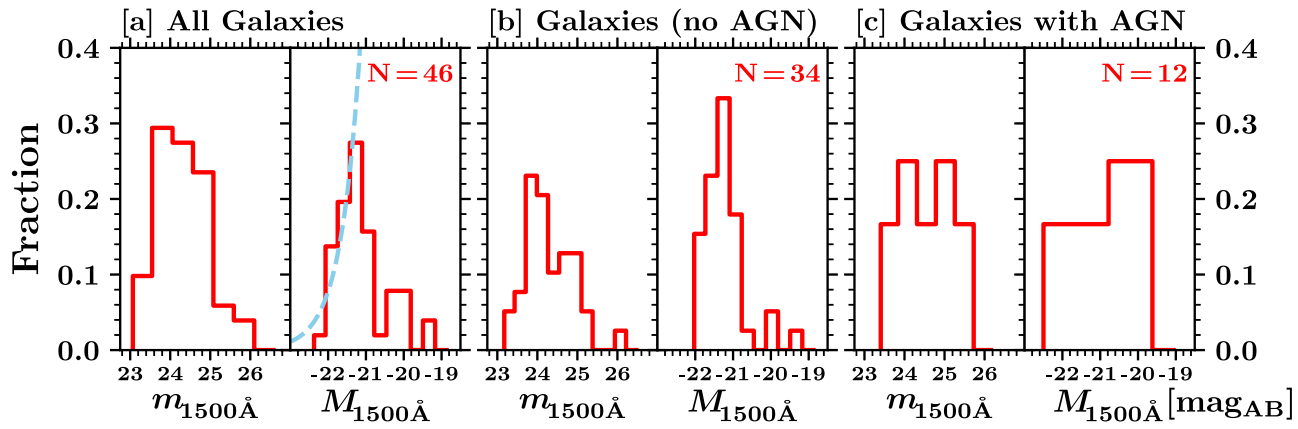

Figure 4. (a) Absolute and apparent magnitude distributions at the rest-frame 1500 ± 100 Å of the spectroscopic samples for all galaxies. (b) Same as panel (a), for just the galaxies without AGN activity. (c) Same as panel (a), for galaxies with indications of AGN activity. These magnitudes were derived from the observed SED fits (see Section 5.1), and therefore do not require k-corrections. The blue dashed curve indicates the slope of the luminosity function of $\langle z \rangle = 3.46$ galaxies at $M_{AB} = -20.8$, equal to 0.84 dex/mag.

UV luminosity function slope at their effective M_{AB} to the effective completeness limits at these redshifts, which typically sample rest-frame wavelengths $\lambda_{eff} \simeq 1500 - 1700$ Å (e.g., Reddy & Steidel 2009; Finkelstein et al. 2015).

It is clear from Figure 4 that our spectroscopically selected samples are incomplete for $m_{AB} \gtrsim 24.0$ mag, both for galaxies with and without weak AGN. For $m_{AB} \lesssim 24.0$ mag, the distributions are consistent with the expected slope of the galaxy counts from W11, so the selected samples may be representative for LyC studies, but only for these brighter fluxes. We also note that our selection of galaxies with high S/N spectra will have favored the broad emission lines of (weak) AGN, and Lyα emission or strong absorption line galaxies, while LBGs and other galaxies without prominent spectroscopic features are less likely to have yielded the highly reliable redshifts required to be included in our highest fidelity sample, even for $m_{AB} \lesssim 24.0$ mag.

The UVC luminosities of the galaxies in our sample span $-22.2 \lesssim M_{AB} \lesssim -19.0$ mag, with an average of $M_{AB} \simeq -21.1^{+0.9}_{-0.5}$ mag (1σ), indicative of predominantly luminous galaxies about as bright as M^* at $2.5 \lesssim z \lesssim 4$ (e.g., Hathi et al. 2010), or of galaxies hosting *weak* AGN. Since this is the only sample for which reliable redshifts currently exist, this is strictly the only luminosity range over which the measurements and analyses of any escaping LyC emission that follows will be valid. These galaxies may also be more luminous than galaxies that contributed to reionization at $z > 7$ (e.g., Bouwens et al. 2012).

Our sample also does not fully sample the parameter space of the age, stellar mass, SFR, and A_V values for galaxies at these redshifts, indicated by their SED fits (see Section 5.1). These biases are also more prominent in the individual redshift subsamples. Figure 5 shows the distribution of these parameters for the spectroscopic sample of galaxies without AGN. These galaxies more or less evenly sample the mass and SFR distribution, which are are generally quite massive and indicative of active star formation, with masses ranging from $\sim 10^{9.5}$–$10^{10.9}$ ($\langle \text{mass} \rangle = 10^{10.2 \pm 0.3} M_\odot$) and SFRs from $\sim 10^{0.8}$–$10^{3.1}$ ($\langle \text{SFR} \rangle = 10^{1.5 \pm 0.4} M_\odot$ yr^{-1}, respectively. Their ages and A_V distributions range from $\sim 10^{7.7}$–$10^{9.4}$ years ($\langle t_{age} \rangle \simeq 10^{8.2^{+0.9}_{-0.4}}$ years) and $A_V = 0.0$–0.8 mag ($\langle A_V \rangle_{med} \simeq 0.3 \pm 0.3$ mag), respectively. We note that the variation in these parameters from sample to sample is most likely due to the selection of the spectroscopic sample, rather than any real correlation in redshift, as the higher redshift galaxies were generally selected in the redder ACS filters.

The incomplete sampling of these various parameters should be taken into account when interpreting the f_{esc} values for these individual subsamples. In order to obtain a more representative sample of galaxies in each redshift bin, we must include more galaxies that sample the full range of these parameters at their respective redshifts, with average parameters that reflect the true averages for all galaxies at these redshifts, and probe fainter luminosities. This should be a focus of future deeper spectroscopic surveys, either from the ground or with *JWST*.

4. LyC Emission Stacking and Photometry

4.1. Sub-image Stacking for each LyC Filter

Since absolute LyC escape fractions have been measured to be very low, and the detected LyC emission is very faint or not detected at all at $z \lesssim 3$ (e.g., Steidel et al. 2001; Shapley et al. 2006; Iwata et al. 2009; Siana et al. 2010; Mostardi et al. 2013), we apply a technique of sub-image stacking of the *observed* LyC emission from multiple galaxies to increase the total S/N and sensitivity to the faint, potentially low, SB LyC flux from individual galaxies. Stacking LyC emission from galaxies at similar redshifts can be used to quantify the *average* LyC emission from galaxies at their average redshift. This method also reduces small-scale residual systematic errors in the stacked sub-images left from bias, dark current, sky-subtraction, flat-fielding, and/or any gradients from variations in exposure time or photon noise between exposures that might remain in the background of drizzled mosaics, as effects from random systematics are averaged out in a stack (see Appendices A–C). We create our stacks of the LyC emission for our samples as following.

For each galaxy, we extracted 151 × 151 pixel (4.″53 × 4.″53) sub-images from the WFC3/UVIS mosaics in the respective filter that samples the LyC emission of each galaxy. The size of these cutouts provided sufficient sampling of the photon statistics in the sub-images for fitting the pixel count-rate distribution, while minimizing the potential area of neighboring sources of non-ionizing flux. Each sub-image was centered on the R.A. and decl. of the centroid of the individual galaxy indicated in the *3D-HST* photometric catalog (Skelton et al. 2014).

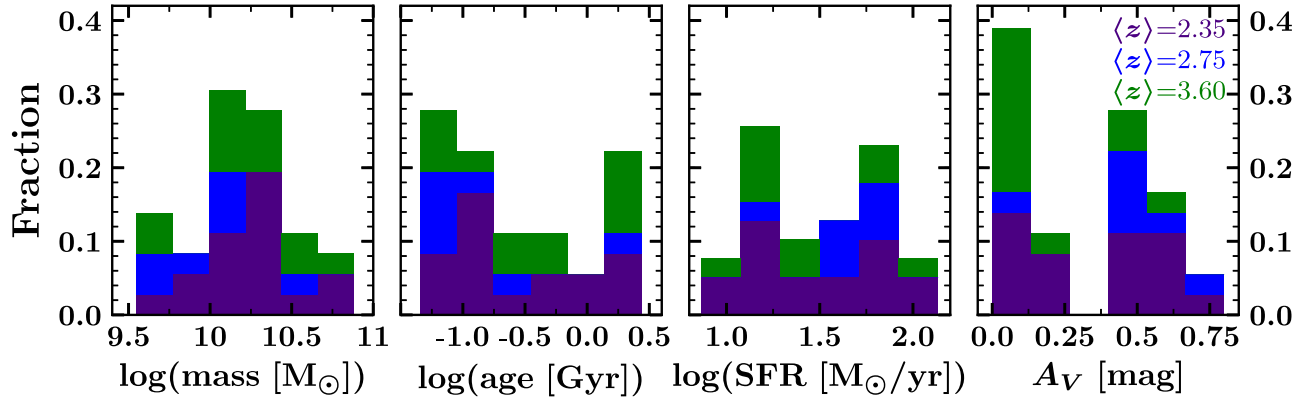

Figure 5. Stacked BC03 SED fit parameter distributions of the spectroscopic samples for galaxies without AGN. The purple, blue, and green bars represent the $\langle z\rangle = 2.35$, $\langle z\rangle = 2.75$, and $\langle z\rangle = 3.60$ samples, respectively.

We then created SExtractor (Bertin & Arnouts 1996) segmentation maps from χ^2 images (Szalay et al. 1999) generated from all available *HST* data for each LyC sub-image in order to identify *all* neighboring objects detected at a $\geqslant 1\sigma$ threshold above the local sky. We then exclude *all* surrounding detections outside of a central circular aperture with a $0\farcs5$ radius ($r \simeq 17$ pix) found in the LyC segmentation maps. We preserve all flux from any objects inside this central aperture when we stack the sub-images, while also excluding those detected on the border of the central aperture. This masking was applied to ensure that all potential sources of non-ionizing flux from lower redshift neighbors along the line of sight are removed before stacking. On average, $\sim 3 \pm 2$ objects were removed from each sub-image. We note that this procedure would not be possible when stacking LyC emission of galaxies using ground-based observations alone, as effects from seeing can blend neighboring non-ionizing contaminants with the true LyC signal (e.g., Nestor et al. 2013; Mostardi et al. 2015; Siana et al. 2015). Each individual masked sub-image was inspected visually to verify that no surrounding objects indeed remained in the sub-images, including those seen only at longer wavelengths in the 10-band ERS mosaics (see Section 2). Thus, it is possible that the rigorous removal of surrounding flux can sometimes result in the removal of more extended (i.e., at $r \geqslant 0\farcs5$) LyC flux from the stacked images if this were detectable at $\geqslant 1\sigma$ above the local sky-background (see Sections 4.3 and 5.4).

We also subtracted a constant from each of the sub-images before object removal in order to bring the mode of the sky-background of the images as close to zero as possible. We calculated the mode of background level from the count-rate histogram of the surrounding pixels outside the central circular aperture, binning their values according to the Freedman–Diaconis rule (see Section 2.3). We then fit each sky histogram to a Gaussian function by least squares, taking the mode of the fitted Gaussian as the background constant. This local sky-background removal was applied in order to sum the actual LyC flux *above* the background from each sub-image, rather than LyC+background, as variations in background levels between sub-images can suppress the flux contribution from the faintest LyC emission in the stack. The subtraction also removed any residual small-scale gradients between the sub-images left from bias/sky-subtraction, flat-fielding, and/or exposure time/noise variations in the mosaics.

We then stacked the processed sub-images of all the galaxies in each UVIS/ACS image with spectroscopic redshifts, where LyC can be observed in their respective filter, using the average of the pixel count rates of the sub-images, weighted by their corresponding AstroDrizzle (Fruchter et al. 2010; Gonzaga et al. 2012) weight maps. We did this by summing the weighted pixel values of the processed sub-images, normalized by the sum of their weights (i.e., $\langle f_j\rangle = \sum_i W_i f_{i,j} / \sum_i W_i$, where f_j represents the flux in counts per second measured in pixel j for sub-image i and W_i is the weight map for sub-image i). We then created stacked weight maps for each LyC stack by summing the inverse of the pixel values of the corresponding region in the weight maps, where the galaxy sub-images were extracted, then inverting the sum to generate the stacked weight maps (i.e., $W_j = 1/\sum_i 1/W_{i,j}$, where W_j is the weight for pixel j in sub-image i). These weight maps give the relative weight of each pixel in the LyC stacks, and are used only for quantifying all photometric errors in the observations. We created stacks for the *total* sample of galaxies and separate stacks for the galaxy and AGN samples, since each sample likely produces the majority of their LyC photons by different mechanisms, which must be taken into account when determining $f_{\rm esc}$ for these galaxies.

Since many $f_{\rm esc}$ values quoted in the literature are calculated relative to the rest-frame non-ionizing UVC flux measured from $1500 \lesssim \lambda_0 \lesssim 1700$ Å (see Section 5.1), we created corresponding UVC stacks for each LyC stack from sub-images extracted from the ACS/WFC mosaics of the ERS/GOODS-S fields that sample the UVC emission of our galaxies. For the redshift intervals that sampled LyC emission in the F225W, F275W, and F336W filters that sample the UVC emission correspond to F606W, F606W, and F775W, respectively.

The galaxies stacked in the WFC3/UVIS F225W filter contain co-added sub-images frames of 19 galaxies over the redshift range $2.276 \leqslant z \leqslant 2.450$ ($\langle z\rangle = 2.352$), the F275W stack contains 14 galaxies at $2.470 \leqslant z \leqslant 3.076$ ($\langle z\rangle = 2.685$), and the F336W stack contains 13 co-added galaxies at $3.132 \leqslant z \leqslant 4.149$ ($\langle z\rangle = 3.537$). These stacks, as well as the corresponding UVC stacks, are shown in Figure 6. Stacks for the subsamples of galaxies with weak AGN and galaxies without AGN are shown in Figures 7 and 8, with elliptical apertures indicating regions where photometry was performed.

The deepest galaxy counts in J and H-band of W11 give us an estimate of the total number of contaminating objects that could be present in our $r \simeq 0\farcs5$ radius LyC apertures (Figures 6–8). To the ERS limit of J, $H \lesssim 27.55$–27.25 mag,

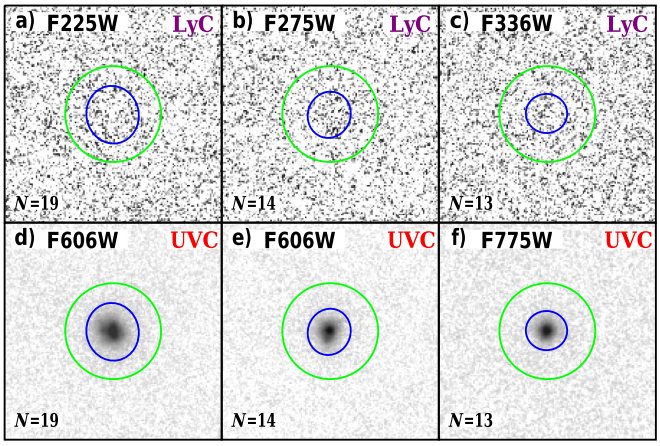

Figure 6. Sub-image stacks for the three different redshift bins in our sample of *all* galaxies, sampling LyC emission in: (a) F225W at $2.28 \leqslant z \leqslant 2.45$, (b) F275W at $2.47 \leqslant z \leqslant 3.08$, and (c) F336W at $3.13 \leqslant z \leqslant 4.15$; and corresponding UVC ($\sim$1400 $\lesssim \lambda_0 \lesssim$ 1800 Å) emission in: (d) F606W, (e) F606W, and (f) F775W. Note that the objects contributing to panels (d) and (e) differ, since they correspond to different redshift bins. Blue ellipses indicate the SExtractor MAG_AUTO UVC detected matched apertures, while green apertures are 2.″0 diameter circles for comparison. All sub-images are 151 × 151 pixels (4.″53 × 4.″53) in size.

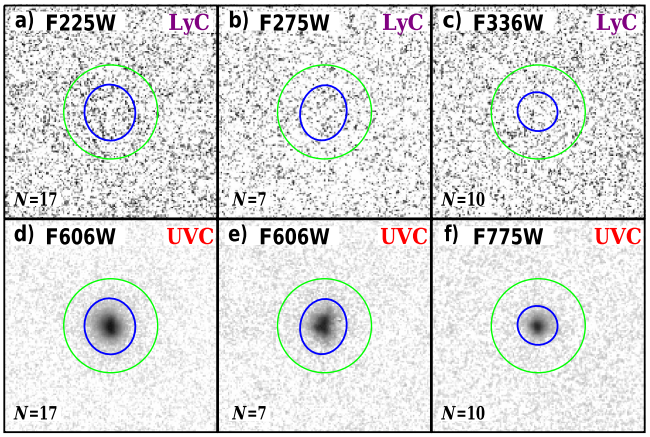

Figure 7. As Figure 6 for galaxies *without* AGN (i.e., no obvious signs of nuclear activity from their spectra or X-ray/radio luminosities/photon indices.

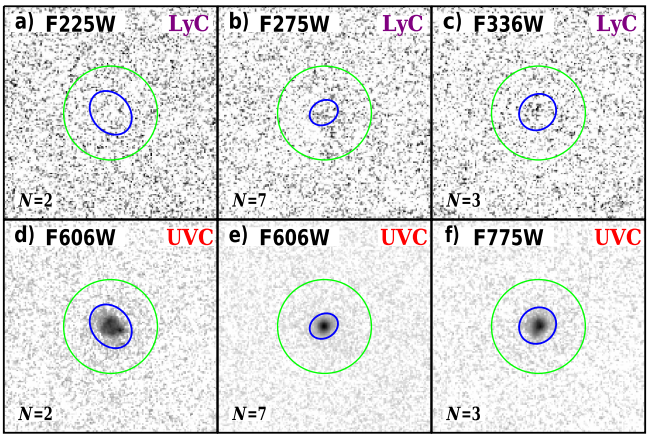

Figure 8. As Figure 6 for only the galaxies hosting weak AGN.

respectively, there are $\lesssim 5.2 \times 10^5$ galaxies deg^{-2} (W11), yielding a $\lesssim$3% probability of finding one unrelated foreground object in, or overlapping with, the LyC aperture. For our sample of 46 galaxies, this would amount to $\lesssim$2 interlopers. Due to the possible interloper's proximity to the LyC candidate, it is not always possible to obtain reliable spectroscopic or photometric redshifts for these neighbors (see Section B.3 for a discussion on contamination from interlopers). Nonetheless, in these few cases, light from the nearby neighbors was masked out with SExtractor segmentation maps. This was then repeated for *all* other objects in the 151 × 151 pixel image sections outside the central $r \simeq 0.''5$ aperture, to exclude contaminating objects in the photometry in the central aperture, and to assure that accurate measurements of the surrounding sky could always be obtained.

4.2. Rest-frame Lyman Continuum Photometry

The results from our photometry measured in the apertures shown in Figures 6–8 are summarized in Table 2. Because the LyC flux escaping from galaxies in these stacks is very faint, we perform all of our photometry on the LyC stacks with SExtractor using detection images in dual-image mode. As our reference images, we use the corresponding non-ionizing UVC stacks to measure any possible escaping LyC flux detectable within the aperture of brighter UVC counterpart.

We used the individual rms maps and the sky-background variance for each sub-image in a given stack to create 10,000 random variations of each pixel for each stack based on the combinations of these uncertainties, in order to assess photometric errors and upper limits. This approach allows us to generate flux distributions of the stack photometry based on systematic uncertainties within the data itself. We measure the flux in the UVC matched aperture for each realization of the stack and plotted them as shown in Figure 9. We quote the mean and 1σ value of the flux distributions in Table 2, or the 1σ value as the upper limit for non-detections. We convert the flux measured by SExtractor to AB magnitudes, using the infinite aperture zero-points listed on the STScI instrument websites.[12]

From these distributions, we measure an average LyC flux from galaxies and AGN at $m_{\rm AB} \simeq 28.11$ mag, with a S/N value at $\sim$2.41 for the F275W stack. We measure 1σ upper bounds of $m_{\rm AB} > 29.02$ and 28.62 mag for the F225W and F336W stacks, respectively. For only the galaxies without AGN (Figure 7), we place 1σ upper bounds for the flux measured in the F225W, F275W, and F336W stacks at $m_{\rm AB} > 27.91$, 28.12, and 30.73 mag, respectively. The flux from galaxies with AGN was measured at $m_{\rm AB} \simeq 28.26$ and 27.42 mag, with S/N $\sim$2.66 and 2.47 for the F275W and F336W stacks, respectively, and we placed a 1σ upper bound to the F225W stack flux at $m_{\rm AB} > 27.91$ mag (see Table 2). Our photometry indicates that the AGN stacks are brighter than galaxies without AGN and have higher S/N, despite having fewer contributing sub-images in the stacks.

We note that, although some LyC flux might exist at the $\sim$1σ level outside the measurement apertures, we do not incorporate this flux into our measurement, as this would require us to increase our aperture size and add extra noise in the aperture, which would increase the uncertainty of our measurements, as well as the interloper contribution.

We performed a series of critical tests on our data to ascertain the robustness and validity of our stacking procedures

[12] http://www.stsci.edu/hst/wfc3/phot_zp_lbn

Table 2
LyC Stack Photometry

Filter (1)	z-range (2)	$\langle z \rangle$ (3)	N_{obj} (4)	m_{LyC} (5)	ABerr$_{LyC}$ (6)	S/N$_{LyC}$ (7)	A_{UVC} (8)	m_{UVC} (9)	S/N$_{UVC}$ (10)
All Galaxies									
F225W	2.276–2.450	2.352	19	>28.26	···	(1.00)†	1.034	24.41	426.7
F275W	2.470–3.076	2.685	14	28.11	0.45	2.41	0.681	24.76	323.8
F336W	3.132–4.149	3.537	13	>28.62	···	(1.00)†	0.553	24.63	247.5
Galaxies without AGN									
F225W	2.276–2.449	2.350	17	>27.91	···	(1.00)†	1.015	24.36	423.8
F275W	2.566–3.076	2.752	7	>28.12	···	(1.00)†	0.932	24.46	268.3
F336W	3.132–4.149	3.603	10	>30.73	···	(1.00)†	0.555	24.75	192.7
Galaxies with AGN									
F225W	2.298–2.450	2.374	2	>27.91	···	(1.00)†	0.637	25.21	85.0
F275W	2.470–2.726	2.618	7	28.26	0.41	2.66	0.253	25.12	232.7
F336W	3.217–3.474	3.316	3	27.42	0.44	2.47	0.486	24.38	158.7

Note. Table columns: (1) WFC3 filter used; (2) redshift range of galaxies included in LyC/UVC stacks; (3) average redshift of stack; (4) number of galaxies with high quality spectroscopic redshifts used in the stacks; (5) observed total AB magnitude of LyC emission from stack (SExtractor MAG_AUTO aperture matched to UVC, indicated by the blue ellipses in Figures 6–8; (6) 1σ error of average LyC AB-mag; (7) measured S/N of the LyC stack flux within matched UVC aperture († indicates a 1σ upper limit); (8) area (in arcsec^2) of the UVC aperture; (9) observed total AB magnitude of the UVC stack; (10) measured S/N of the UVC stack.

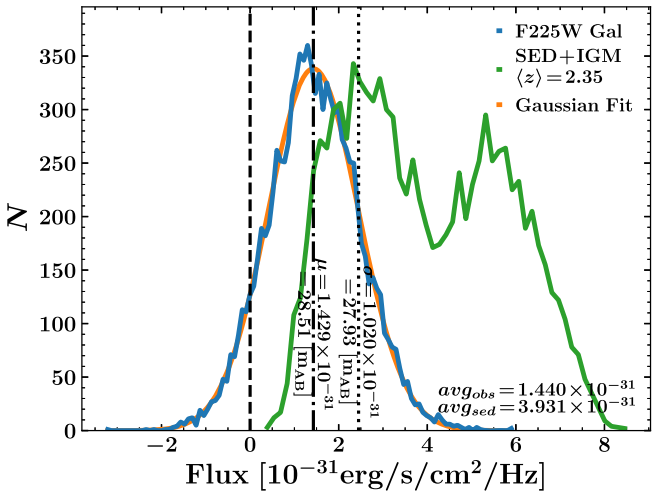

Figure 9. Example flux distribution for the F225W galaxies *without* AGN stack used for our photometric analysis listed in Table 2. Each pixel in the stack was given a mean based on the pixel value in the stacked F225W image, and a variance from the sum of the sky-background variance and the square of the corresponding pixel value in the stacked rms map. The blue distribution was generated by summing the pixel flux distributions inside the blue aperture from Figure 7 for each realization of the stack. The orange line is the Gaussian curve fit to the blue distribution. The mean and $+1\sigma$ values are shown as vertical dash-dot and dotted lines, respectively. The green distribution is the modeled intrinsic flux using the stacked best fit SED convolved with the IGM transmission models of Inoue et al. (2014) and fitting error. The average value of the blue and green distributions is indicated as avg$_{obs}$ and avg$_{sed}$, respectively.

and LyC detections, for which we refer the interested reader to Appendix A. From these tests, we conclude that our measurements are reliable to within their measured errors or upper bounds, and are not the result of various possible sources of spurious signal.

4.3. Super-stacks of LyC Emission from Galaxies at $2.3 \leqslant z \leqslant 4.1$

In order to determine at what S/N our observations can measure the LyC flux from our total sample of galaxies that span the $2.3 \leqslant z \leqslant 4.1$ redshift range, and probe the faintest LyC emission from our galaxies, we construct a stack of the observed LyC flux in f_ν of *all* the galaxies in our sample as follows. We first extract the sub-images from the F225W, F275W, and F336W and apply our sky-subtraction and neighbor masking procedures, as outlined in Section 4.1. We then scale all sub-images in the stack to a common zero-point and stack the sub-images by a weighted average, as described in Section 4.1. We created stacks for the full sample of all galaxies and separate stacks for the galaxies with and without AGN, as shown in Figure 10. We note that these "Super-Stacks" represent the average *observed* LyC flux from our sample integrated from $z = 2.3$–4.1 through the various sight lines, and so the flux in these stacks will be dominated by the galaxies with the brightest apparent LyC flux.

Due to the very low sky-background in the F225W and F275W filters (W11), the relative scaling of the count rates in the sub-images slightly amplified the contribution of detector noise from these filters in the stack. However, since the F336W filter is limited by photon noise from the much brighter zodiacal background at these wavelengths, these "Super-Stacks" therefore also have more significant sky-background. We find that the stack of the total sample reaches a S/N of $\sim 2.3\sigma$, while the LyC stacks of galaxies with and without AGN achieve S/N ratios of 3.9σ and 0.7σ in their UVC matched apertures, respectively. We also find that the average apparent AGN LyC flux outshines that from galaxies without AGN by a factor of $F_\nu^{AGN}/F_\nu^{Gal} \simeq 7.7$ ($\Delta m_{AB} \sim$ mag).

Since these "Super-Stacks" were created solely for the purposes of visualization and probing the S/N of the total observed LyC signal from our samples, we do not perform any further analysis of the LyC flux measured in these stacks. Because the absorption of ionizing photons by the IGM is nonlinearly dependent on redshift, modeling of the combined intrinsic LyC flux from galaxies spanning $2.3 \lesssim z \lesssim 4.1$ through various sight lines would become increasingly divergent, such that the resulting total f_{esc} value of these galaxies would be highly uncertain.

This exceedingly faint LyC emission emerging from the stack of the 12 galaxies with AGN appears to have a flat spatial distribution that is *not* centrally concentrated. This may allude to the manner in which LyC escapes from galaxies. In order to ionize the IGM, LyC photons must escape through holes in the

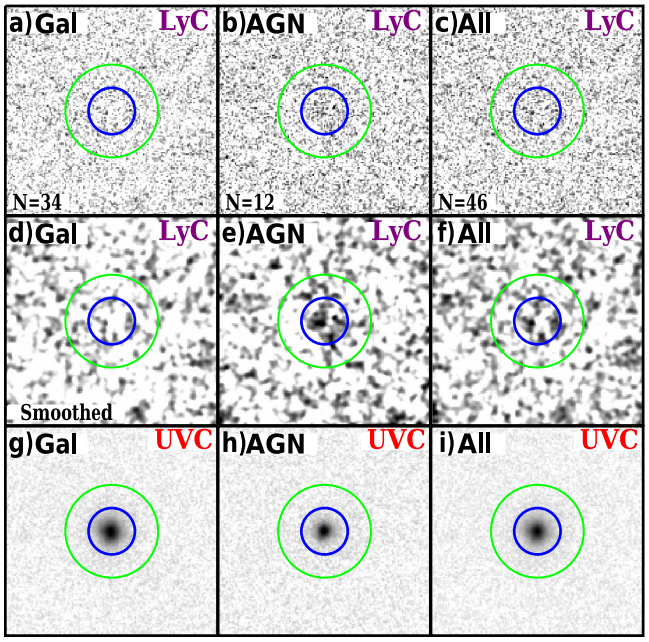

Figure 10. (Top row) LyC stacks of all galaxies in our sample with high quality spectra and reliable redshifts. (Middle row) The same as the top row but convolved with a 1σ Gaussian kernel. (Bottom row) The UVC counterparts of the top row. (a), (d), and (g), Composite stacks of all galaxies without AGN in our spectroscopic sample observed in the F225W, F275W, and F336W filters. (b), (e), and (h), Composite stacks of all galaxies hosting (weak) AGN. (c), (f), and (i), Composite stacks of all 46 galaxies in our sample. These stacks represent the average *observed* LyC F_ν from all galaxies integrated from $2.3 \lesssim z \lesssim 4.1$, scaled to a common zero-point magnitude. The blue and green circles have radii $0\farcs5$ and $1\farcs0$, respectively. The measured S/N of the combined LyC emission in these stacks is $\sim$2.3, 0.7, and 3.9σ for the stack of all galaxies, all galaxies without AGN, and all galaxies with AGN, respectively. The AGN stacks exhibit both a centrally concentrated and extended component in their flux distributions, from contributions of a central AGN point source and perhaps also from scattered photons (Figure 7). These images suggest that LyC escape paths may be slightly offset from a galaxy center, including point source emission from the AGN. Given the random orientation of galaxies in each stack, this would explain the faint, non-centrally concentrated, and extended morphology of the detected LyC emission.

surrounding gaseous and/or dusty material between stars, the central point source, and the line of sight IGM, which can be distributed randomly within or around galaxies. With at most a few clear sight lines per galaxy, these stacked images suggest that some escape paths of LyC may be on average somewhat offset from the galaxy center, i.e., escaping more from the outskirts than the centers of these galaxies. Given the random orientation of galaxies in each stack, this would explain the faint, non-centrally concentrated, and extended morphology of the detected LyC emission. This may indicate that LyC photons produced by accretion disks in AGN escape from galaxies with weak AGN via scattering. We discuss the radial profiles of galaxies further in Section 5.4.

In our adopted Planck cosmology, the angular size scale decreases by $\sim$16% and the apparent fluxes dim by $\sim$75% from $z \simeq 2.3$ to $z \simeq 4.1$. We deliberately did *not* scale any of the pixel values or resample the pixel scale to account for these these changes during the stacking process over all redshifts, as we only created these super-stacks to quantify the S/N of the average *observed* LyC flux for our entire sample. Using a varying pixel scale for each galaxy would have introduced correlated inter-pixel resampling noise, which would also decrease the sky SB limits and the effect of averaging over residual subtle systematics. Stacking with the same plate scale for all redshifts also preserves the observed photon statistics, which are needed for accurate sky-subtraction. Hence, resampling all the images as a function of redshift would reduce the S/N of the resulting stacked LyC signal. We note that the physical scale of the galaxies that we stack changes by $\pm$4% within each redshift bin and by $\pm$16% for the entire sample. This does not noticeably affect the LyC and UVC light profiles in each of our three redshift bins, which are discussed in Section 5.4, but does "blur" the light distribution seen in the super-stacks in Figure 10 by approximately these amounts in the radial direction from the center. Figure 10 can thus only be used to visualize the combined *observed* LyC signal over the entire redshift range $z \simeq 2.3$–4.1, but cannot be used for further quantitative analysis.

5. LyC Escape Fractions, and Radial Surface Brightness Profiles

5.1. Relative and Absolute LyC Escape Fractions for Stacks

Estimating the escape fraction of LyC photons from galaxies, $f_{\rm esc}$, is non-trivial, as it requires modeling of their apparent *intrinsic* LyC flux, $F^{\rm int}_{\nu,{\rm LyC}}$, and the wavelength-dependent transmission of LyC photons through the IGM, $\mathcal{T}^{\rm LyC}_{\rm IGM}(z, \nu)$, for a galaxy at redshift z. Quantitatively, the average *observed* LyC flux ($F^{\rm obs}_{\nu,{\rm LyC}}$) from a stack of galaxies, measured by a photon counting device such as a CCD, is given by:

$$\langle F^{\rm obs}_{\nu,{\rm LyC}} \rangle = \frac{1}{N_{\rm gal}} \sum_{i=1}^{N_{\rm gal}} \frac{\int T^{\rm LyC}_{\rm obs}(\nu) \mathcal{T}_{\rm IGM}(z_{\rm i}, \nu) f^{\rm abs}_{\rm esc,i} F^{\rm int}_{\nu,{\rm i}}(\nu) \frac{d\nu}{\nu}}{\int T^{\rm LyC}_{\rm obs}(\nu) \frac{d\nu}{\nu}}, \quad (1)$$

where $N_{\rm gal}$ denotes the number of galaxies in the stack, $F^{\rm int}_{\nu,{\rm i}}$ denotes the *intrinsic* (i.e., produced) stellar SED from galaxy "i," $f^{\rm abs}_{\rm esc,i}$ denotes the fraction of the observed LyC flux that escaped from the galaxy into the IGM, $\mathcal{T}_{\rm IGM}(z_{\rm i}, \nu)$ denotes the wavelength-dependent IGM transmission curve for galaxy "i" at redshift z, which we acquired from the recent absorption models of Inoue et al. (2014), and the $T^{\rm LyC}_{\rm obs}(\nu)$ term denotes the combined transmission of the throughput from the Optical Telescope Assembly (OTA), the filter throughput, and the Quantum Efficiency (QE) of the detector used for the LyC observation (see Figure 1 for the WFC3/UVIS total system throughput curves).

We expect $f_{\rm esc}$ generally to vary between individual objects. However, since we stack the observed LyC emission from all galaxies in our sample, we simplify our analysis by assuming a constant $f^{\rm abs}_{\rm esc}$ value for all galaxies within a given redshift bin. We denote this "sample averaged" escape fraction with $\langle f^{\rm abs}_{\rm esc} \rangle$. We can then take $\langle f^{\rm abs}_{\rm esc} \rangle$ outside of the sum in Equation (1), and write:

$$\langle f^{\rm abs}_{\rm esc} \rangle = \frac{\langle F^{\rm obs}_{\nu,{\rm LyC}} \rangle}{\frac{1}{N_{\rm gal}} \sum_{i=1}^{N_{\rm gal}} \frac{\int T^{\rm LyC}_{\rm obs}(\nu) \mathcal{T}_{\rm IGM}(z_{\rm i}, \nu) F^{\rm int}_{\nu,{\rm i}}(\nu) \frac{d\nu}{\nu}}{\int T^{\rm LyC}_{\rm obs}(\nu) \frac{d\nu}{\nu}}}, \quad (2a)$$

which can also be expressed as:

$$\langle f_{\rm esc}^{\rm abs}\rangle = \frac{\langle F_{\nu,\rm LyC}^{\rm obs}\rangle}{\frac{1}{N_{\rm gal}}\sum_{i=1}^{\rm N_{gal}} F_{\nu,\rm LyC,i}^{\rm int}} = \frac{\langle F_{\nu,\rm LyC}^{\rm obs}\rangle}{\langle F_{\nu,\rm LyC}^{\rm int}\rangle}. \quad (2b)$$

A more thorough analysis should also take into account that the impact of the IGM varies substantially around this mean for individual objects and sight lines (see Inoue & Iwata 2008; Nestor et al. 2011). We determine $F_{\nu,\rm i}^{\rm int}(\nu)$ for each galaxy from the minimized χ^2 fit (Bruzual & Charlot 2003, BC03) synthetic stellar population model SED, which was fit to four to six non-ionizing continuum broadband WFC3/IR+ACS/WFC measurements longward of Lyα at the known *fixed* redshift. These best fit SEDs were allowed four degrees of freedom for the χ^2 minimization at the fixed spectroscopic redshift of each object, i.e., the age, stellar mass, A_V, and the exponentially decreasing SFR timescale (τ). These were fit from a grid of SEDs using a wide range in each of these parameters. Thus, the best fit SEDs correspond to the observed F_ν of the galaxy *with* Calzetti et al. (2000) attenuation applied to the *intrinsic SED*, thereby determining the best fit A_V value. We use a Salpeter (1955) IMF and adopt solar metallicities for the SEDs.

In order to determine the absolute fraction of escaping LyC ($f_{\rm esc}^{\rm abs}$), which compares the apparent flux of LyC photons produced by stars in the galaxy to the observed LyC emission (i.e., $F_{\nu,\rm LyC}^{\rm obs}/F_{\nu,\rm LyC}^{\rm int}$), the effects from dust must be removed from the SED to obtain its *intrinsic* LyC flux, $F_{\nu,\rm LyC,i}^{\rm int}(\nu)$. Since we began our SED fitting with the intrinsic stellar population photospheric flux—which was then reddened by a specified A_V value using Calzetti et al. (2000) attenuation—we simply use the initial dust-free intrinsic stellar photospheric SED to calculate $F_{\nu,\rm i}^{\rm int}(\nu)$ for each galaxy. Thus, the *absolute* escape fraction quantifies the amount of LyC that is not absorbed by dust, the multiphase ISM, or other sources of LyC absorption in the galaxy.

The sample average escape fraction of LyC flux *relative* to the non-ionizing UVC flux ($F_{\nu,\rm UVC}$), denoted as $f_{\rm esc}^{\rm rel}$, is defined the as:

$$\langle f_{\rm esc}^{\rm rel}\rangle = \frac{1}{N_{\rm gal}}\sum_{i=1}^{N_{\rm gal}} \frac{F_{\nu,\rm UVC,i}^{\rm int}/F_{\nu,\rm LyC,i}^{\rm int}}{F_{\nu,\rm UVC,i}^{\rm obs}/F_{\nu,\rm LyC,i}^{\rm obs}} \simeq \frac{1}{N_{\rm gal}}\frac{\langle F_{\nu,\rm LyC}^{\rm obs}\rangle}{\langle F_{\nu,\rm UVC}^{\rm obs}\rangle}\sum_{i=1}^{\rm N_{gal}} \frac{F_{\nu,\rm UVC,i}^{\rm int}}{F_{\nu,\rm LyC,i}^{\rm int}} \quad (3a)$$

Using Equation 2(b), we can further simplify this expression as:

$$\langle f_{\rm esc}^{\rm rel}\rangle \simeq \langle f_{\rm esc}^{\rm abs}\rangle \frac{\sum_{i=1}^{N_{\rm gal}} F_{\nu,\rm UVC,i}^{\rm int}}{\sum_{i=1}^{\rm N_{gal}} F_{\nu,\rm UVC,i}^{\rm obs}} = \langle f_{\rm esc}^{\rm abs}\rangle \left\langle \frac{F_{\nu,\rm UVC}^{\rm int}}{F_{\nu,\rm UVC}^{\rm obs}}\right\rangle, \quad (3b)$$

where $F_{\nu,\rm UVC,i}^{\rm obs}$ is the observed UVC flux from galaxy "i" as measured in the ACS/WFC UVC filters (see Section 4.1) and:

$$F_{\nu,\rm UVC,i}^{\rm int} = \frac{\int T_{\rm obs}^{\rm UVC}(\nu) F_{\nu,\rm i}^{\rm int}(\nu)\frac{d\nu}{\nu}}{\int T_{\rm obs}^{\rm UVC}(\nu)\frac{d\nu}{\nu}} \quad (4)$$

for UVC observations with a total system throughput of $T_{\rm obs}^{\rm UVC}(\nu)$. Thus, the relative and absolute escape fractions differ by a factor of $\left\langle \frac{F_{\nu,\rm UVC}^{\rm int}}{F_{\nu,\rm UVC}^{\rm obs}}\right\rangle = \langle f_{\rm esc}^{\rm UVC}\rangle^{-1}$ for the total sample, which deviates from unity depending on the A_V and χ^2 values of the SED fits. The escape fraction of non-ionizing UVC photons, $f_{\rm esc,i}^{\rm UVC}$, is related to the observed reddening in galaxy "i" as $f_{\rm esc}^{\rm UVC}=10^{-0.4\,A_{\rm UVC}}$. Note that this term can be omitted from Equation 3(a) when using the *intrinsic* (unreddened) model SEDs instead of the observed ones. We determine the ratio of intrinsic fluxes of the LyC and UVC emission from all galaxies as:

$$\left\langle \frac{F_{\rm UVC}}{F_{\rm LyC}}\right\rangle_{\rm int} = \frac{\sum_{i=1}^{N_{\rm gal}} F_{\nu,\rm UVC,i}^{\rm int}}{\sum_{i=1}^{N_{\rm gal}} F_{\nu,\rm LyC,i}^{\rm int}} \quad (5)$$

without applying the $\mathcal{T}_{\rm IGM}(z_{\rm i}, \nu)$ term to $F_{\nu,\rm LyC,i}^{\rm int}$. The *observed* LyC and UVC flux ratios can be obtained by performing photometry on stacked images of the LyC and UVC emission shown in Figures 6–8.

Compared to the *intrinsic* LyC flux, the *intrinsic* stellar UVC flux of these galaxies increases by a factor $2.98^{+0.08}_{-0.07}$ (e.g., Siana et al. 2010). We determine this factor as expressed in Equation (5) from the intrinsic SEDs and filter curves used for LyC and UVC observations, with their 1σ dispersion, as listed in Column 4 of Table 3. Moreover, at $\langle z\rangle \simeq 2.68$, the *filter-weighted* average IGM transmission of the redshifts in the stack is $0.247^{+0.086}_{-0.085}$, which was determined from the models of Inoue et al. (2014), and is listed in Column 7 of Table 3.

We also include an estimate of the SED error from the 4–6 observed continuum data points that were used to fit each SED at its fixed known redshift, i.e., the filters that sample the continuum emission of the galaxies longward of Lyα up to WFC3/IR F125W, which are not affected by the IGM, even at high redshift. The main uncertainty in the SED fitting is therefore *not* the χ^2 values of fitted data, but the uncertainty in the applied internal extinction values A_V to each SED, which is unknown. We therefore do not include a dust-correction *error* in our calculations. Calzetti et al. (2000) empirically derived the dust attenuation curves of nearby starburst galaxies and found a total to selective extinction value of $R_V = 4.05 \pm 0.8$. Our SEDs were reddened with various dust screen A_V values by $F_\nu^{\rm obs}(\lambda) = F_\nu^{\rm int}(\lambda)10^{-0.4A_\lambda}$, where $A_\lambda = k(\lambda)A_V/R_V$. The attenuation for wavelengths shorter than 630 Å and longer than 2200 Å were extrapolated from the interpolated slope of the endpoints of the attenuation curves. The applied reddening does not include the uncertainty in the R_V value. Estimating the reddening error in the flux of our sample galaxies would require a more extensive SED fitting analysis, which takes into account the equally probable A_V values that fall within the measurement errors of the observed continuum data points. We instead assume a single A_V value and vary the SED flux based on their observed continuum errors. This error estimate is equivalent to applying a convolution to the intrinsic SED LyC flux with a Gaussian kernel (see Section 5.2) and so applying an additional dust-correction error would only increase the size of this kernel. Since the uncertainties in our measurements are dominated by the variation of the IGM transmission of LyC at the various redshifts and sight lines, we did not attempt to quantify this additional dust-correction error. Nevertheless, our calculated $f_{\rm esc}$ values themselves (Section 5.2) are not significantly affected by the A_V uncertainty, though their quoted $\pm1\sigma$ ranges would increase somewhat. Further details on the adopted A_V distributions are given in Appendix D.1.

Table 3
Summary of f_{esc} Constraints

$\langle z \rangle$	N_{obj}	$\langle f_{UVC}/f_{LyC} \rangle_{obs}$	$\langle f_{UVC}/f_{LyC} \rangle_{int}$	$\langle t_{age} \rangle$ (year)	AV_{med} (mag)	$\langle \mathcal{T}_{IGM} \rangle$	$\langle f_{esc}^{abs} \rangle$ (%)
(1)	(2)	(3)	(4)	(5)	(6)	(7)	(8)
Galaxies without AGN							
2.350	17	27^{+61}_{-5}	20.2 ± 0.1	$10^{8.2^{+0.9}_{-0.3}}$	$0.40^{+0.20}_{-0.40}$	$0.326^{+0.062}_{-0.085}$	22^{+44}_{-22}
2.752	7	<98.0	12.8 ± 0.1	$10^{7.9^{+0.6}_{-0.1}}$	$0.40^{+0.21}_{-0.02}$	$0.218^{+0.102}_{-0.085}$	<53
3.603	10	<50.1	15.6 ± 0.2	$10^{8.5^{+0.6}_{-0.8}}$	$0.0^{+0.4}_{-0.0}$	$0.066^{+0.045}_{-0.033}$	<55

Note. Table columns: (1) average redshift of each stack; (2) number of objects in each redshift bin, as in Table 2; (3) average *observed* flux ratio $f_{\nu,UVC}/f_{\nu,LyC}$ and its $\pm 1\sigma$ error range, as measured from the LyC and UVC stacks in their respective apertures (see Section 4.2 and Table 2); (4) average *intrinsic* flux ratio $f_{\nu,UVC}/f_{\nu,LyC}$ and its $\pm 1\sigma$ error range, as derived from the BC03 best fit SED models galaxies without AGN in each of our redshift bins (see Section 5.1 and Equation (5)); (5) average age of the stellar populations from the best fit BC03 models and their $\pm 1\sigma$ standard deviations in years; (6) median dust extinction A_V and its $\pm 1\sigma$ error range of the best fit BC03 SED model (the median A_V is more representative, as the distributions of each subsample is asymmetric; see Appendix D.1); (7) average filter-weighted IGM transmission of all sight lines and redshifts in the stacks and their $\pm 1\sigma$ standard deviations, calculated from the Inoue et al. (2014) models; (8) ML and $\pm 1\sigma$ or upper limit values of the Monte Carlo analysis of f_{esc}^{abs} in percent, i.e., the escape fraction of LyC including effects from all components of the ISM and reddening by dust as described in Section 5.1 (Equation 2(b)).

5.2. Estimating the LyC Escape Fraction: Monte Carlo Analysis

Since we cannot measure the amount of intrinsic LyC radiation produced by stars within galaxies directly, we must use the best available stellar population synthesis and IGM absorption models to estimate the fraction of LyC that escapes from galaxies at high redshift in a statistical way. We first find the best fit BC03 model of each galaxy at their spectroscopically verified redshifts using four to six band photometric data points taken from the Skelton et al. (2014) photometric catalog. With the BC03 SED and the IGM transmission models of Inoue et al. (2014), we simulated the most likely f_{esc} values for the galaxies in our three redshift bins with a Monte Carlo analysis, treating the various measured and modeled fluxes and IGM transmission as discrete random variables (RVs), which incorporates a range of possible values for these measurements. This method also allows us to model the most likely apparent intrinsic flux from individual galaxies in a stack, which can vary substantially around the mean for galaxies at different redshifts observed through different IGM sight lines (Inoue & Iwata 2008). We model all observed stacked fluxes from galaxies using Gaussian RVs for each pixel value in each sub-image, where the mean of the Gaussian is the count rate in the exposure, and the variance is equal to the sum of the variance of the sky-background and the square of the corresponding pixel value from the rms map. These 151×151 Gaussian RVs in each sub-image are combined by weighted sums in the same way described in Section 4.1, and flux is measured within the UVC aperture for each realization of the stack.

For each galaxy, we take our best fit BC03 SED to obtain our dust-free (intrinsic) model LyC flux measurement ($F_{\nu,LyC,i}^{int}$), as denoted in Equation 2(a), before correcting for IGM absorption. We then approximate the error of this *model* LyC flux by independently varying the *observed* continuum data points the SEDs were fit to within their error bars, and refitting the SED by least squares, i.e., $F'_\nu(\nu) = \alpha F_\nu(\nu)$, where $\alpha = \boldsymbol{F}_\nu^{\boldsymbol{r}} \cdot \boldsymbol{F}_\nu^{\boldsymbol{m}} / ||\boldsymbol{F}_\nu^{\boldsymbol{m}}||^2$ and $\boldsymbol{F}_{\nu,\boldsymbol{i}}^{\boldsymbol{r}}$ and $\boldsymbol{F}_{\nu,\boldsymbol{i}}^{\boldsymbol{m}}$ are the randomized *observed* flux measurements and continuum band *model* fluxes, respectively. This process is equivalent to convolving the *model* LyC flux with a Gaussian kernel of width equal to the quadratic sum of the *observed* relative continuum errors. These continuum band *model* fluxes were calculated by convolving the apparent dust-attenuated SED with the respective filter transmission curve, similar to Equation (4).

Using the models of IGM transmission with updated absorber statistics from Inoue et al. (2014), which simulates the transmission of photons through the IGM from $600\ \text{Å} < \lambda_{rest} < 1300\ \text{Å}$ for 10^4 lines of sight, we apply the IGM attenuation to our *model* LyC flux by convolving the SED with the wavelength-dependent IGM transmission coefficient curve at the redshift of the galaxy for all 10^4 simulated lines of sight. We then convolve the IGM attenuated model flux with the model error that we calculated to obtain our final model LyC flux (i.e., $F_{\nu,LyC,i}^{int}$). We then stacked all of the IGM attenuated *model* LyC fluxes of all galaxies in their respective redshift bins to obtain our stacked *model* LyC flux as denoted in Equation 2(a). The stacked *model* LyC flux was then used to calculate f_{esc}^{abs}, and the dust-attenuated f_{esc}^{abs}, as shown in Equation 2(b). Since we performed a non-correlated sum of the model LyC flux RVs to estimate this intrinsic stacked LyC flux, we run this f_{esc} calculation for a total of 10^3 trials, which we combine in order to generate a statistically significant sample of possible f_{esc} values. The probability mass function (PMF) of f_{esc} was then calculated by optimally binning these f_{esc} samples according to the Freedman–Diaconis rule (see Section 2.3), and normalizing by $N_{samples}$ to give their relative probabilities. The full f_{esc} PMFs are shown in Figure 11 for galaxies without AGN. The statistics of the sample array, i.e., the ML values, averages, and $\pm 1\sigma$ error ranges were computed and are shown in Figure 11 and Columns (8) and (9) of Table 3.

Since each element in our sample represents a simulated possible value of f_{esc}, we take the mode, or the maximum likelihood (ML) value of our PMF as the f_{esc} value representative of our galaxies at their average redshift, as these values correspond to the escape fraction of the total flux from all galaxies in each stack. The $\pm 1\sigma$ error bars were computed from the inner 68% of the PMF at equal probability, and upper limits were computed at (84%) of the full data set. The averages and medians were computed from the full data set as well. These *model* LyC fluxes also represent the lines of sight, where escaping LyC flux was transmitted through the IGM before being absorbed by Lyman Limit Systems and Damped Lyα systems within $\Delta z \simeq 0.5$. The opaque lines of sight, where the IGM transmission peaks near $\mathcal{T}_{IGM}^{LyC} \simeq 0.01$, represent ~30%–40% of our potential model LyC flux values. These

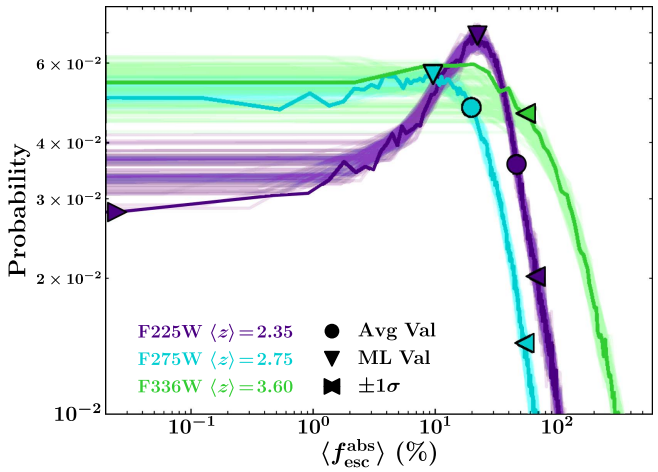

Figure 11. Probability mass functions (PMFs) of the *absolute* $f_{\rm esc}$ values from the MC simulations described in Section 5 plotted against their relative probability. This analysis was performed 10^3 times using the measured and modeled intrinsic stacked *apparent* LyC flux and their $\pm1\sigma$ ranges. We apply the IGM attenuation models of Inoue et al. (2014) to our modeled LyC fluxes. These $f_{\rm esc}^{\rm abs}$ values were optimally binned according to the Freedman–Diaconis rule (see Section 4.1). Downward triangles and circles indicate the resulting ML and average $f_{\rm esc}$ values in each probability distribution function, respectively, while the left/right-facing triangles indicate the $\pm1\sigma$ range around the mode.

lines of sight result in higher $f_{\rm esc}$, as the model LyC would have been attenuated by more absorbers. However, ∼40%–50% of our lines of sight have average IGM transmission values $\mathcal{T}_{\rm IGM}^{\rm LyC} \gtrsim 0.4$ (where the transmission distribution is at a local minimum), and corresponds to the peak of the $f_{\rm esc}$ PMFs, where the model LyC flux encountered fewer absorbers. These lines of sight have a local maximum transmission near $\mathcal{T}_{\rm IGM}^{\rm LyC} \simeq 0.7$, and about ∼0.3% of these sight lines can be as high as $\mathcal{T}_{\rm IGM}^{\rm LyC} \simeq 0.85$.

5.3. Implications of the $f_{\rm esc}$ MC Results

We list the results of our $f_{\rm esc}$ MC simulations in Table 3. The average absolute escape fraction, $\langle f_{\rm esc}^{\rm abs}\rangle$, from galaxies at various redshifts can be used to determine what fraction of LyC produced by the stellar photospheres in those galaxies escapes, i.e., is not absorbed by interstellar neutral H I, dust, etc., at their average redshift. However, variations in IGM transmission can cause these values to become highly uncertain when stacking LyC emission from galaxies over too broad of a redshift range. Thus, in order to ascertain any meaningful evolution in $f_{\rm esc}^{\rm abs}$, we must stack galaxies at similar redshifts and compare their $f_{\rm esc}^{\rm abs}$ values from sample to sample. Then, any trends in the independent subsamples can be used to constrain correlations of $f_{\rm esc}$ with galaxy properties or evolution with redshift. Modeling these properties can also be used to determine their impact on $f_{\rm esc}$, and to see if trends in these properties with redshift can affect the apparent evolution of $f_{\rm esc}$ with cosmic time.

The galaxies selected in our $\langle z\rangle \simeq 2.35$ and $\langle z\rangle \simeq 2.75$ stacks have, on average, younger stellar populations and more dust than the $\langle z\rangle \simeq 3.60$ stack. The $f_{\rm esc}$ value for galaxies *selected* at $\langle z\rangle \simeq 3.60$ are indicative of somewhat older stellar populations (of ∼1 Gyr), but are not significantly affected by the lower amount of dust observed in these galaxies. The $\langle z\rangle \simeq 2.35$ and $\langle z\rangle \simeq 2.75$ stacks sample galaxies that are undergoing a period of more active star formation compared to the two higher redshift samples, which may have led to the accumulation of more H I gas and dust in these galaxies, but also a brighter *intrinsic* LyC flux. Thus, these $f_{\rm esc}^{\rm abs}$ values also imply that the ISM can absorb a larger fraction of LyC flux from older stellar populations than from younger ones when comparing $f_{\rm esc}^{\rm abs}$ from older and younger stellar populations.

Although young stellar populations can produce more intrinsic LyC than older ones, which then has a higher probability of escaping the ISM, higher extinction from dust in the UVC may correlate to a reduced efficiency of LyC escape. Although dust is the dominant factor for attenuation for $\lambda > 912$ Å, ionizing radiation is more strongly absorbed by neutral hydrogen due to the higher cross sectional area (Richings et al. 2014). LyC escape requires very low neutral Hydrogen column densities ($N_{\rm H} < 10^{17}$). Since the amount of extinction from dust is strongly correlated to the column density of hydrogen (Bohlin et al. 1978; Fitzpatrick 1999; Rachford et al. 2002), higher extinction may then be indicative of low $f_{\rm esc}$. This apparent correlation of high dust extinction and low $f_{\rm esc}$ is consistent with the results of several observational and analytical studies that investigate the impact of various galactic parameters on $f_{\rm esc}$ (e.g., Mathis 1971; Leitherer et al. 1995; Inoue 2001; Bergvall et al. 2013).

5.4. The Observed Radial Surface Brightness Profiles in UVC and LyC

The radial profiles of our LyC and UVC stacks from Figure 8 for F275W and F336W are shown in Figure 12. We construct all observed radial SB profiles by summing successive annuli of three pixel radii beginning with the central pixel, where each pixel is treated as a Gaussian RV with the mean set to the pixel value in the stack and variance set to the sum of the variance from the square of the pixel value in the corresponding rms map, and the variance from the sky-background. This allowed us to estimate uncertainties on a per pixel basis for generating flux distributions of the sum of several pixels. The averages and $\pm1\sigma$ errors or 1σ upper bounds to these distributions are indicated as vertical bars and downward triangles, respectively.

The stacked UVC profiles are shown as solid curves, and those for LyC are dashed. The *observed* PSFs in the WFC3/UVIS F275W and ACS/WFC F606W mosaics are indicated by dotted curves, normalized to the central surface brightness of the corresponding LyC SB profile. The PSF in F336W is very similar to the F275W PSF, so we do not plot it. These are available in Table 1 and Figure 7(b) of W11. Note that these PSFs measured in the 0.″03 mosaics are undersampled. The 1σ SB sensitivity limit for the LyC profile in the F275W stack is indicated by a horizontal dashed line at $\mu_{\rm AB} \simeq 30.5$ mag arcsec^{-2}. For the sensitivity limits of the samples in the other filters, we refer the reader to Columns 9 and 10 of the Table 4 in Appendix A and to the discussion of systematics in the stacked data in Appendices A–C. These SB sensitivity limits are consistent with the 1σ sky-subtraction errors discussed in Section 2.2.

Both UVC SB profiles are clearly extended with respect to their corresponding filter PSFs, as expected for stacked galaxy radial light profiles at $z \simeq 3$–6 (e.g., Hathi et al. 2008). The much deeper HUDF UVC stacks of Hathi et al. (2008) suggested a possible "break" (or slight change in slope) near $r \gtrsim 0.''3$–$0.''4$, from exponential in the inner parts to a somewhat less steep profile in the outskirts. Our stacked UVC light profiles do not clearly show a change in slope at

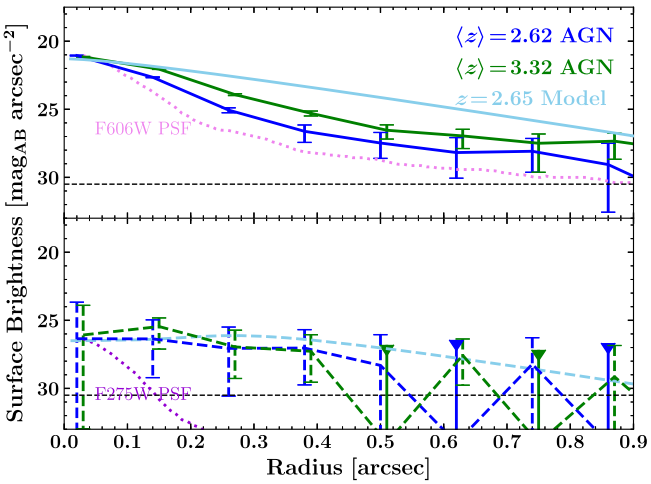

Figure 12. Radial surface brightness profiles of the non-ionizing UVC signal (solid curves) and the LyC signal (dashed curves) measured in the stacks (Figure 8) for the galaxies with AGN samples. The curves are color coded according to their mean redshift (filter): $\langle z\rangle = 2.68$ (F606W and F275W; blue) and $\langle z\rangle = 3.49$ (F775W and F336W; green). The *observed* PSF in F275W and F606W are indicated by dotted purple and pink curves, which were normalized to the central SB of the corresponding LyC surface brightness profiles. The horizontal black dashed line indicates the 1σ sensitivity limit for the LyC profile in F275W. Both UVC surface brightness profiles are extended with respect to the corresponding PSF curves. The observed LyC stack SB profiles are also extended *and* flatter than the UVC profiles, which is also predicted from our LyC scattering model (light blue dashed curve), where scattering of the escaping LyC photons off electrons and/or dust with a porous ISM spreads the LyC emission beyond the distribution of the stellar UVC light (light blue solid curve). The light blue solid curve is scaled from light blue dashed curve by a single ratio of $\frac{f_{\rm UVC}}{f_{\rm LyC}}$, which may depend on radius. See Section 5.5 for further details of the model.

$r \gtrsim 0\farcs3$–$0\farcs4$, since our (77–180 orbit) UVC stacks are not nearly as deep as their ∼1680–4300 orbit stacks, and because of our much more stringent method of masking neighbors.

Both LyC SB profiles are also clearly extended with respect to their *observed* PSFs, and remain extended to $r \simeq 0\farcs5$, beyond which errors in the sky-subtraction start to become substantial. The very faint, flat, non-centrally concentrated appearance of the combined LyC signal makes the extraction of its SB profile uncertain at larger radii. The relatively flat LyC SB profiles may indicate a more complicated LyC escape scenario, in which the light distribution of the LyC flux of a stack of galaxies is largely dependent on the porosity of the ISM in those galaxies, and/or the scattering processes that the LyC photons undergo before escape. We find that the UVC SB profiles are well fit to Sérsic profiles of index of $n \simeq 2.4 \pm 0.7$, while the LyC SB profiles could not converge to a Sérsic fit but are better fit to straight lines with slope $\sim 2.5 \pm 0.6$ mag arcsec^{-2} per arcsec. The difference in linear slope between UVC and LyC is ∼6 mag arcsec^{-2} per arcsec with a formal S/N of ∼2.8, so the LyC is therefore likely flatter. This may also be indicative of a decreasing LyC opacity with radius, as the LyC and UVC escape morphology differs radially.

After integrating these SB profiles as elliptical frustums between each isophote, we find reasonable agreement with our photometric analysis (see Table 2), although the flux represented by the radial SB profiles is consistently fainter by $\sim 0.3 \pm 0.2$ mag. This discrepancy is expected, given that our SB profiles do not extend out to the larger aperture sizes used in the photometry of the stacks, and therefore miss some real LyC flux that might be present at larger radii and at very faint SB levels.

5.5. Modeling the UVC and LyC Radial Surface Brightness Profiles

For the highest S/N measurements in the LyC stacks (i.e., F275W/F336W), the radial SB profile of escaping LyC flux appears to be flatter than the corresponding *non-ionizing* UVC profile (the dashed and solid colored curves in Figure 12, respectively).

A LyC SB profile that is measurably flatter than the corresponding UVC SB profile could arise naturally in a porous ISM, in which the covering factor of neutral gas decreases with increasing galacto-centric distance. To illustrate this quantitatively, we consider the transfer of UVC and LyC photons through simplified models of galaxies with a multi-phase ISM.

To calculate this, we assume that the UVC sources are spatially extended and characterized by a volume emissivity $\epsilon_{\rm UVC}(r)$. We assume an exponential distribution with galactic radius: $\epsilon_{\rm UVC}(r) = \epsilon_{\rm UVC,0}\exp(-r/r_0)$. The normalization constant $\epsilon_{\rm UVC,0}$ and scale length of r_0 are obtained by matching the observed SB profiles in Figure 12. We further assume that LyC emission traces the UVC emission. We attribute differences in observed SB profiles to the fact that neutral clumps of gas are opaque to LyC radiation, but not to UVC.

We also assume a (spherical) distribution of neutral gas clumps, which is described completely by its covering factor, $f_{\rm cov}(r) \equiv n_{\rm c}(r)A_{\rm c}(r)$. Here, $n_{\rm c}$ and $A_{\rm c}(r)$ denote the number of clumps and area of a clump at r, respectively. The covering factor $f_{\rm cov}$ then denotes the probability that a sight line intersects a clump per unit length. For example, for clumps of fixed size that are outflowing at *an assumed constant* velocity v, we have a number density dependence as $f_{\rm cov} \propto n_{\rm c} \propto r^{-2}$ (we refer the reader to Dijkstra & Kramer (2012) for a more detailed description of this covering factor).

The precise radial dependence of $f_{\rm cov}$ is not known. However, when $f_{\rm cov}$ decreases with r, we generally expect increased LyC escape fractions at larger galacto-centric distances. We consider two parameter models for $f_{\rm cov} = Ar^{-x}$, and fit for A and x. Both A and v can also depend on radius. Hence, $f_{\rm cov}$ generally is some unknown power law of r (i.e., r^{-x}), where x typically ranges between 0 and 3. This calculation shows that when sight lines with low impact parameter see the largest $f_{\rm cov}$, we see a reduced escape fraction in these directions.

An interesting possibility is that the neutral gas clouds can theoretically *scatter* LyC photons: LyC photons penetrate the neutral clumps over an average distance that corresponds to $\tau \simeq 1$. Direct recombination to the ground state produces LyC photons that can escape from the neutral cloud, as the optical depth to the edge of cloud is $\tau \simeq 1$. This "scattering" (absorption and re-emission of LyC photons occurs on the recombination timescale inside the cloud) of LyC photons could further flatten the predicted surface brightness profile. The possible effects of LyC scattering can be expanded to include scattering off free electrons and dust grains (which also differs between LyC and UVC).

While the dotted–dashed curve in Figure 12 is only a single example (matching our F275W LyC observations at $\langle z\rangle \simeq 2.62$) of these model LyC SB profiles, model predictions with similar parameter values fit the SB profiles in the other

redshift bin. With these models, we can integrate out to larger impact parameters and get a constraint on the total escape fraction that accounts for the difference in SB profiles. This procedure gives a slightly larger value for f_{esc} than those given in Table 3 (This is, of course, almost identical to the constraints one would obtain simply by extrapolating the surface brightness profiles to larger impact parameters, and integrating over them.)

6. Discussion of Results

6.1. Summary of Available Data on f_{esc} versus Redshift

The constraints we place on f_{esc} are valid for the luminosity range $M_{AB}^{UVC} \simeq -21.1^{+0.9}_{-0.5}$ mag present in the sample which was selected to have reliable spectroscopic redshifts (see Figure 4), with the two lowest redshift subsamples being dominated by relatively younger stellar populations with active star formation and significant dust extinction, the $\langle z \rangle = 3.60$ subsample comprises mostly lower extinction galaxies with somewhat older stellar populations. For faint galaxies to have finished reionization by $z \simeq 6$–7, their f_{esc} values need to be $\gtrsim$20% (Ouchi et al. 2009; Wilkins et al. 2011; Kuhlen & Faucher-Giguère 2012) beyond $z \simeq 6$ *and* their luminosities need to reach as faint as $M_{UVC} \simeq -15$ to -13 mag (e.g., Robertson et al. 2013). Hence, if faint (dwarf) galaxies contributed significantly to reionization at $z \lesssim 6$–7, one should consider how much their f_{esc} fraction might have increased *both* toward higher redshifts due to the expected lower metallicities and lower dust extinction, *and* at fainter luminosities due to the larger impact that SN driven outflows have on lower mass dwarf galaxies (e.g., Ricotti & Shull 2000; Razoumov & Sommer-Larsen 2007; Wise & Cen 2009; Fernandez & Shull 2011). Given that our spectroscopic selection samples luminous galaxies in all three redshift bins, our LyC detections can only constrain the first possibility, which we discuss here.

In Figure 13, we plot our ML and 1σ upper bound f_{esc}^{abs} values generated from the MC simulation listed in Table 3 for galaxies without AGN activity (purple filled circles and triangles, respectively). We show the interquartile range of the $\langle z \rangle = 2.35$ f_{esc} data to emphasize it is highly asymmetric PMF, which has more data below the ML point. We also plot similarly derived, f_{esc}^{abs} data available in published work summarized in Section 1 as light blue points, with upper limits indicated as blue triangles. The light blue f_{esc} points indicate galaxies with rest-frame 1500 Å luminosities close to those sampled in Figures 5(a)–(c) (i.e., $\langle M_{AB} \rangle \simeq -21.1^{+0.9}_{-0.5}$ mag). The dependence of the f_{esc} values of galaxies on luminosity is not well determined, but no clear dependence on luminosity is obvious in Figure 13. We will therefore discuss the redshift dependence of f_{esc} here for the luminosities sampled in Figure 4.

We first converted the published f_{esc}^{rel} values to f_{esc}^{abs} when necessary using the quoted extinction values from the literature source. We note that these f_{esc} values were derived from different observational analyses, including both space- and ground-based spectra and imaging, with different object selection, reduction techniques, error assessment, and application of IGM attenuation models. We plot only the quoted f_{esc} values from the literature source most analogous to this study, i.e., those derived from their full, stacked sample. Some of the published errors may not account for the same uncertainties that we address in Section 5.2. When necessary, we converted the quoted published uncertainties to 1σ error bars, so they are comparable to our results in Table 3.

Although the f_{esc} values plotted in Figure 13 were derived with different methods, the current data appears to suggest a correlation of f_{esc} with redshift. However, any such relation may not be a simple power law in $(1+z)$. Several authors (Inoue et al. 2006; Razoumov & Sommer-Larsen 2010; Finlator et al. 2012; Kuhlen & Faucher-Giguère 2012; Becker & Bolton 2013; Dijkstra et al. 2014) have suggested that redshift averaged f_{esc} values for galaxies may increase significantly with redshift, possibly as steeply as $\propto(1+z)^3$–$(1+z)^5$. This only holds only for $z \lesssim 7$, beyond which the implied escape fraction would approach 100% for the upper bound, but decrease monotonically at lower redshift (e.g., Razoumov & Sommer-Larsen 2010). If the $(1+z)^{\kappa}$ exponent values were as steep as $\kappa \simeq 2.0$, this prediction would provide f_{esc} values at $z \gtrsim 6$ in excess of ~30%, as required for hydrogen reionization to have completed by $z \sim 6$ (Robertson et al. 2013). However, none of the simple $(1+z)^{\kappa}$ power laws for f_{esc} seem to be consistent with the data points in Figure 13 to within their stated 1σ errors.

6.2. A Redshift Dependence Faster than $(1+z)^{\kappa}$?

Since the plotted 21 independent data points in Figure 13 deviate from published power laws, *no* single $(1+z)^{\kappa}$ curve seems to fit all the f_{esc}^{abs} data for galaxies without AGN. We therefore suggest the possibility that *a more sudden decrease* of f_{esc}^{abs} with redshift may instead have to be considered. The combined data in Figure 13 suggests, however, that f_{esc}^{abs} may have declined by a factor of nearly ~10 from $\gtrsim$20% at $z \gtrsim 2$ to ~1% at $z \lesssim 2$. These low f_{esc} values at $z \lesssim 2$ are predicted by some cosmological radiative transfer models as well, which also require a "steep rise" in f_{esc} at $z \gtrsim 2$ for massive galaxies to reionize the universe (e.g., Khaire et al. 2016), and have also been suggested in studies of the Lyα escape fraction over redshift (e.g., Blanc et al. 2011).

Figure 13 indicates that the sudden decrease in f_{esc}^{abs} may have occurred within the epoch of $z \sim 2$, or within about ± 1 Gyr of the observed peak in the cosmic star formation history (SFH) (Madau et al. 1996; Faucher-Giguère et al. 2008; Cucciati et al. 2012; Burgarella et al. 2013). This period may indicate the epoch where the universe transitions from infall/merger-driven SFGs at $2 \lesssim z \lesssim 6$ to a more passively evolving universe by giant galaxies at $z \lesssim 1$–2 (Driver et al. 1998). This transition may have resulted in dust and gas rapidly accumulating in the disks and central bulges of forming galaxies, with an SN rate that has progressively less impact on clearing gas and dust from the galaxies that are steadily growing in mass with cosmic time. It is possible that this process may have caused f_{esc}^{abs} to rapidly drop over a relatively narrow interval of cosmic time in luminous galaxies, as massive LyC-producing stars formed during the period of high SFR become either SNe II or AGB stars, which then enrich the ISM with dust within ~1 Gyr (Mathis 1990; Bekki 2015). The infall of hydrogen in these galaxies could have then caused f_{esc}^{abs} to decrease substantially (Rauch et al. 2011; van de Voort et al. 2012). The subsequent increase of dust can then prevent the collapse of cold gas by photoelectric heating from stars or AGN in the galaxy (Krumholz & Dekel 2012; Forbes et al. 2016). This would then lead to a decrease in the galaxy's SFR, as feedback from heating inhibits the formation of new massive stars (e.g., Inoue 2001; Inoue et al. 2001). The decline in SFR would also

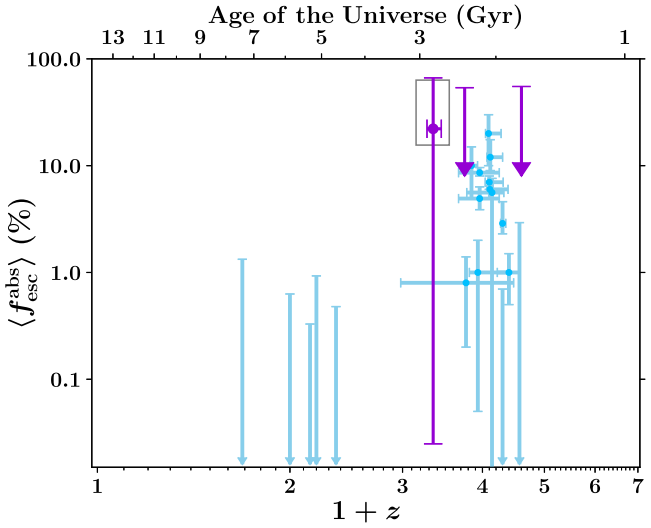

Figure 13. The *absolute* LyC escape fraction for various galaxy samples as a function of redshift. Plotted is our ML average f_{esc}^{abs} value with their $\pm 1\sigma$ range and 1σ upper limits for our galaxies *without* AGN sample (purple filled circled and triangles) taken from the probability mass functions of Figure 11, generated from our MC simulations described in Section 5. The interquartile range of the $\langle z \rangle = 2.35$ data is indicated by a box to highlight the high asymmetry of its PMF. The blue points indicate available published data as referenced in Section 1, some of which were converted from quoted f_{esc}^{rel} values using extinction values from the literature source (see Section 5.1, Equation 3 (b)). All vertical error bars are the $\pm 1\sigma$ uncertainty on the f_{esc} values. Some errors were converted from the quoted 2σ–3σ uncertainties. Upper limits are shown as blue downward triangles. Although the blue points represent galaxy samples with different properties from our samples, and the quoted errors were derived from uncertainties with different error assessment, the combined data suggests a correlation of f_{esc}^{abs} with redshift, which may not be a simple power law in $(1+z)$. This compiled data set does not rule out the possibility that massive galaxies may have had high enough LyC f_{esc} values to complete hydrogen reionization by $z \sim 6$, if galaxies at $2 \lesssim z \lesssim 4$ and $z \gtrsim 6$ are analogous.

lead to a decreasing SN rate (Botticella et al. 2012), further preventing the escape of LyC, as there would have been fewer clear channels produced by SN for the LyC to escape. LyC produced by AGN can be absorbed by gas and dust in the disk of the galaxy itself, depending on viewing angle. When galaxies produce stronger AGN outflows, more of their LyC radiation may escape approximately *perpendicular to* the galactic disk (e.g., Windhorst et al. 1998; Reunanen et al. 2003), which contributes to maintaining the ionized state of the IGM, as AGN begin to dominate the ionizing background at $z \lesssim 3$.

6.3. The Role of Galaxies with Weak AGN in Reionization

Figure 8 shows the stacked LyC and UVC images of the known galaxies with AGN in our sample. The $\langle z \rangle = 2.374$ stack only includes two AGN with a LyC flux of $m_{AB} > 27.91$ mag (UVC aperture). The $\langle z \rangle \simeq 2.61$ and 3.32 samples contain seven and three stacked AGN with measured LyC fluxes of $m_{AB} \simeq 28.3$ and 27.42 mag with $S/N \sim 2.7$ and 2.5, respectively. These fluxes are typically more luminous in LyC and have higher S/N than their non-AGN counterparts, despite having fewer stacked galaxies. This is most likely due to LyC originating from the central accretion disk, made visible by stronger AGN outflows when viewed under the right angle. AGN outflows can also increase the porosity of the ISM in its host galaxy (e.g., Silk 2005), thereby increasing f_{esc} of the LyC produced by stars, which further contributes to the total measured LyC flux from that galaxy.

The stacks in Figure 6 suggest some variety of LyC morphologies, though the UVC images exhibit more compact light profiles compared to the non-AGN stacks in all three cases (see the discussion in Sections 5.5–5.4). The $\langle z \rangle \simeq 2.62$ stack is the most extended of the AGN both in LyC and UVC, which is most likely due to the increased sensitivity to fainter flux at low redshift, with a central bright point source from radiation escaping along the observed line of sight. The radial dependence of the LyC SB profile for this stack may be due to the viewing angle of the AGN relative to the direction of the escaping LyC radiation, or possibly due to the fact that the LyC undergoes a more complex escape process, where photons can be reflected off of relativistic electrons in the AGN corona and accretion disk, or by hot dust in the torus via Thomson and/or inverse Compton scattering (e.g., Haardt & Maraschi 1993). The $\langle z \rangle \simeq 3.32$ AGN LyC stack appears to be more point-like, indicating that these observed LyC photons may be escaping predominantly along the line of sight, which is supported by the presence of broad emission lines in their spectra, although the more extended LyC emission may not be visible due to the average SB of these AGN at higher redshift being dimmed by an additional ~61% from $\langle z \rangle \simeq 2.62$ to $\langle z \rangle \simeq 3.32$.

Figure 4 shows that the *average* UVC luminosities of "galaxies with weak AGN" in our sample is about the same, or somewhat fainter than that of galaxies without AGN. Their average luminosity in Figure 4 $M_{AB} \simeq -20.4 \pm 0.9$ mag at $z \simeq 2.3$–4.1 does not indicate clearly QSO dominated luminosities or SEDs. Table 2 shows that the LyC flux measured from the stacks of (weak) AGN at all redshifts is typically *brighter* than galaxies without AGN. Thus, precise modeling of the intrinsic LyC emission must include the contribution of flux emitted by, or reprocessed from, the AGN accretion disk. The SED of the AGN accretion disk may be more complicated than a simple blackbody curve, as the SED must account for the broad and narrow emission line regions, as well as energy lost to relativistic jets and photons scattered/absorbed by the corona and central torus and non-AGN dust, which is also viewing angle dependent. Because we cannot fit both stellar +AGN SED models to the four to six band continuum data currently available for galaxies with weak AGN, we do not calculate escape fractions for these galaxies. Since the SEDs of these galaxies are likely dominated by stellar light at the non-ionizing wavelengths, their $f_{esc}(z)$ correlation may be similar to the trend seen from the escape fractions of galaxies without AGN. From the compact appearance in some of our stacked images—and from the fact that they are on average brighter than galaxies without AGN—the LyC flux in galaxies with weak AGN may be dominated by light originating from their accretion disks.

Further data and modeling is needed to better constrain $f_{esc}^{abs}(z)$ for both galaxies and weak AGN to confirm these observed trends. The current data for AGN may be consistent with a more modest drop in $f_{esc}^{abs}(z)$ than for galaxies that may have occurred close to the peak in the epoch of AGN activity around $z \simeq 2.5$ (e.g., Fontanot et al. 2007; Croom et al. 2009; Ikeda et al. 2011, Ikeda et al. 2012). Since AGN activity can affect the SFRs, it is possible that when AGN outflows started to ramp up after the peak in the cosmic star formation history at $z \simeq 2$ (Springel et al. 2005; Hopkins et al. 2006), their outflows

cleared enough paths in the host galaxy ISM to increase $f_{\rm esc}^{\rm abs}$ of a possibly AGN induced top-heavy stellar population IMF.

Because galaxies far outnumber AGN, and despite being fainter in LyC on average, their $f_{\rm esc}^{\rm abs}$ values suggest that galaxies may have produced sufficient LyC radiation to maintain reionization at $z \gtrsim 3$, while AGN likely dominated in the production of ionizing LyC flux at $z \lesssim 2$–3. Even though our spectroscopically selected sample of galaxies outnumber the *weak* AGN by a factor of ∼3 (see column 4 of Table 2), the total ionizing flux from AGN is brighter than that from galaxies *without* AGN by $\sim 7.7 \times 12/34 \sim 2.7$.

The current samples are still very small, and clearly need further confirmation through much larger samples, both through deep UV/optical imaging of wider *HST* fields and through spectroscopy on fields with high quality existing *HST* data. Further theoretical work is needed to outline exactly how quickly $f_{\rm esc}$ may have increased toward higher redshifts *and* at fainter luminosities, as well as at lower metallicities and lower extinction at higher redshifts, while producing enough escaping LyC photons from faint galaxies to finish and maintain reionization at $z \lesssim 6$–7.

There is already a significant issue in accounting for reionization with the faint galaxy population observed via cluster lensing at $z \simeq 9$. At redshifts larger than 8, the Hubble Frontier Fields reveal a strong drop in rest-frame UV luminosity density (e.g., Ishigaki et al. 2015). Hence, it is also possible that one may need to consider an additional source of reionizing photons beyond $z \simeq 6$–7. This source might include feedback on both the IGM ionization and clumpiness via hard ionizing photons from high mass X-ray binaries (e.g., Mirabel et al. 2011). Other astrophysical sources such as Population III stars or mini AGN seem strongly constrained via chemical evolution (Kulkarni et al. 2014) and the X-ray background (Dijkstra et al. 2004). It is possible that $f_{\rm esc}$ may evolve with redshift and/or with galaxy properties (e.g., mass, A_V, SFR, and/or age).

7. Conclusions

We studied LyC emission that may be escaping from galaxies using improved *HST* WFC3 of the ERS fields in three filters, where LyC may be observed from galaxies at $z \simeq 2.3$–4.1. The data that we used in our analysis was drizzled with the much more accurate 2013 WFC3 geometric distortion correction tables, which resulted in the correction of significant astrometric offsets that remained in earlier ERS UVIS mosaics. The WFC3 ERS UV images were taken in 2009 September, when the CTE was still at a level where faint flux could still be measured without significant losses. We verified that any loss in CTE is not the primary limitation to our measurements (see Appendix C.2).

We extracted sub-images centered on galaxies with high quality spectroscopically measured redshifts from the ERS mosaics, and averaged the LyC flux of those galaxies. We paid careful attention to the removal of potentially nearby contaminating objects and low-level variations in the UV sky-background during this stacking process. We ensured that no significant amount of contaminating flux longward of the Lyman break ($\lambda > 912$ Å) was included in our stacks. We performed a series of critical tests to ensure our stacking procedure was not affected by various systematics in the mosaic images. All of these tests are described in Appendices A–C. The following are our main findings:

(1) Our measurements of the average LyC flux in the stacks for galaxies at $z \simeq 2.3$–4.1 is summarized in Table 2. We find that the LyC flux of faint galaxies at $\langle z \rangle \simeq 2.35$, 2.69, and 3.54 is generally constrained at the <1–3σ level, in typical image stacks of 13–19 objects in the WFC3/UVIS F225W, F275W, and F336W filters, respectively. These upper limits correspond to total LyC fluxes of $m_{\rm AB} \gtrsim 28.1$–29.0 mag. The LyC flux of weak AGN is detected to be brighter on average at $z \simeq 2.3$–3.5, but over ∼2–10× fewer objects per stack.

(2) The combined LyC emission averaged over the three filters suggests an overall LyC flux distribution that is non-centrally concentrated, which may be explained by a radial dependence in the ISM porosity and/or scattering of the LyC photons. We find that the LyC flux from AGN is flatter than its UVC counterpart. This may suggest a complex escape process that may be determined by the distribution and extent of neutral (dusty) gas clouds within a porous multiphase ISM.

(3) From our best fit BC03 SED models fit to *HST* continuum observations longward of Lyα, the observed LyC flux corresponds to an *average* absolute LyC escape fraction constrained to $f_{\rm esc}^{\rm abs} \sim 22^{+44}_{-27}\%$ at $\langle z \rangle \simeq 2.4$ and $\lesssim$55% at $\langle z \rangle \simeq 2.8$–3.6. While the error bars on the implied $f_{\rm esc}$ values in each of the three redshift bins remain large, within the error bars, the data suggest an increasing trend of $f_{\rm esc}$ with redshift at $z \gtrsim 2$.

(4) The available published $f_{\rm esc}$ data for galaxies may suggest *a more sudden increase* in $f_{\rm esc}^{\rm abs}$ with redshift that occurred around $z \sim 2$. For galaxies, the steepest drop in $f_{\rm esc}$ occurs at $z \lesssim 2$, near the peak of the cosmic star formation history within an interval of ±1 Gyr from this peak in cosmic time.

(5) If galaxies *without* AGN at $z \sim 2$–4 are analogous to those at $z \gtrsim 6$, the upper limits to their $f_{\rm esc}^{\rm abs}$ values suggest that they may have had a sufficient LyC escape fraction to reionize the IGM by $z \gtrsim 6$. The SEDs of galaxies with weak AGN is likely dominated by *stellar light* in the non-ionizing continuum. Galaxies with weak AGN outshine galaxies *without* AGN in our sample by a factor of ∼7.7, or $m_{\rm AB} \sim 2.3$ mag. Hence, while galaxies without AGN likely began and maintained cosmic reionization at $z \gtrsim 3$, galaxies with (weak) AGN likely dominated the contribution to the cosmic ionizing background and maintain reionization at $z \lesssim 2$–3, although the role of massive galaxies without AGN may not have been negligible at $z \lesssim 2$.

The transition from galaxy-dominated reionization to weak AGN reionization appears to have occurred at $z \sim 2$–3, i.e., right around the peak in the cosmic SFR (Madau et al. 1996), which may indicate the epoch where the universe transitions from infall/merger-driven SFGs at $2 \lesssim z \lesssim 6$ to a more passively evolving universe by giant galaxies at $z \lesssim 1$–2. This may result in gas and dust rapidly accumulating in the disks and nuclei of forming galaxies, combined with an SN rate that has progressively less impact on clearing gas/dust in galaxies that are steadily growing in mass with cosmic time. The accumulating H I gas and decreasing SFR may have caused $f_{\rm esc}^{\rm abs}$ to *rapidly drop* over a relatively narrow interval of cosmic time (∼1.5 Gyr), as the LyC flux heats the dust and inhibits the formation of new massive stars. When AGN outflows began to increase after the peak in the cosmic star formation history at $z \sim 2$, their outflows may have cleared enough paths in the ISM of host galaxies to enhance the fraction of escaping LyC radiation produced by massive stars and from the accretion disk, resulting in AGN beginning to dominate the ionizing background at $z \lesssim 2$.

(6) Further data on LyC $f_{\rm esc}$ are essential for both galaxies and weak AGN to confirm both their trends in $f_{\rm esc}^{\rm abs}(z)$. The current samples are still very small, and clearly need further

confirmation through much larger samples, both through deep imaging of wider *HST* fields in the UV and through deeper spectroscopy on fields with high quality existing *HST* data, e.g., with the *JWST* FGS/NIRISS grisms and with NIRSpec (Gardner et al. 2006). Further theoretical work is needed to outline exactly how quickly f_{esc} may have increased toward higher redshifts *and* at fainter luminosities, as well as at lower metallicities and lower dust extinction at higher redshifts, while producing enough escaping LyC photons from faint galaxies to complete and maintain reionization.

This paper is based on Early Release Science observations made by the WFC3 Scientific Oversight Committee. We are grateful to the Director of the Space Telescope Science Institute, Dr. Matt Mountain, for generously awarding Director's Discretionary time for this program. Finally, we are deeply indebted to the crew of STS-125 for refurbishing and repairing *HST*. We thank Drs. George Becker, Renyue Cen, Nimish Hathi, Anne Jaskot, Karen Olson, Michael Rutkowski, Mr. Jacob Vehonsky, and the referee for their useful comments and suggestions for this work. Support for *HST* programs GO-11359, AR-13877, and AR-14591 was provided by NASA through grants from the STScI, which is operated by the Association of Universities for Research Inc., under NASA contract NAS 5-26555.

Appendix A
Critical Testing of our Stacking Procedure and LyC Measurements

We performed various tests on our data to assess the robustness of our LyC stacking method and detections (Section 4). We test the impact of several sources of possible systematic effects or spurious signal and evaluate the overall level of confidence in our quoted uncertainties on the resulting measured LyC signal.

A.1. Detection Tests of the LyC Stacking and Measurements

To verify that residual astrometric offsets and/or trapped electron trails do not significantly affect our measurements, we first *randomly* rotate each of the individual sub-images by integer multiples of 90°, then repeat the stacking described in Section 4.1, as these systematics would be directionally dependent. In Figure 14, we compare our spectroscopic samples to the original LyC stacks (panels (a)–(d)) with the results of our rotation tests (panels (e)–(h)). The detected LyC signal in the rotated stacks does indeed remain consistent with our original stacks within

Table 4
Photometric "Tic-Tac-Toe" Analysis of the LyC and UVC from Galaxies and AGN, and Other Photometry Tests

Filter	z-range	$N_{objects}$	μ_{sky} (mag/″²)	$S_{LyC/UVC}$ (e^-/pix/s)	m.e.$_{S_{LyC/UVC}}$ (e^-/pix/s)	$S_{LyC/UVC}$ (m_{AB})	σ_S (m_{AB})	$\mu_{LyC/UVC}$ (mag/″²)	1-σ_μ (mag/″²)	S/N (Pred.)	S/N (Obs.)
(1)	(2)	(3)	(4)	(5)	(6)	(7)	(8)	(9)	(10)	(11)	(12)
LyC—Galaxies with AGN											
F275W	2.559–3.076	7	25.64	1.48×10^{-5}	4.52×10^{-5}	27.71	0.33	28.59	29.88	3.25	3.29
F336W	3.132–3.917	3	24.82	1.91×10^{-5}	1.21×10^{-4}	27.97	0.69	28.85	29.35	0.91	1.58
UVC—Galaxies with AGN											
F606W	2.559–3.076	7	22.86	1.61×10^{-3}	1.41×10^{-5}	24.97	0.01	25.85	31.0	149.	114.
F775W	3.132–3.917	3	22.64	1.48×10^{-3}	1.47×10^{-5}	24.24	0.01	25.12	30.1	77.5	100.
LyC—All Galaxies											
F225W	2.302–2.450	19	25.46	4.89×10^{-6}	2.54×10^{-6}	28.82	0.56	29.70	30.41	2.90	1.92
F275W	2.559–3.076	14	25.64	6.65×10^{-6}	3.17×10^{-6}	28.58	0.52	29.46	30.27	2.91	2.10
F336W	3.132–3.917	13	24.82	5.86×10^{-6}	6.04×10^{-6}	>29.29	⋯	>30.13	30.10	(1σ)	⋯
All	3.132–3.917	46	25.46	4.02×10^{-6}	2.14×10^{-6}	29.04	0.58	29.92	30.60	1.76	1.87
UVC—All Galaxies											
F606W	2.302–2.450	19	22.86	2.90×10^{-3}	8.99×10^{-6}	24.34	.003	25.22	31.49	181.	322.
F606W	2.559–3.076	14	22.86	2.19×10^{-3}	9.95×10^{-6}	24.64	.005	25.52	31.38	118.	220.
F775W	3.132–3.917	13	22.64	1.13×10^{-3}	7.52×10^{-6}	24.53	.007	25.41	30.85	76.2	150.
All	3.132–3.917	46	22.86	2.51×10^{-3}	7.49×10^{-6}	24.49	.003	25.37	31.69	292.	335.
LyC—AllGalaxies—Rotatedby random $n \times 90°$											
F225W	2.262–2.450	19	25.46	5.05×10^{-6}	2.55×10^{-6}	28.79	0.55	29.67	30.41	2.98	1.98
F275W	2.481–3.076	14	25.64	7.01×10^{-6}	3.18×10^{-6}	28.52	0.49	29.40	30.26	3.07	2.20
F336W	3.110–4.149	13	24.82	4.92×10^{-7}	6.06×10^{-6}	>29.67	⋯	>30.32	30.32	(1σ)	⋯
All	3.110–4.149	46	25.46	4.10×10^{-6}	2.14×10^{-6}	29.01	0.57	29.89	30.60	1.79	1.92
Random empty sky											
F225W	2.262–2.450	19	25.46	2.52×10^{-6}	2.74×10^{-6}	>29.63	⋯	>30.42	30.33	(1σ)	⋯
F275W	2.481–3.076	14	25.64	6.39×10^{-6}	3.71×10^{-6}	>28.62	⋯	>29.50	30.09	(1σ)	⋯
F336W	3.110–4.149	13	24.82	1.18×10^{-6}	6.03×10^{-6}	>29.22	⋯	>31.87	30.10	(1σ)	⋯
All	3.110–4.149	46	25.46	3.94×10^{-6}	2.38×10^{-6}	>29.05	⋯	>29.94	30.49	(1σ)	⋯

Note. (1) WFC3 filter; (2) redshift range (as in Table 2); (3) number of galaxies with reliable spectroscopic redshifts used in each stack; (4) sky surface brightness in AB mag arcsec^{-2} using EXPTIME and MDRZSKY from the FITS header, corrected for the number of tiles in the mosaic; (5)–(6) average sky-subtracted flux and mean error thereon in e^- pix^{-1} s^{-1} over N sub-images in the central 51 × 51 pixel "tic-tac-toe" aperture (see Appendix A.2); (7)–(8) total LyC and UVC flux and error thereon, expressed as AB mag; (9)–(10) average LyC and UVC surface brightness and 1σ error thereon, both in AB mag arcsec^{-2}; (11) S/N of LyC or UVC flux in Column (5), predicted from the WFC3/UVIS or ACS/WFC CCD equation; (12) S/N of LyC or UVC detection in Column (5), observed from the total sky-subtracted LyC (row 1–4) or UVC (row 5–8) flux and corresponding sky subtraction error in Column (6). (These are to be compared with the S/N of LyC or UVC detections within the SExtractor UVC apertures listed in Table 2).

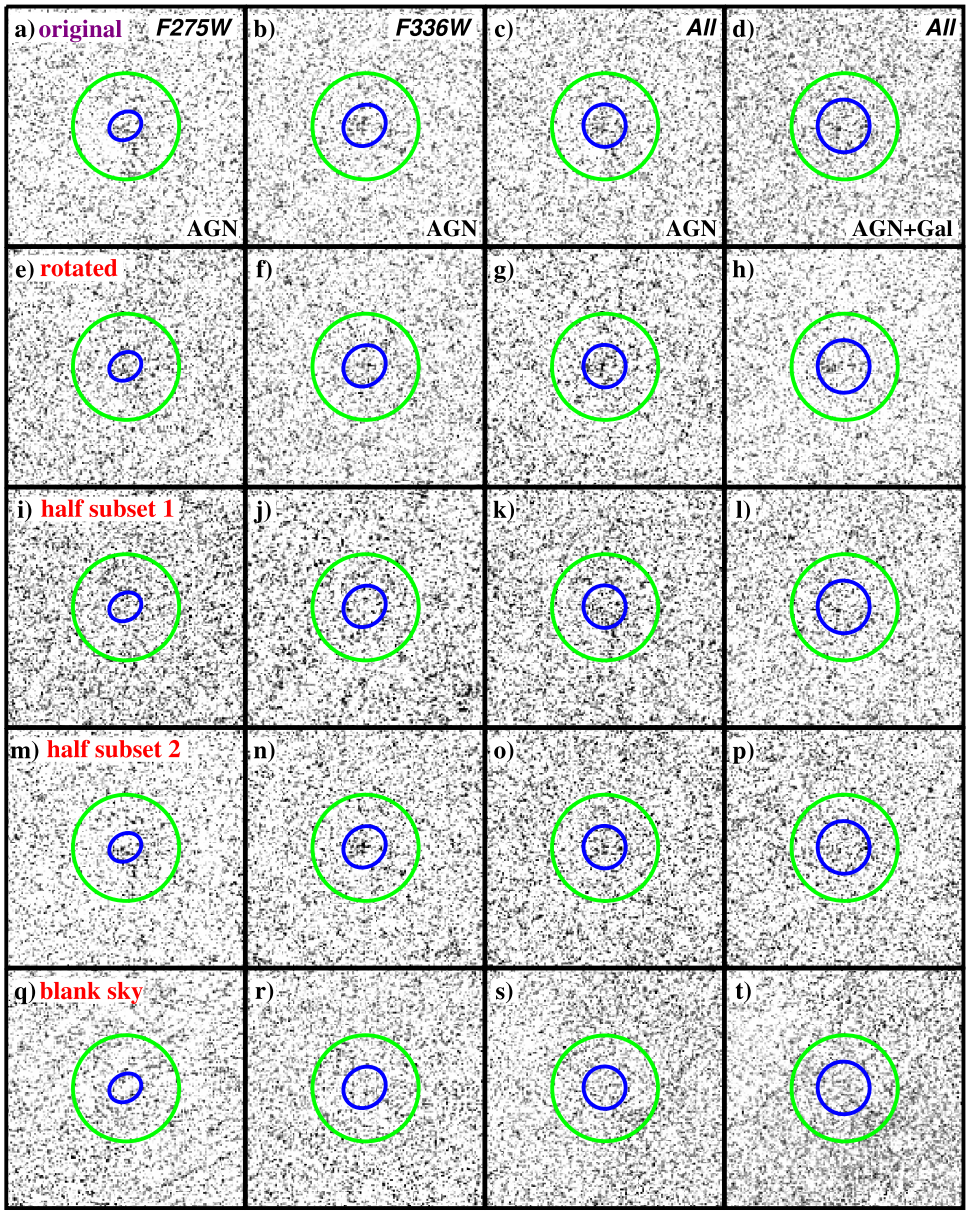

Figure 14. Tests for systematics in our stacking procedure for our stacks that had detections $>2\sigma$. For reference, we show the original stacks that were unaltered in the stacking process in panels (a) through (d). In panels (e) through (h), we present the result of our test with all images rotated over random multiples of 90° before stacking; in panels (i) through (l), we show the result of randomly dividing our sample in two and stacking the first independent subset of images; in panels (m) through (p), we show the complementary stack for the remainder of the images; and in panels (q) through (t), we show that no excess LyC signal is detected in stacks of equal numbers of *random* blank sky areas. The first column display stacks for tests on the F275W AGN sample, the second for the F336W AGN sample, the third for all AGN in our sample, and the fourth for our entire sample of galaxies with and without AGN, where *all* indicates the F225W, F275W, and F336W filters. The meaning of blue and green ellipses is as in Figures 6–8.

0.13 ± 0.15 mag (see Table 4). In the case of F275W, rotation of the images actually *improves* the S/N of the measurement (by ~5%), while the measured photometry remains within ~0.1 mag from that of the original (unrotated) stack. Such an improvement in S/N without significantly affecting the detected flux is most likely due to small-scale residual gradients in the background of the individual sub-images, which, after the random rotations, would average out in a stack. For the F336W filter, this is not the case, and the measured 1σ upper limit actually decreased (by ~0.4 mag) upon random rotation, suggesting that randomizing the surrounding sky may slightly dilute the flux, as small-scale fluctuations in the brighter background of this filter may combine with the central flux in the image (see Table 4). The F225W ERS images were all taken at the end of each orbit—closest to the Earth's limb—since the F225W sky-background was expected to be the faintest. Hence, slight amounts of Earth-shine may have contributed to somewhat larger sky-gradients in the F225W mosaics than in the other filters.

We also extract from the WFC3/UVIS ERS mosaics random patches of *blank sky*, equal in number to the number of galaxy sub-images used for the stacks for each filter. These are combined using the same stacking method, and have the *same* sensitivity to LyC emission as the galaxy stacks. We present the resulting blank sky stacks in the bottom row (panels (q)–(t)) of Figure 14 and their blank-sky "photometry" is tabulated in Table 4. No significant signal is detected at $\geqslant 28.6$ mag (i.e., the central aperture "flux" is present at the $\sigma < 1$ level) in any of the blank sky stacks, which implies that our measured LyC signal in the

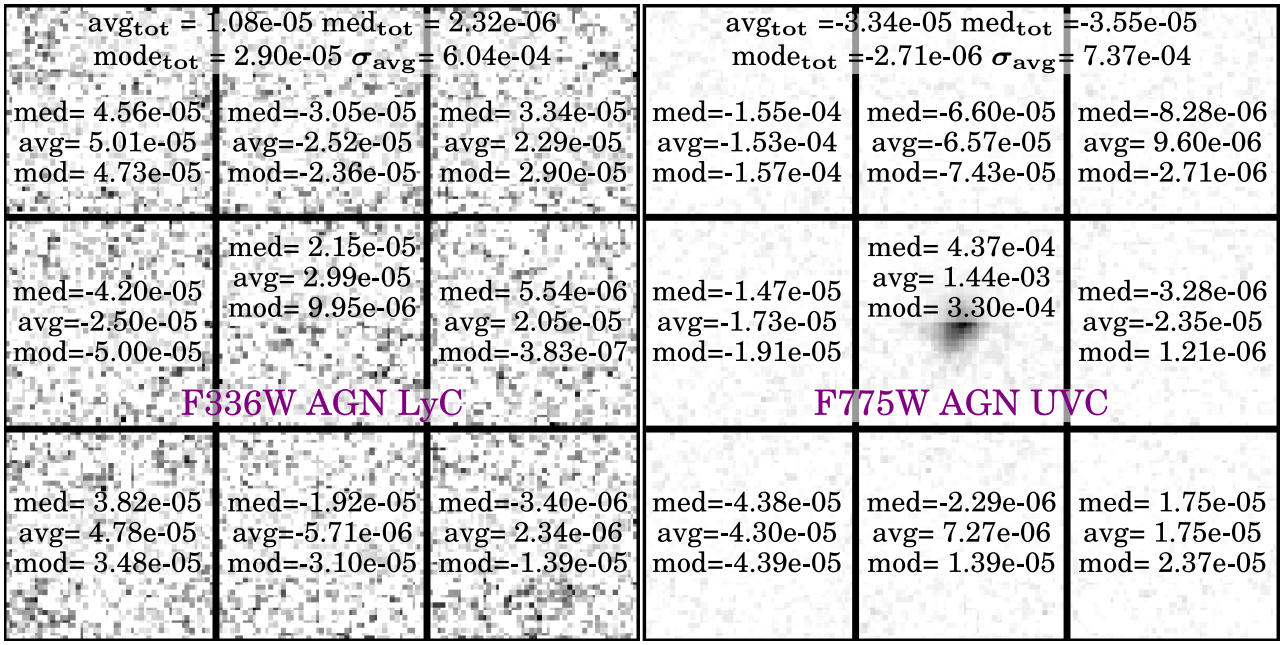

Figure 15. Example of a "tic-tac-toe" sky-background analysis of the 151 × 151 pixel F336W AGN LyC and F775W UVC stacks. Units displayed are in e^-/s for each respective box, and full stack statistics are displayed at the top of the image. (Left nine panels) Stacks of all galaxies and AGN for each filter and a "super-stack" of the entire sample (right nine panels). Any large-scale gradients in the residual sky-background left in the drizzled images are $\gtrsim$5.2–40× fainter than the faint remaining sky-background residuals determined in Figure 3. Such gradients in the sky will be fainter than ∼32.1, 32.0, and 32.4 mag arcsec^{-2} across the 1.″53 "tic-tac-toe" aperture in the WFC3/UVIS F225W, F275W, and F336W stacks. Residual UV sky-gradients appear, therefore, fainter than the LyC signal where this can be measured, as discussed in the text. Not all "tic-tac-toes" used in Table 4 are shown here.

other cases discussed above is most likely real, and associated with objects that were selected at longer (UVC) wavelengths.

A.2. SExtractor versus "Tic-tac-toe" Photometry

It may be of some concern that our use of SExtractor generated UVC apertures for photometric measurements might cause us to miss some amount of extended and faint LyC flux at larger galacto-centric radii, which may be smaller than desired.

We therefore analyzed the flux and S/N within the central 51 × 51 pixels (1.″53 × 1.″53) of a "tic-tac-toe" nine-segment grid with respect to the background level, corrected for residual gradients, determined from the eight surrounding segments. An example is shown in Figure 15. The final columns of Table 4 compare the S/N measured using our "tic-tac-toe" photometry and those measured within the SExtractor LyC apertures. We measure similar fluxes—at slightly lower S/N—using the "tic-tac-toe" aperture compared to the smaller SExtractor fitted apertures and measurements, validating their robustness against modest variations in choice of aperture size, and the specific details of the sky-background subtraction.

The details of our "tic-tac-toe" photometry results are shown in Table 4, which serves to verify the quantities listed in Table 2 for the SExtractor UVC apertures used for LyC detections in Section 4.2. Column 1–3 of Table 4 are the same as columns 1, 2, and 4 of Table 2; column 4 lists the measured ERS sky-background *before* the sky-level itself was removed from each exposure in the AstroDrizzle reduction (for details, see W11 Table 2); columns 5–6 list the sky-subtracted LyC and UVC fluxes and their formal 1σ errors in the central square aperture from the "tic-tac-toe" photometry; columns 7–8 list the resulting total LyC and UVC AB magnitudes measured over the full 1.″53 × 1.″53 "tic-tac-toe" apertures, which are to be compared with the same quantities derived from the SExtractor apertures in columns 6 and 9 of Table 2; column 9 of Table 4 lists the corresponding *average* LyC and UVC SB values inside the 1.″53 × 1.″53 apertures; column 10 lists the 1σ SB error on this value *implied* by the observed total S/N of the LyC or UVC flux, assuming a fully flat SB distribution inside the central "tic-tac-toe" aperture (see Section 5.4); column 11 shows the S/N predicted by the WFC3/UVIS and ACS/WFC CCD equations as a check of the observed S/N derived from the "tic-tac-toe" analysis, which is listed in column 12.

When averaged over the 24 cases listed in Table 4, the S/N predicted by the CCD detector properties is about 0.83 ± 0.62 (rms)× the observed S/N that was derived from the "tic-tac-toe" photometry. This is likely because the S/N predicted from the CCD equation has an uncertain component related to how detector read noise and dark current noise affect the drizzled images in a *correlated* fashion. These noise components are only measured in the original CCD images (see W11 and Dressel et al. (2015) for a discussion of all WFC3 CCD parameters). For the CCD equation prediction of the drizzled mosaics, we assumed that this term would scale with the original/drizzled pixel ratio. Depending on how large a fraction of the read noise and dark current is correlated on scales of a few pixels, this may not be exactly true. In any case, with the above assumption, the predicted S/N for the 1.″53 × 1.″53 "tic-tac-toe" apertures is close to the S/N derived from the observed parameters in the "tic-tac-toe" photometry. More specifically, the observed "tic-tac-toe" S/N values in column 12 of Table 4 are generally close to the S/N derived from the photometry using the smaller SExtractor UVC apertures (see Section 4.2 and Table 2). The exception is the F336W photometry, where the "tic-tac-toe" S/N appears to be lower. This is likely due to the larger amount of higher sky-background and its sky-background gradients included in the "tic-tac-toe" aperture in the WFC3/UVIS F336W filter.

Table 1 lists the measured 1σ SB sensitivity over a 2.″0 diameter aperture in our drizzled WFC3 mosaics. For example,

the F275W filter has a single mosaic 1σ SB sensitivity of $\sim$29.82 mag arcsec^{-2} when measured over a 2.″0 diameter aperture. *If* the sky-background was completely flat without any gradients (but see the discussion in Appendix C.1) then in an 11 object galaxy stack with 8 surrounding "tic-tac-toe" apertures, the quality of the sky-subtraction, or the 1σ SB sensitivity, could in principle be as good as 29.82 mag + 2.5 log($\sqrt{(1.53/2)^2 \times 11 \times 8}$) = 32.0 mag arcsec^{-2}. Here, we scaled the 1σ SB sensitivity with the aperture size, and the rms deviation of the surrounding sky with the number of sub-images and number of available surrounding sky boxes (each of which have their own well measured residual sky values and sky rms; see Figure 15). All of these values are determined *after* image stacking, and are used in predicting the "tic-tac-toe" S/N in Table 4.

This formal limit is better than the measured 1σ SB sensitivity value derived from the "tic-tac-toe" photometry in Table 4 (30.3 mag arcsec^{-2}), which could be due to some correlated or systematic noise present in the actual data. Since subtle residual gradients remain in the sky-background, as discussed in Appendix C.1, the real 1σ SB sensitivity limit that can be achieved is *not as faint* as 32.0 mag arcsec^{-2}. We suggest in Appendix C.1 that uncertainties from subtle residual sky-background gradients in the LyC stacks limit our photometry to $\sim$30.3 mag arcsec^{-2}, so that any LyC SB values measured to be fainter than this should be considered with this limit in mind. For that reason, we do not plot any of the SB values in the LyC light profiles of Figure 10 to levels fainter than 30.3 mag arcsec^{-2}. As quantified in Appendix A.3, the "tic-tac-toe" photometry does confirm the SExtractor photometry from the smaller LyC and UVC apertures discussed in Section 4.2, to within their respective errors.

A.3. Quality of SExtractor versus "Tic-tac-toe" Photometry

When compared to our main photometry using SExtractor UVC apertures in Table 2, the "tic-tac-toe" photometry in Table 4 shows the following: for galaxies, the measured difference in flux within the LyC detected apertures and the 1.″53 × 1.″3 "tic-tac-toe" aperture is Δ(LyC-TTT) = 0.55, when averaged over the F275W and F336W LyC filters for AGN. This difference is not significant, which is possibly another sign of the very flat LyC SB profiles discussed in Section 5.4.

In the "tic-tac-toe" exercise, all contaminating neighbors were removed from the central 1.″53 × 1.″53 "tic-tac-toe" aperture. Nonetheless, it is also possible that some contaminating very low SB flux (invisible in the individual sub-images, even in our deepest WFC3 IR images) from nearby neighbors could have leaked into the larger "tic-tac-toe" apertures. In any case, the above numbers show that the total contaminating flux is likely $\lesssim$0.3 mag, since any contaminating flux should be far smaller in the much smaller LyC apertures (see also Section 4.2).

The "tic-tac-toe" photometry in Table 4 also allows us to further quantify the three other critical tests that were qualitatively discussed in Appendix A.1. For the stack of all galaxies, the "tic-tac-toe" photometry of the sub-images that were randomly rotated by 90° shows a difference with the "unrotated" image stacks of Δ(Rotated–Unrotated) = +0.13 ± 0.15 mag (m.e.) when averaged over the four LyC filters. In other words, the "tic-tac-toe" photometry of the rotated stack is consistent with that of the corresponding unrotated stack, showing that—to within the errors—our stacking method yields reproducible and consistent LyC fluxes.

No signal was detected (at the AB $\gtrsim$ 28.6 mag level) in any of the random blank-sky central "tic-tac-toe" apertures, when compared to the average surrounding sky boxes. These "blank-sky" stacks thus serve as a check on the quality of the UV sky-background subtraction, and the effects of any subtle remaining sky-gradients. They also show that, in random sky areas, no significant amount of flux from cosmic rays residuals that might have not been completely removed during the drizzling process were added in at the at the AB $\simeq$ 28.6 mag level (see Figure 14). Hence, these blank-sky stacks are our best check that even for N = 3–6 one-third to one-half-orbit exposures per filter, the bulk of our stacked, very faint LyC signal at $m_{\rm AB} \sim$ 27.4–28.6 mag (Tables 2 and 4) is not due to residual unfiltered cosmic rays or noise peaks. If this were true, then these random blank-sky stacks would have shown as significant false signal at *similar* $m_{\rm AB}$ levels as the real LyC detections, which was not the case.

Appendix B
Possible Sources of Contaminating Non-ionizing Flux

B.1. In-filter Red-leak of Non-ionizing Flux

The WFC3/UVIS filters were designed to minimize the transmission of photons with wavelengths higher or lower than their specified cutoffs (see Figure 1(a)). However, as seen in Figure 1(b), a small amount of flux red-ward of the Lyman Limit from galaxies observed in these filters with redshifts in the ranges of Table 1 can still leak into the filter and contaminate LyC observations with non-ionizing UVC flux. The lower redshift bounds in Table 1 were carefully chosen such that *no* light >912Å is sampled below the filter's red edge. The filter red edge is defined as <0.5% of the filter's peak transmission. For galaxies at the higher redshifts in the ranges of Table 1, and especially those at higher redshifts than the designated upper bound, the contribution from UVC "red-leak" can become the dominant source of photons measured in the filter, as the portion of the spectrum intended for LyC observation becomes exceedingly faint at shorter wavelengths and the non-ionizing continuum remains roughly constant at longer wavelengths. Thus, in order to accurately measure LyC photometry and escape fractions from these samples of galaxies, we must verify that the flux measured from our sample is dominated by LyC photons.

Since we cannot directly measure the fraction of non-ionizing flux leaking into the filter from the observation, we estimate this value by modeling the contribution of LyC and UVC to the observed flux from the total sample. Using SEDs fit from continuum observations of our galaxy sample and *average* line of sight IGM transmission models (see Section 5.1), we calculate the average UVC "red-leak" of our observation in the WFC3/UVIS F225W, F275W, and F336W filters by comparing the total flux integrated in the entire filter, and the total flux integrated below the Lyman Limit of each galaxy. We calculate this value as:

$$\frac{F_\nu^{\rm UVC}}{F_\nu^{\rm LyC}} = 1 - \sum_{i=1}^{N_{\rm gal}} \frac{\int_{\lambda_{\rm l}}^{\lambda_{912}} \mathcal{T}_{\rm obs}^{\rm LyC}(\nu)\mathcal{T}_{\rm IGM}(z_{\rm i},\nu)F_{\nu,{\rm i}}(\nu)\frac{d\nu}{\nu}}{\int_{\lambda_{\rm l}}^{\lambda_{912}} \mathcal{T}_{\rm obs}^{\rm LyC}(\nu)\frac{d\nu}{\nu}} \Bigg/ \frac{\int_{\lambda_{\rm l}}^{\lambda_2} \mathcal{T}_{\rm obs}^{\rm LyC}(\nu)\mathcal{T}_{\rm IGM}(z_{\rm i},\nu)F_{\nu,{\rm i}}(\nu)\frac{d\nu}{\nu}}{\int_{\lambda_{\rm l}}^{\lambda_2} \mathcal{T}_{\rm obs}^{\rm LyC}(\nu)\frac{d\nu}{\nu}},$$

where $\lambda_{\rm l}$ and λ_2 are the minimum and maximum wavelengths of the full filter transmission curve, λ_{912} is the observed wavelength

of the Lyman Limit of the galaxy, F_ν is the SED flux of the galaxy in erg s^{-1} cm^{-2} Hz^{-1}, $\mathcal{T}_{\rm IGM}$ is the average line of sight IGM transmission at the redshift of the galaxy, and $\mathcal{T}^{\rm LyC}_{\rm obs}(\nu)$ is the combined throughput of the filter, detector QE, and optical telescope assembly (OTA). This value quantifies the fraction of flux we measure from these galaxies in the filter intended for LyC observations that is non-ionizing. For the F225W, F275W, and F336W filters, the *percentage of total* "red-leak" photons that contribute to the measured LyC flux of our sample are ∼0.65%, 0.64%, and 0.19%, respectively. That is, less than 1% of the anticipated and measured LyC flux itself could be red-leak flux from longward of 912 Å. From these values, it is clear that LyC observations of galaxies at the redshift ranges indicated in Table 1 with their respective filters are dominated by LyC photons. We also note that our MC analysis of the observed LyC flux from these galaxies accounts for these "red-leak" photons, in order to make appropriate corrections for low-level non-ionizing contamination of the order of ∼0.28%.

B.2. UVIS filter Pinholes

Pinholes are very small voids in the coating on the surface of a filter. These voids appear usually due to poor adhesion of the coating in these regions where particulate matter on the surface of the filter is coated over when the substrate is cast, or from mechanical abrasion or chemical interactions when the filter is in use. Several of the WFC3/UVIS filters have pinholes, so we must make sure that none of the LyC flux that we measure is due to out-of-band flux leaking in through the filter in an area where such a pinhole exists. Most of the obvious pinholes were known before WFC3's launch, and the filters with the fewest pinholes were chosen for flight (Dressel et al. 2015). To the best of our knowledge, the number of pinholes did not increase during the 7 years that the WFC3 filters were on the ground. Visible pinholes on the selected filters were painted over when possible (Baggett et al. 2006). Any remaining pinholes not painted over before launch are likely $\lesssim$0.2 mm in diameter, or they would have been treated before final instrument assembly. Unfortunately, no record was kept of any less obvious pinholes in the flight filters that were not painted over before launch. Remaining pinholes could cause subtle field-dependent red-leaks and very low-level sky gradients, which we quantify here.

We need to first estimate how large the footprint and the amplitude of any pinhole red-leak on the WFC3 CCDs could be. The *HST* $f/24$ beam gets re-imaged inside WFC3 to $f/31$ (Dressel et al. 2015), so that the plate scale on the WFC3 UVIS detector changes from $3\farcs58$/mm to $2\farcs77$/mm (i.e., $206265/(2400\times 31)''$/mm). The WFC3 UVIS Marconi CCDs have 15 μm pixels, so the two 2k × 4k CCD arrays are about 61 mm in physical size. The WFC3/UVIS F225W filter is in Selectable Optical Filter Assembly (SOFA) filter wheel 3, F336W in filter wheel 4, and F275W in filter wheel 6 out of 12, where wheel 12 is closest to the CCD's. The average location of these three filter wheels is about 190 ± 25 mm away from the focal plane (Figure 2.1 of Dressel et al. 2015), which we hereafter refer to as the "center of the SOFA." The ±25 mm indicates the approximate range over which these three UVIS filter wheels are mounted inside the SOFA. Each SOFA filter is 57.3 mm square and $\lesssim$5.151 mm thick (Baggett et al. 2006), as fabricated by the filter vendor to the specifications defined by the WFC3 Scientific Oversight Committee and Instrument Product Team.

The SOFA is about one-third of the way between the focal plane and the pupil, which is the anamorphic asphere mirror inside WFC3 that corrects for the spherical aberration in *HST*'s primary mirror. Fortunately therefore, all pinholes in the WFC3 UVIS filters will be severely out of focus, since the filters are so far from the focal plane. We first need to calculate how large the pupil of each image is in the filter plane. The anamorphic asphere mirror has a diameter of about 25 mm and is about 630 mm away from the CCD. It is about 440 mm from the center of the SOFA, so that the *radius* of the image pupil at the filter distance is about $r_{\rm ip-f} \simeq (190/630)\cdot 25/2 \simeq 3.77$ mm. Hence, the image pupil at the filter is about $7.54/57.3 \simeq 13\%$ of the filter size.

Next, we need to estimate how large the footprint and the amplitude of any pinhole flux on the WFC3 CCDs could be. If WFC3's $f/31$ beam goes through a pinhole with an $r \gtrsim 0.08$ mm radius (i.e., $\gtrsim 0.5\times 5.151/31$) in a $\lesssim$5.151 mm thick UV filter about 190 mm in front of the CCD, this pinhole will affect a beam with an opening angle $\theta = 90°-{\rm atan}(31) \simeq 1\fdg85$ projected onto the CCD. As viewed from the CCD, the remainder of the pixels outside this beam will not view the sky through the pinhole. At the CCD, the circular beam that *is* affected by this pinhole will have a $190/31 \simeq 6.1$ mm $\simeq 17\farcs0 \simeq 430$ pixel radius on the CCD, and so its diameter will cover about 20% of the WFC3 CCD FOV. To avoid internal reflections in the camera, the UVIS CCDs are tilted by ∼21° with respect to the axis of the beam, so the projected footprint of each pinhole is actually about $430/\cos(21) \simeq 460$ pixels in radius. In other words, the footprint projected by the pinhole on the CCD is very large, and will significantly dilute the extra SB signal projected through the pinhole. In the limit, a much smaller pinhole ($r \ll 0.08$) mm would not see the entire $f/31$ beam, and will thus act like a pinhole camera that illuminates the entire CCD, diluting the extra SB that goes through this smaller pinhole even more.

If the interference or AR coating were not present in a pinhole for one of our WFC UVIS filters, Figure 1(b) shows that it could have a significant increase in local throughput, or less in the case that the local defect was only partial in transmission. In a worst case, the pinhole would act like a F606W or F775W WFC3 filter at that location, if the OTA×Filter-Throughput×CCD-QE at those wavelengths reached the WFC3 maximum in the F606W filter of ∼28% (see Figures 3.2 and 5.2 of Dressel et al. 2015). In such cases, the Zodiacal sky in the beam illuminated by the pinhole would be much higher than seen in our UVIS filters, possibly as high as that in our broadband optical filters, or slightly higher if the pinhole were fully transparent.

The brightest object in the WFC3 ERS has $V \simeq 17$ $m_{\rm AB}$ and the most commonly seen objects are faint galaxies with $V \simeq 26$–27 $m_{\rm AB}$ (Figure 12 of W11). Hence, their collective SB is well below the average Zodiacal background, which is 23.7–22.6 mag arcsec^{-2} (see Column 4 of Table 4). Hence, for all practical purposes, the pinhole contribution will just be the full white light Zodiacal background if its throughput reaches the maximum total throughput of ∼28%. Following Table 4, we assume that the white light Zodi would have on average a SB ≃ 22.9 mag arcsec^{-2} through such a pinhole, which is roughly the observed value in F606W (see W11). We will also consider the case of a single $V \simeq 17$ $m_{\rm AB}$ star shining behind a pinhole, as well as the integrated sky SB derived from the faint galaxy counts in Figure 12 of W11 to $m_{\rm AB} \lesssim 26$ mag. In F606W, the latter reaches 10^5 galaxies/0.5 mag deg^{-2} to $m_{\rm AB} \lesssim 26$ mag, and in F275W, they reach 3×10^4 galaxies/0.5 mag deg^{-2} to

$m_{AB} \lesssim 25.5$ mag. On a per square arcsecond basis, the integrated sky SB from faint galaxies is therefore ~29.3 mag arcsec^{-2} in F606W and ~30.1 mag arcsec^{-2} in F275W, respectively, i.e., fully negligible compared to the Zodiacal sky SB values from Table 4 of $SB_V^{Zodi} \simeq 22.9$ and $SB_{NUV}^{Zodi} \simeq 25.5$ mag arcsec^{-2} in these filters, respectively. Hence, only the Zodiacal light and the effective SB of the occasional bright star behind the filter would be the main sources of pinhole contamination. All calculations below are done in terms of surface brightness (SB in mag arcsec^{-2}) or intensity (I in relative counts s^{-1}).

In a slow $f/31$ beam, when the pinhole is larger than the minimum size to transmit through the filter, the total white light transmitted would increase proportionally to the pinhole area compared to the total area of the image pupil at the filter $(r_{ph}/r_{ip-f})^2$, both measured in mm. For an untreated pinhole with an assumed $r_{ph} \simeq 0.1$ mm, we can now estimate the increase in sky SB contribution from this pinhole over a $r = 460$ pixel radius on the CCD. In relative units, this is increase is:

$$I_V^{ph} = F \cdot [r_{ph}^2/r_{ip-f}^2] \cdot [I_V^{Star} + I_V^{Zodi}] \quad (6)$$

with $I_V^{Star} = 10^{-0.4(SB_V^{Star} - ZP_V)}$, $I_V^{Zodi} = 10^{-0.4(SB_V^{Zodi} - ZP_V)}$, and:

$$I_{NUV}^{ph} = [(r_{ip-f}^2 - r_{ph}^2)/r_{ip-f}^2] \cdot [I_{NUV}^{Star} + I_{NUV}^{Zodi}] \quad (7)$$

$I_{NUV}^{Star} = 10^{-0.4(SB_{NUV}^{Star} - ZP_{NUV})}$, $I_{NUV}^{Zodi} = 10^{-0.4(SB_{NUV}^{Zodi} - ZP_{NUV})}$. Eq. (6) describes the relative counts of optical white light through the pinhole, and Equation (7) the relative counts for the uncorrupted NUV sky SB. Note that the optical white light $SB_V^{Zodi} \simeq 22.9$ mag arcsec^{-2} is compared here to the WFC3 F606W zero-point of $ZP_V = 26.08$ mag (i.e., *not* the ACS ZP in this case), and the original UV $SB_{NUV}^{Zodi} \simeq 25.5$ mag arcsec^{-2} (Column 4 of Table 4) is compared to the combined F225W and F275W zero-points of ~24.1 mag. The factor $F \simeq (10000 - 4000)/2000) \simeq 3$ reflects that the pinhole could transmit three broadband filters worth of white light from 4000 to 10,000 Å (see Figure 1(b)). We find approximately the same values if we instead use the WFC3 white light filter F200LP and its zero-point ZP = 27.36 mag, and set the factor $F = 1$. The limit of $r_{ph} \simeq r_{ip-f}$ would describe a hypothetical pinhole so large that it transmits full white light over the entire image pupil at the filter, which now acts like a wide V band filter. In that case, both equations still give the correct results: Equation (6) describes its wide V band SB, and Equation (7) describes its now vanishingly small NUV SB.

At first, we ignore the terms with I_V^{Star} and I_{NUV}^{Star} due to a bright star near a pinhole. The SB from the pinhole in V and NUV then are $I_V^{ph} \simeq 0.039$ and $I_{NUV}^{ph} \simeq 0.28$ in the same relative units, respectively. The ratio I_V^{ph}/I_{NUV}^{ph} is 0.14, so that about 14% of white light background through the pinhole gets added to the UV sky:

$$SB_{NUV}^{Sky} = SB_{NUV}^{Zodi} - 2.5 \log(I_V^{ph}/I_{NUV}^{ph}). \quad (8)$$

The error on this is at least $25/190 \sim 0.13$ mag, depending how far the SOFA filter is from the CCD. That is, a full white light pinhole footprint could add ~14 ± 2% to the sky SB over an annulus with a diameter about 20% of the 61 mm CCD area. This is the worst case—a smaller pinhole that doesn't project the entire $f/31$ beam through the filter could instead add a much fainter SB over the whole chip.

If we also add the effect from a $m_V^{Star} \simeq 17$ mag, $m_{NUV}^{Star} \simeq 18$ mag star whose image pupil in the filter plane illuminates the pinhole, we must first correct for the fact that the light from this point source is now spread out by factor of $(r_{ip-f}/r_{ph})^2$ at the filter, so we must add $2.5\log(3.77/0.1)^2$ to the star's point source flux of $m_{AB} \sim 17$–18 mag in Equations (6)–(7) to get the equivalent SB from the star that actually affects the pinhole, expressed in the appropriate relative units. Note that the Zodiacal background and integrated galaxy counts do not have this problem, since they are already expressed as proper SB in Equations (6)–(7). These numbers are $SB_V^{Star} \simeq 24.9$ and $SB_{NUV}^{Star} \simeq 25.8$ mag arcsec^{-2}. Equations (6)–(7) convert these SB numbers to relative fluxes, then add them linearly. With a $V \sim 17$ mag star, the white light SB from the pinhole now grows from $I_V^{ph} \simeq 0.039$ to $I_V^{ph} \simeq 0.046$. This is only 17% larger than just the light from Zodiacal light alone, since the star is so much more spread out behind the filter. The NUV comparison term remains at $I_{NUV}^{ph} \simeq 0.28$. Hence, an out of focus image of a $V \sim 17$ mag star behind the pinhole adds ~17 ± 2% of white light background to the NUV sky.

To first order, both the proper NUV light and any white light pinhole flux would get flat-fielded away, although the pinhole regions would have a different color of the sky-background than the regular UV sky. The WFC3 UVIS Marconi CCDs have QE curve that is fairly flat as a function of wavelength, with most QE values between 2000 and 8000 Å peak around QE ~ 70% with a range of ±10%. This peak actually lies within the F275W filter. We therefore did the experiment to flat-field a WFC3 F606W image with a high S/N flat-field taken in the F275W filter, and—owing to WFC3's flat QE curve—this did not result in a residual gradient larger than about 10% of sky corner to-corner across the whole CCD frame. Below we will assume a worst case of ~10%.

We can use this result to compute the additional sky gradient that an unpainted pinhole with $r \simeq 0.1$ mm could have caused in our UV images. When a pinhole adds about 14%–17% extra flux to the regular UV Zodiacal sky over a 920 pixel diameter circle on the CCD, the residual sky gradient that the improper flat-fielding induces is at most 0.6%–0.8% of the *total* Zodiacal sky over 920 native pixels, or about 404 drizzled pixels. Across our sub-image size of 71 × 71 drizzled pixels, this residual sky gradient—if present in our object sub-images—is thus less than ~0.22%–0.26% of the local Zodiacal sky. That is, the error in the UV sky of Equation (8) from sky gradients induced by the partial improper flat-fielding of any pinhole white light is:

$$\sigma_{Sky} \simeq SB_{NUV}^{Sky} + 2.5 \log(I_V^{ph}/I_{NUV}^{ph} \cdot 0.1 \cdot 71/404). \quad (9)$$

For our average UV sky of 25.36 mag arcsec^{-2} (which is now brightened by −0.14 mag due to the extra pinhole flux), the residual sky-gradients left by pinholes in 71 × 71 drizzled pixels are thus fainter than 25.36–2.5 log(0.22%) ≃ 31.9 mag arcsec^{-2} and fainter than ≃31.7 mag arcsec^{-2} if a $V \simeq 17$ mag star is also nearby the pinhole. These pinhole-induced systematics are at worst slightly brighter than those possibly caused by subtle residual gradients left at the 32.3 mag arcsec^{-2} level across the CCD's due to remaining errors in the bias, dark frames, or flat-fields, as discussed in Section 2.3 and Appendix C.1). Of course, the latter may affect our stacks everywhere in the CCD mosaics, while the former occur only in sporadic (although unknown) locations.

We investigated if the effects of any pinhole red-leaks were in fact seen in the ERS data, since obvious pinholes would appear as large donut shaped objects in the drizzled images. No obvious defects with $\gtrsim$14%–17% increased transmission were seen in the raw ERS data on scales of ~920 native pixels, although this is hard to see due to cosmic rays and the shallow depth of individual images. Partial transmission defects might exist at lower levels. As discussed in Section 4.1, we inspected all LyC sub-images individually, and removed the ones with suspected increased noise due to residual cosmic rays, structure in the weight maps due to drizzled image borders, and other image defects. The objects removed from the LyC stacking all appear to have higher image rms due to the proximity of structure in the weight maps due to drizzled image borders. No obvious enhancements in the LyC signal were seen due to the proximity of bright stars.

We find that both red-leak flux from UV filter pinholes and other subtle calibration errors may result in residual sky gradients of order ~32–32.3 mag arcsec^{-2} across our stacking sky boxes. Unless these effects can be removed through further refinement of the WFC3 calibration techniques, residual systematic subtraction errors of order $\simeq$32 mag arcsec^{-2} may well pose a fundamental limit to the LyC stacking method of WFC3 data. This is why the light profiles in Figure 12 cannot be extended to SB levels much fainter than AB $\simeq$ 32 mag arcsec^{-2} (see also the discussion in Appendix A.2 and Table 4).

Finally, if our LyC detections were in fact caused by subtle sky gradients on $r \simeq 920$ pixel scales, they should have been *preferentially* located near the same physical regions of the CCD, as would have been the case with CTE effects if these had been already significant in Figure 16. We saw no evidence of our strongest LyC candidates being located in the same physical CCD region of each exposure. On the contrary, our strongest LyC emitters are known "galaxies with weak AGN" (Table 2), and show no correlation in their observed position on CCDs. On average, their LyC flux is brighter than that of our "galaxies without AGN." The AGN LyC flux is sometimes compact ($\lesssim$ a few pixels; Figure 8)—as opposed to that of the galaxies (see Figure 7)—and therefore occurs on too small of an optical scale to be caused by the severely out of focus red-leak through pinholes. Thus, since the physical location of the AGN on the CCDs is spatially uncorrelated, their enhanced LyC flux is unlikely associated with residual sky-background gradients from pinholes. Had that been the case, a number of our much more numerous "galaxies without AGN" would likely have also been exposed near pinhole-induced sky gradients and shown the same amount of red-leaked flux, which is not the case. Hence, local residual sky-background gradients due to pinhole induced red-leak enhancements are not likely to have affected our LyC measurements, at least not to the level of AB $\simeq$ 32 mag arcsec^{-2}.

B.3. Estimating LyC Contamination from Objects Below the χ^2 Image Detection Limit

Here we estimate the potential non-ionizing contamination to our LyC stacks from interloping objects below the χ^2 image detection limit. As seen in Section 4.1, the deepest χ^2 images allow us to locate possible low-redshift contaminants in sub-images to AB ~ 27.5 mag, such that they can be removed from our stacks so they cannot contribute any flux to our photometry. However, the possibility of fainter objects that may remain undetected in χ^2 detection image must be addressed, since those objects could potentially contribute some flux within the SExtractor aperture photometry.

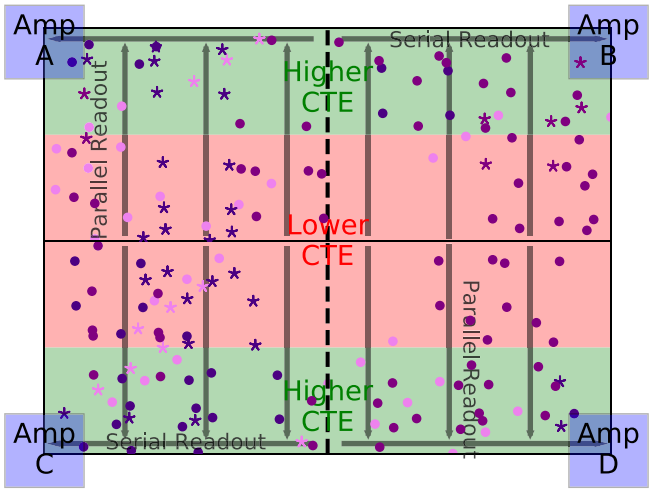

Figure 16. Detector layout and observed location of galaxy subsamples. WFC3/UVIS F225W, F275W, and F336W images. The two 2k × 4k CCDs are shown as the rectangular panels that stretch from $X = 1$ to 4096 and $Y = 1$ to 2051 pixels. Within each WFC3 CCD, the green regions indicate the half of each CCD quadrant that is closest to the corresponding read-out amplifier along the parallel read-out direction, while the red regions indicate the half that is furthest away and will undergo more transfers along the array. The colored circles mark the positions in physical WFC3/UVIS CCD coordinates of each of the $z \simeq$ 2.3–4.8 galaxies with HQ spectra in our sample. Filled circles mark objects where visible flux is seen in the individual LyC sub-images. The subsamples of objects in the green and red regions are referred to as our "high-CTE" and "lower CTE" subsamples, respectively. Averaged over all objects, the difference between the stacked LyC signal in the "high-CTE" are compared to the "lower CTE" area is Δ(High-CTE–Lower-CTE) $\simeq$ +0.22 mag. This suggests that the CTE induced systematics are not yet larger than the rms error and other systematics in the photometry. Since the circles (galaxies without AGN) and stars (galaxies with AGN) are fairly uniformly distributed across the CCD, CTE degradation must have not yet been a major limitation in detecting the faint LyC signal four months after the WFC3 installation.

As an example, the F336W stack LyC photometry is taken within an aperture area of ~0.5 arcsec^2 (see Table 2). To assess this fainter contaminating flux, we need to estimate to the total F336W stack sky-surface brightness from objects undetected at AB $\gtrsim$ 27.5 mag. For this, we will use the galaxy counts of Driver et al. (2016) from 20 filters ranging from $\lambda \simeq$ 0.15–500 μm. At nearly all wavelengths, their normalized differential counts (Figure 8 or A1 in the on-line version only) converge with a well-determined slope of $\frac{\Delta\rho_L}{\Delta m} \simeq$ –0.177. The total sky-surface brightness contributed by each magnitude bin in the F336W counts peaks at AB $\simeq$ 24 mag. The faintest galaxy counts that contribute in F336W are the UVUDF counts in the HUDF (Teplitz et al. 2013), which reach AB ~ 28 mag. Driver et al. (2016) performed MC tests to determine the uncertainty in the extrapolated total sky-signal, which is $\lesssim$20% in F336W.

We will extrapolate this converging signal with the same slope as measured between AB $\simeq$ 24 and AB $\simeq$ 28 mag to arbitrarily fainter fluxes, e.g., from 27.5 mag to 38 mag. This is the F336W flux that a very dim ($M_{AB} \simeq$ –10 mag) galaxy would have at $z \simeq 3$, where the distance modulus in Planck 2016 cosmology is DM = 47.47 mag. The actual F336W sky-brightness in Driver et al. (2016) drops from ~$10^{-28.3}$ W Hz^{-1} m^{-2} deg^{-2}(0.5 mag^{-1}) at AB = 27.5 mag to ~$10^{-30.2}$ W Hz^{-1} m^{-2} deg^{-2}(0.5 mag^{-1}) at AB = 38.0 mag. Over the 21 contributing 0.5 mag-bins from AB = 28 to AB = 38 mag, this sky-integral is ~10^{-28} W Hz^{-1} m^{-2} deg^{-2} or 1.85×10^{-9} Jy arcsec^{-2}, or 30.73 mag arcsec^2.

Within the 0.5 arcsec^2 SExtractor aperture, the contribution of contamination from *unresolved, unseen* galaxies between AB = 27.5–38 mag amounts to a total integrated flux of AB = 31.5 mag. This is well below the level of our AGN LyC detections in Table 2 and also fainter than our 1σ sky-subtraction errors in in Table 4 (Column 10). Any such contaminating flux from unresolved objects at AB $\gtrsim$ 27.5 mag will also be present in the eight neighboring sky-apertures in Figure 15, and so would be statistically subtracted to first order. Thus, after subtracting all detectable contaminating neighbors at AB $\lesssim$ 27.5 mag using the χ^2 images, statistically the LyC signal is not significantly affected by contaminating objects below the *HST* χ^2 image detection limit of AB $\sim$ 27.5 mag.

Appendix C
Sources of Systematic Uncertainties

C.1. Impact of Gradients in the Residual Sky-background

Subtle gradients still exist in the new ERS UV mosaics, but at a much reduced level from the v0.7 ERS mosaics of W11. These are $\lesssim$3%–5% of the Zodiacal sky values from *corner to corner* across each of the eight individual 4096 × 4096 pixel CCD images that were drizzled onto the UVIS mosaics. This subtle gradient pattern was not very discernible, but appears to be similar in each of the eight full WFC3/UVIS CCD frames in the ERS to a good approximation, and roughly linear across each CCD. The cause of these remaining gradients could be subtle residual errors in the on-orbit master bias frames, in the delta-flat corrections used in the recent WFC3 pipeline reduction, and/or from variation in exposure time or background noise across the drizzled mosaic (Baggett & Anderson 2012; Mack et al. 2013). These remaining gradients are too faint to accurately map and remove from individual WFC3/UVIS UV exposures prior to drizzling, and removal of inaccurately measured gradients would introduce additional unintended errors in the mosaics. We therefore will assess the effects that these 3%–5% global gradients have on the $\lesssim$151 pixel scales at which local sky-subtraction is performed in the LyC image stacks.

Dividing each LyC stack into our nine-segment "tic-tac-toe" grid, we determine the sky-background level and uncertainty in each of the eight segments around the central box that contains the LyC candidate itself, which we exclude from the sky-background calculation. We compute these by optimally binning the count rates of the eight outer segments, then we fit a normal distribution to the inner quartile of this data, taking the average of the fitted distribution as the sky value and the +1σ value to be the 84% of the pixel histogram. We estimate the gradients in the stacks from the rms value of the fitted average count rate in each segment. As shown in the examples of our "tic-tac-toe" photometric analysis in Figure 15 and tabulated in Table 4, we find that any residual sky-background *gradient* left in the image stacks is ∼5.2–40 × (∼1.8–4 mag) fainter than the residual sky-background numbers derived from Figure 3. This then implies that *any* gradients in the local sky-background in the LyC image stacks (containing 13–19 objects each) are fainter than ∼32.3, 32.1, and 32.5 mag arcsec^{-2} in WFC3/UVIS F225W, F275, and F336W across the 4.″53 × 4.″53 extent of each sub-stack, respectively.

These numbers are consistent with the aforementioned ∼3%–5% linear gradient across each of the full WFC3/UVIS mosaic images *before drizzling*, and corresponds to a $\lesssim$0.2% error in the sky-subtraction across typical 151 × 151 pixel sub-image stacks. For a UV sky brightness of $\mu_{\rm sky} \sim 25.5$ mag arcsec^{-2} (see Table 4), this amounts to a sky-subtraction error of ∼32.3 mag arcsec^{-2} across a 151 × 151 pixel stack. One possible source of such gradients are residual dark current subtraction errors. Rafelski et al. (2015) show that the 2009 WFC3/UVIS dark current may vary between 0.00045 e^-/s and 0.00035 e^-/s across the CCDs (black curve in their Figure 15). From experience, the quality of the calibration files is such that these gradients are typically subtracted at the level of (conservatively) ∼20% of the gradient itself. That is, this dark current subtraction error across the 151 pixel "tic-tac-toe" sub-images (out of 4096 pixels across the two CCDs) will amount to a residual sky subtraction error in the subimages of approximately: $-2.5 \log [0.20 \times ((0.00045/0.00035)\text{-}1)*151/4096] \simeq 6.7$ mag below sky. This could then leave a residual dark current gradient on top of the UV zodiacal sky (25.5 mag arcsec^{-2}) of 25.5+6.7 = 32.2 mag arcsec^{-2}, consistent with the limits given above. This level of uncertainty in the local sky-background level may pose a fundamental limit on the sensitivity and accuracy of any LyC (surface) photometry, which is slightly fainter than that potentially imposed by pinholes. The systematic nature of these residual gradients also explains the slight improvement in S/N noted in Appendix A.1 when the individual F225W sub-images are rotated by random multiples of 90°. These residual gradients are also much fainter than the measured LyC signal (see Table 4).

C.2. Assessment of Possible WFC3/UVIS CTE Degradation $\lesssim$4 Months After Launch

Charge Transfer Efficiency (CTE) degrades over time due to high-energy cosmic ray collisions with the detector, and from encounters with relativistic protons and electrons during *HST*'s frequent passages through the South Atlantic Anomaly. Particle damage to the silicon of the CCD can cause areas where electrons become trapped in the detector's crystal lattice during readout of the array. The WFC3/UVIS detectors suffer from a CTE loss of ∼0.1 mag per year. After several years in orbit, faint objects ($\lesssim$300 e^-) can lose up to 50% of their flux during readout (Noeske et al. 2012; Bourque & Kozhurina-Platais 2013). CTE degradation can also cause charge trails to be visible in the images, caused by the delayed release of trapped electrons during readout. Partial recovery and correction of CTE losses in post-processing of the images is only possible for brighter sources (Anderson & Bedin 2010; Massey et al. 2014). Flux from very faint objects cannot be corrected in this manner, as their low electron counts are lost in the background noise of the detector. Because the WFC3 UV data were taken less than four months after Shuttle Servicing Mission SM4 that installed WFC3 onto *HST*, the WFC3/UVIS ERS data may not yet suffer from significant CTE losses.

The CTE may be lower in some regions further away from the amplifiers at the beginning of readout due to any existing electron traps first being filled nearest to the amps during readout. However, this effect is very nonlinear, as the traps have an unknown probability of capturing and releasing electrons per each charge transfer, so electrons further away from from the amps might encounter more traps if the captured electrons are released before the last columns are read out. Thus, the *cumulative* CTE will be higher on average closer to the amps when combining all CTE effects along the *parallel* readout direction.

Figure 16 provides an overview of the WFC3/UVIS readout configuration (see Figure 6.14 of Dressel et al. 2015). The two 2k × 4k WFC3/UVIS CCDs are shown as rectangular panels in Figure 16, displaying the total pixel arrays from X = 1–4096 and

Table 5
Assessment of the Impact of CTE Effects for Galaxies with HQ+IQ Spectra

Filter (1)	z Range (2)	$\langle z \rangle$ (3)	N_{obj} (4)	m_{LyC} (5)	S/N_{LyC} (6)	A_{LyC} (7)	m_{UVC} (8)	S/N_{UVC} (9)
All Galaxies, Higher CTE Area								
All	2.298–4.149	2.785	30	28.78	1.41	0.76	24.60	445
All Galaxies, Lower CTE Area								
All	2.276–4.120	2.764	28	28.56	1.67	0.75	24.63	409

Note. Table columns are as for Table 2.

$Y = 1$–2051 pixels. Within each WFC3/UVIS chip in Figure 16, the green band indicates the half of each CCD *closest* in the parallel read-out direction to the four corresponding amplifiers (labeled as Amp A, B, C, D, respectively), where the cumulative CTE degradation effects from CR and relativistic particle hits accumulated on-orbit are expected to be *lowest*. We refer to this higher CTE region as the "higher CTE" area. The red bands in each chip indicate the half of each WFC3 CCD *furthest* from the amplifier in the Y read-out direction, where the effects from CTE *degradation* would be more substantial. The cumulative CTE value itself from these areas will be lower compared to the "higher CTE" regions, since its signal will have on average been read-out through more charge transfer rows. We refer to this region as the "lower CTE" area.

The colored circles and stars in Figure 16 show, *in physical WFC3/UVIS CCD (X, Y) coordinates*, where all our galaxies without and with AGN, respectively, at $z \simeq 2.3$–4.1 were observed in all individual exposures within the CCDs for WFC3/UVIS. We note that the galaxy sample was specifically selected to have high reliability in spectroscopic redshifts (see Section 3.1 and Tables 2–3), therefore any apparent spatial correlation of the objects in the CCD coordinates is not due to CTE degradation but from the spectroscopic object selection.

There are four drizzled exposures in both WFC3/UVIS F225W and F275W and three exposures in WFC3/UVIS F336W. Every object with a spectroscopic redshift to AB $\lesssim 25$ mag is therefore plotted up to 11× in the WFC3/UVIS in Figure 16 to monitor their actual locations in the individual WFC3/UVIS F225W, F275W, and F336W exposures. The somewhat apparent clustering of ERS galaxies with the most reliable redshifts in Figure 16 is caused by this repetitive plotting of the individual locations of the galaxies in each exposure, overemphasizing the appearance of any real clustering in the mosaic. It is possible that the way the VLT and other spectroscopic masks were configured to observe galaxies for redshift measurements—while maximally avoiding spectral overlap—further introduced some apparent clustering in a particular region of Figure 16. Since the VLT spectroscopic masks are comparable in size to the WFC3 FOV, it is possible that the objects who received the most integration time during spectroscopy were more preferentially selected to be on one side of the FOV to minimize the spectral overlap.

With these two separate regions subdivided by their aggregate CTE, we can now determine if and how much the LyC measurements vary based on their location within each chip, and if CTE was already significantly degraded in the September 2009 WFC3/UVIS mosaics less than four months after WFC'3s launch. Similar to our randomly subdivided test stacks in Appendix A.1, we combined these two subsamples in each filter to compare their photometry, background, and noise levels. Some objects appear both in the "higher CTE" and "lower CTE" areas of Figure 16, which occurred due to the dithering of the individual WFC3/UVIS ERS exposures. These objects were added to the corresponding sub-stacks for assessing the effects from CTE degradation. Figure 16 shows that about as many objects with spectroscopic redshifts are located in the green ("higher CTE") areas as in the red ("lower CTE") areas, allowing us to make a quantitative comparison between the two subsets to assess the possible effects of differential CTE across the detector.

The results for the two CTE subsamples are shown in the bottom two sets of rows in Table 5. From these measurements, as a function of relative position on the CCDs, it is clear that each of these two CTE subsamples still yields LyC detections, with correspondingly larger errors due to the smaller number of objects in each sub-sample. In particular, the LyC flux in the "lower CTE" sub-sample remains at least as significant as it is for the "higher CTE" sub-sample: on average, the LyC flux in the "lower CTE" sub-sample is 0.22 mag brighter than in the "higher CTE" sub-sample (Table 2). This differences in photometry between the "higher CTE" and "lower CTE" subsamples—as averaged over the four filters—is not significant, but its sign is such that the "lower CTE" sub-sample is actually somewhat brighter than the "higher CTE" sub-sample. *Therefore this difference does not point to significant WFC3 CTE effects as of 2009 September.* The difference also varies fairly randomly between the four filters, showing no general trend with Y position on the CCD's. Small differences in the observed LyC flux from the two different regions on each CCD may also be caused by some intrinsic variation of LyC f_{esc} between the two subsamples, and/or by the small number statistics available in both subsamples in general. Thus, any CTE induced systematics four months after WFC3's launch are not yet larger than the random errors in the faint LyC signal. This is consistent with the decline in CTE of ∼0.1 mag/year measured by (Noeske et al. 2012; Bourque & Kozhurina-Platais 2013).

The AGN stacks are typically brighter than the stacks without AGN. This information allows us to do a simple statistical analysis to see if CTE degradation has already affected the fraction of objects with, on average, brighter LyC flux between the "higher CTE" and "lower CTE" areas of the WFC3 CCDs. For this, we used the total of 12 AGN and 36 galaxies with no AGN (Table 2) covered by WFC3 UVIS images in the filters F225W, F275W, and F336W, respectively. Since these were taken in four, four, and three dither points each, this resulted in $4 \times 2 + 4 \times 7 + 3 \times 3 = 45$ stars in Figure 16 for AGN, and $4 \times 17 + 4 \times 7 + 3 \times 10 = 126$ circles for galaxies, or a total of 171 points, 82 of which are in the "higher CTE" area, and 89 in the "lower CTE" area.

Of these points indicated in Figure 16, 21/45 or ∼47% occurred in the "higher CTE" area and 24/45 or 53% occurred in the "lower CTE" area. Since the circles are fairly uniformly distributed across the both individual WFC3 CCDs and AGN exist in regions furthest away from the readout amplifiers, CTE

must have been high enough for these faint detections to survive the multiple transfers during readout without becoming trapped in the detector. Hence, the WFC3 UVIS data has not suffered from CTE effects that affected the possible fraction of LyC detections within four to five months after launch for WFC3.

Both of these tests suggest that, less than four months after WFC3's launch, CTE degradation in the UVIS chip is not yet at a level that significantly affects the readout and subsequent photometry of faint flux to within the errors of our measurements, nor has it biased the distribution of objects with marginal individual LyC detections across the CCD. If this had been the case, we would have seen significantly larger differences in LyC flux across the two CCD detectors in the parallel readout direction, and would in fact have seen faint objects fully disappear into the noise in the "lower CTE" regions in Figure 16, in addition to visible charge trails for all brighter objects, none of which appear in our data.

Appendix D
Modeling and Uncertainties

D.1. SED Fitting Uncertainties due to Extinction

In order to obtain accurate estimates for LyC and UVC dust extinction and subsequent absolute LyC escape fractions, we

Table 6
List of Individual Galaxies Reliable Spectra

R.A. (J2000.0) (deg)	Decl. (J2000.0) (deg)	z	$m_{I,\mathrm{AB}}$ (mag)	$M^{\mathrm{AB}}_{1500\text{Å}}$ (mag)	$(V-I)$ (mag)	AGN?
53.006583	−27.724170	2.7212	22.737	−21.20	0.131	yes
53.008846	−27.724348	2.7260	23.919	−19.72	0.811	yes
53.012648	−27.747244	2.5730	23.698	−19.33	0.683	yes
53.013515	−27.755235	3.2171	24.381	−21.30	−0.023	yes
53.013889	−27.756827	2.3170	23.705	−21.32	−0.098	no
53.014539	−27.727922	3.1320	24.114	−21.12	0.283	no
53.020573	−27.742150	3.4739	23.417	−22.23	0.169	yes
53.020927	−27.770185	3.9170	24.484	−21.60	0.598	no
53.033326	−27.782577	2.6123	24.043	−20.11	0.241	yes
53.034441	−27.698210	2.4700	24.552	−19.77	0.094	yes
53.035231	−27.744125	4.1486	25.388	−20.91	0.559	no
53.040821	−27.719068	2.3021	22.509	−21.80	0.133	no
53.042456	−27.737862	2.3036	22.956	−21.25	0.097	no
53.062429	−27.735634	2.6730	25.336	−19.01	0.220	no
53.065221	−27.742901	2.6160	23.539	−21.40	0.061	no
53.065771	−27.695980	3.6433	24.415	−21.15	0.381	no
53.072558	−27.744441	2.6503	24.402	−20.86	−0.108	yes
53.078023	−27.731020	2.4160	23.373	−20.82	0.165	no
53.078800	−27.693745	2.3060	24.363	−20.29	−0.033	no
53.079284	−27.691368	2.4352	23.072	−21.01	0.143	no
53.095384	−27.687524	3.3565	24.771	−20.82	0.230	no
53.100815	−27.715987	2.2980	23.162	−20.15	0.142	yes
53.102783	−27.759367	2.3115	23.792	−21.15	−0.046	no
53.113001	−27.745551	2.3230	24.272	−19.73	0.081	no
53.117831	−27.734305	3.2560	22.767	−21.90	0.408	yes
53.120610	−27.736585	3.3680	24.630	−21.25	0.186	no
53.121611	−27.672921	3.3083	24.994	−20.76	0.095	no
53.131718	−27.669018	3.0762	23.951[a]	−21.88	0.133	no
53.134558	−27.690656	2.3200	22.968	−21.72	0.057	no
53.134819	−27.713359	2.4300	23.143	−20.87	0.184	no
53.138759	−27.700469	2.4500	23.285	−20.51	0.250	yes
53.144489	−27.728071	2.2760	24.519	−19.73	0.115	no
53.145431	−27.698008	2.3129	23.781	−21.00	−0.015	no
53.145621	−27.685249	2.7708	24.084	−21.09	0.121	no
53.149223	−27.748588	2.5658	23.770	−21.27	−0.036	no
53.149815	−27.697213	3.6180	23.903	−21.83	0.315	no
53.151291	−27.742911	3.4173	23.943	−21.44	0.426	no
53.157430	−27.709016	2.9752	23.636	−21.57	0.219	no
53.158912	−27.742675	2.3277	22.417	−21.19	0.230	no
53.161953	−27.722657	2.4490	23.563	−21.10	0.087	no
53.167996	−27.711349	2.5845	23.776	−21.14	0.064	no
53.168265	−27.741939	4.1200	25.013	−21.11	0.490	no
53.174442	−27.733297	2.5760	24.139	−19.99	0.235	yes
53.181805	−27.729920	2.3168	23.211	−20.77	0.136	no
53.182798	−27.705269	2.3682	24.187	−21.02	−0.092	no
53.182838	−27.734909	2.4284	22.744	−20.89	0.316	no

Note.
[a] From Hsieh et al. (2012).

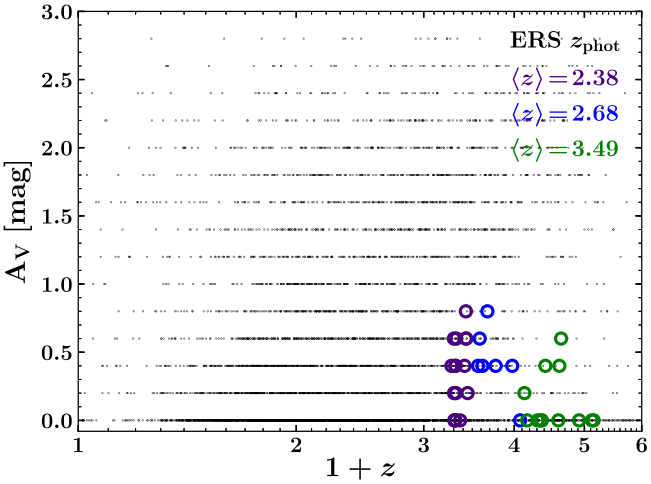

Figure 17. Distribution of dust extinction A_V values from best fit Calzetti et al. (2000) dust-attenuated BC03 SEDs for all galaxies in the 10-band ERS data (black dots), compared to the spectroscopic samples used for the stacks in the three indicated redshift bins (colored open circles for galaxies).

must adopt the best available dust attenuation models for galaxies with accurate redshifts and no contaminating AGN signatures when performing the minimized χ^2 stellar SED fits that results in the most likely A_V values from the observed panchromatic ERS data. From SED fitting of Calzetti et al. (2000) attenuated BC03 models using the 10-band WFC3 +ACS photometry of all ∼6900 galaxies at $2 \lesssim z \lesssim 6$ within the GOODS-S ERS field (Windhorst & Cohen 2010; W11, see also Section 5.1), we find that most ERS galaxies have $0.0 \lesssim A_V \lesssim 1.0$ mag.

Figure 17 shows the distribution of dust extinction A_V values from best fit SEDs for all galaxies in the 10-band ERS data (small black dots), compared to our spectroscopic sample in the four indicated redshift bins. The SED fitting sampled the A_V parameter space in 0.2 mag intervals. Table 3 lists the $A_V^{\rm med}$ values and their $\pm 1\sigma$ ranges a function of redshift.

Figure 17 shows that the A_V values of our galaxy sample listed in Table 6 are consistent with those found for the entire ERS sample of 6900 galaxies with 10-band fitted photometric redshifts to $m_{\rm AB} \lesssim 27$ mag. This implies that our galaxies *are* sampling the available parameter space of A_V values *at their approximate redshifts*. Since the A_V uncertainty in the SED fits is unknown, the MC simulated $f_{\rm esc}^{\rm abs}$ values in Sections 5.1 and 5.2 do not include an A_V uncertainty, even though they utilize the extinction-corrected (intrinsic) SEDs. This implicit A_V error is one of the dominant errors in the $f_{\rm esc}^{\rm abs}$ calculation, but is less important than the IGM transmission variations in the MC-derived $f_{\rm esc}$ values (see Sections 5.2 and 5.3). We also note that there may exist a degeneracy between the A_V values and the ages of the best fit SEDs, which would also add to the uncertainty of the A_V values. The A_V induced error can be as large as the combined uncertainty of the photometric observations that we fit, and can further increase the overall uncertainty of the SED fit. Furthermore, the error in R_V derived by Calzetti et al. (2000) ($R_V = 4.05 \pm 0.80$) is not propagated into the SED fit, which would also increase the A_V error. However, the uncertainty in IGM transmission, which is primarily due to variations in sight lines and redshifts in the stacks (see Inoue & Iwata 2008), dominates the error in the MC $f_{\rm esc}$ values, and so an additional A_V error would only slightly increase their $\pm 1\sigma$ values, as discussed in Section 5.2 and Table 3.

Table 3 also shows that $A_V^{\rm med}$, for the samples with spectroscopic redshifts, increases from ∼0 mag at $z \simeq 3.1$–4.1 to ∼0.4 mag at $z \simeq 2.3$–3, consistent with the behavior seen in the entire ERS sample as a gradual increase in reddening toward the lower redshifts, when the stellar populations have aged more and produced more dust over cosmic time. Hence, the median A_V values and their rms for galaxies appears to increase at the lower redshifts.

D.2. LyC and UVC Surface Brightness Model Details

For the UVC and LyC SB models in Section 5.5 and Figure 12, we generate the UVC surface brightness as following:

$$SB_{\rm UVC}(b) = \int_{-\infty}^{\infty} ds\ \epsilon_{\rm UVC}(b, s). \tag{10}$$

where b denotes the impact parameter, s denotes the line of sight coordinate, and $\epsilon_{\rm UVC}(b, s)$ denotes the emission rate of UVC photons per unit volume at (b,s). The distance from the galaxy r is defined as $r = \sqrt{b^2 + s^2}$ (note that $2rdr = 2sds$ and $ds = \frac{r}{s}dr = \frac{r}{\sqrt{r^2 - b^2}}dr$, since $r^2 = s^2 + b^2$). We then obtain the LyC surface brightness from:

$$SB_{\rm LyC}(b) = \int_{-\infty}^{\infty} ds\ \epsilon_{\rm UVC}(b, s) \frac{f_{\rm LyC}}{f_{\rm UVC}} f_{\rm esc}(b, s). \tag{11}$$

where $f_{\rm esc}(b, s)$ denotes the fraction of LyC photons that can escape from (b,s), and the factor $\frac{f_{\rm LyC}}{f_{\rm UVC}}$ simply rescales the flux at UVC frequencies to that at LyC.

In our model of a clumpy ISM, $f_{\rm c}(r)$ denotes *the number of self-shielding clumps per unit length at r* (see Dijkstra & Kramer 2012). We therefore find that $f_{\rm c}(r)dr$ denotes the number of self-shielding clumps along a differential length dr. We assume that each clump is optically thick to ionizing photons. In this case, the escape fraction from (b, s) is simply the probability of finding *at least* one clump on a sight line to (b, s), $P_{\rm clump}(b, s)$, which is given by:

$$P_{\rm clump}(b, s) = 1 - P_{\rm no\ clump}(b, s) = 1 - \exp[-N_{\rm clump}(b, s)], \tag{12}$$

where, in the last step, we assumed that the number of clumps along a given line of sight follows a Poisson distribution with mean $N_{\rm clump}(b, s)$. This mean is given by:

$$N_{\rm clump}(b, s) = \int_{-\infty}^{s} ds' f_{\rm c}(b, s'). \tag{13}$$

ORCID iDs

Brent M. Smith https://orcid.org/0000-0002-0648-1699
Rogier A. Windhorst https://orcid.org/0000-0001-8156-6281
Rolf A. Jansen https://orcid.org/0000-0003-1268-5230
Linhua Jiang https://orcid.org/0000-0003-4176-6486
Anton M. Koekemoer https://orcid.org/0000-0002-6610-2048
Akio K. Inoue https://orcid.org/0000-0002-7779-8677
Robert W. O'Connell https://orcid.org/0000-0002-8190-7573
Joseph I. Silk https://orcid.org/0000-0002-1566-8148

References

Ade, P. A. R., Aghanim, N., Armitage-Caplan, C., et al. 2014, A&A, 571, A16
Aird, J., Coil, A. L., Georgakakis, A., et al. 2015, MNRAS, 451, 1892
Anderson, J., & Bedin, L. R. 2010, PASP, 122, 1035
Avila, R., Grogi, N., Anderson, J., et al. 2015, ACS Instrument Handbook v.14 (Baltimore, MD: STScI), http://www.stsci.edu/hst/acs/documents/handbooks/current/cover.html
Baggett, S., & Anderson, J. 2012, Instrument Science Report WFC3 2012-12 (Baltimore, MD: STSci)
Baggett, S., Brown, T., Boucarut, R., et al. 2006, Proc. SPIE, 6265, 626532
Balestra, I., Mainieri, V., Popesso, P., et al. 2010, A&A, 512, A12
Becker, G. D., & Bolton, J. S. 2013, MNRAS, 436, 1023
Becker, G. D., Bolton, J. S., Madau, P., et al. 2015, MNRAS, 447, 3402
Bekki, K. 2015, ApJ, 799, 166
Bergvall, N., Leitet, E., Zackrisson, E., & Marquart, T. 2013, A&A, 554, A38
Bergvall, N., Zackrisson, E., Andersson, B.-G., et al. 2006, A&A, 448, 513
Bertin, E., & Arnouts, S. 1996, A&AS, 117, 393
Bielby, R., Hill, M. D., Shanks, T., et al. 2013, MNRAS, 430, 425
Blanc, G. A., Adams, J. J., Gebhardt, K., et al. 2011, ApJ, 736, 31
Bland-Hawthorn, J., & Maloney, P. R. 1999, ApJL, 510, L33
Bohlin, R. C., Savage, B. D., & Drake, J. F. 1978, ApJ, 224, 132
Borthakur, S., Heckman, T. M., Leitherer, C., & Overzier, R. A. 2014, Sci, 346, 216
Botticella, M. T., Smartt, S. J., Kennicutt, R. C., et al. 2012, A&A, 537, A132
Bourque, M., & Kozhurina-Platais, V. 2013, Instrument Science Instrument Science Report WFC 2013-03 (Baltimore, MD: STScI)
Boutsia, K., Grazian, A., Giallongo, E., et al. 2011, ApJ, 736, 41
Bouwens, R. J., Illingworth, G. D., Oesch, P. A., et al. 2012, ApJL, 752, L5
Bridge, C. R., Teplitz, H. I., Siana, B., et al. 2010, ApJ, 720, 465
Bruzual, G., & Charlot, S. 2003, MNRAS, 344, 1000
Burgarella, D., Buat, V., Gruppioni, C., et al. 2013, A&A, 554, A70
Calzetti, D., Armus, L., Bohlin, R. C., et al. 2000, ApJ, 533, 682
Chen, H.-W., Prochaska, J. X., & Gnedin, N. Y. 2007, ApJL, 667, L125
Choudhury, T. R., Puchwein, E., Haehnelt, M. G., & Bolton, J. S. 2015, MNRAS, 452, 261
Clarke, C., & Oey, M. S. 2002, MNRAS, 337, 1299
Cooke, J., Ryan-Weber, E. V., Garel, T., & Diaz, C. G. 2014, MNRAS, 441, 837
Cowie, L. L., Barger, A. J., & Trouille, L. 2009, ApJ, 692, 1476
Cristiani, S., Appenzeller, I., Arnouts, S., et al. 2000, A&A, 359, 489
Croom, S. M., Richards, G. T., Shanks, T., et al. 2009, MNRAS, 399, 1755
Cucciati, O., Tresse, L., Ilbert, O., et al. 2012, A&A, 539, A31
de Barros, S., Vanzella, E., Amorín, R., et al. 2016, A&A, 585, A51
Deharveng, J.-M., Buat, V., Le Brun, V., et al. 2001, A&A, 375, 805
Dickinson, M., Giavalisco, M. & GOODS Team 2003, in ESO Astrophysics Symp. The Mass of Galaxies at Low and High Redshift, ed. R. Bender & A. Renzini (Berlin: Springer), 324
Dijkstra, M., Haiman, Z., & Loeb, A. 2004, ApJ, 613, 646
Dijkstra, M., & Kramer, R. 2012, MNRAS, 424, 1672
Dijkstra, M., Mesinger, A., & Wyithe, J. S. B. 2011, MNRAS, 414, 2139
Dijkstra, M., Wyithe, S., Haiman, Z., Mesinger, A., & Pentericci, L. 2014, MNRAS, 440, 3309
Dove, J. B., Shull, J. M., & Ferrara, A. 2000, ApJ, 531, 846
Dressel, L., Balick, B., Baggett, S., et al. 2015, Wide Field Camera 3 Instrument Handbook v.7 (Baltimore, MD: STScI), http://www.stsci.edu/hst/wfc3/documents/handbooks/currentIHB/
Driver, S. P., Andrews, S. K., Davies, L. J., et al. 2016, ApJ, 827, 108
Driver, S. P., Fernández-Soto, A., Couch, W. J., et al. 1998, ApJL, 496, L93
Ebrero, J., Carrera, F. J., Page, M. J., et al. 2009, A&A, 493, 55
Fan, X., Carilli, C., & Keating, B. 2006a, ARA&A, 44, 415
Fan, X., Narayanan, V. K., Strauss, M. A., et al. 2002, AJ, 123, 1247
Fan, X., Strauss, M. A., Richards, G. T., et al. 2006b, AJ, 131, 1203
FaucherGiguère, C., Lidz, A., Hernquist, L., & Zaldarriaga, M. 2008, ApJ, 688, 85
Ferguson, A. M. N., Wyse, R. F. G., Gallagher, J. S. I., & Hunter, D. A. 1996, AJ, 111, 2265
Ferguson, H. C. 2001, in Proc. ESO Workshop, Deep Fields, ed. S. Cristiani, A. Renzini, & R. E. Williams (Berlin: Springer), 54
Fernandez, E. R., & Shull, J. M. 2011, ApJ, 731, 20
Fernández-Soto, A., Lanzetta, K. M., & Chen, H.-W. 2003, MNRAS, 342, 1215
Finkelstein, S. L., Ryan, R. E., Jr., Papovich, C., et al. 2015, ApJ, 810, 71
Finlator, K., Oh, S. P., Özel, F., & Davé, R. 2012, MNRAS, 427, 2464
Fiore, F., Puccetti, S., Grazian, A., et al. 2011, A&A, 537, A16
Fiore, F., Puccetti, S., Grazian, A., et al. 2012, A&A, 537, A16
Fitzpatrick, E. L. 1999, PASP, 111, 63
Fontanot, F., Cristiani, S., Monaco, P., et al. 2007, A&A, 461, 39
Forbes, J. C., Krumholz, M. R., Goldbaum, N. J., & Dekel, A. 2016, Natur, 535, 523
Freedman, D., & Diaconis, P. 1981, Z. Wahrscheinlichkeitstheor. Verwandte Geb., 57, 453
Fruchter, A. S., Hack, W., Dencheva, N., Droettboom, M., & Greenfield, P. 2010, in Space Telescope Science Institute Calibration Workshop, ed. S. Deustua & C. Oliveira (Baltimore, MD: STSci), 382
Fujita, A., Martin, C. L., Mac Low, M., & Abel, T. 2003, ApJ, 599, 50
Fynbo, J. P. U., Jakobsson, P., Prochaska, J. X., et al. 2009, ApJS, 185, 526
Gardner, J. P., Mather, J. C., Clampin, M., et al. 2006, SSRv, 123, 485
Giallongo, E., Cristiani, S., D'Odorico, S., & Fontana, A. 2002, ApJL, 568, L9
Giavalisco, M., Ferguson, H. C., Koekemoer, A. M., et al. 2004, ApJL, 600, L93
Glikman, E., Djorgovski, S. G., Stern, D., et al. 2011, ApJL, 728, L26
Gnedin, N. Y. 2000, ApJ, 535, 530
Gonzaga, S., Hack, W., Fruchter, A., & Mack, J. 2012, The DrizzlePac Handbook (Baltimore, MD: STScI)
Grazian, A., Giallongo, E., Gerbasi, R., et al. 2016, A&A, 585, A48
Grimes, J. P., Heckman, T., Aloisi, A., et al. 2009, ApJS, 181, 272
Grimes, J. P., Heckman, T., Strickland, D., et al. 2007, ApJ, 668, 891
Grogin, N. A., Kocevski, D. D., Faber, S. M., et al. 2011, ApJS, 197, 35
Guaita, L., Pentericci, L., Grazian, A., et al. 2016, A&A, 587, A133
Guo, Y., Ferguson, H. C., Giavalisco, M., et al. 2013, ApJS, 207, 24
Haardt, F., & Madau, P. 1996, ApJ, 461, 20
Haardt, F., & Madau, P. 2012, ApJ, 746, 125
Haardt, F., & Maraschi, L. 1993, ApJ, 413, 507
Hanish, D. J., Oey, M. S., Rigby, J. R., de Mello, D. F., & Lee, J. C. 2010, ApJ, 725, 2029
Hathi, N. P., Jansen, R. A., Windhorst, R. A., et al. 2008, AJ, 135, 156
Hathi, N. P., Ryan, R. E., Cohen, S. H., et al. 2010, ApJ, 720, 1708
Heckman, T. M., Sembach, K. R., Meurer, G. R., et al. 2001, ApJ, 558, 56
Hinshaw, G., Larson, D., Komatsu, E., et al. 2013, ApJS, 208, 19
Hopkins, P. F., Somerville, R. S., Hernquist, L., et al. 2006, ApJ, 652, 864
Hsieh, B.-C., Wang, W.-H., Hsieh, C.-C., et al. 2012, ApJS, 203, 23
Hurwitz, M., Jelinsky, P., & Dixon, W. V. D. 1997, ApJL, 481, L31
Ikeda, H., Nagao, T., Matsuoka, K., et al. 2011, ApJL, 728, L25
Ikeda, H., Nagao, T., & Matsuoka, K. 2012, ApJ, 756, 160
Inoue, A. K. 2001, AJ, 122, 1788
Inoue, A. K., Hirashita, H., & Kamaya, H. 2001, ApJ, 555, 613
Inoue, A. K., & Iwata, I. 2008, MNRAS, 387, 1681
Inoue, A. K., Iwata, I., & Deharveng, J.-M. 2006, MNRAS, 371, L1
Inoue, A. K., Iwata, I., Deharveng, J.-M., Buat, V., & Burgarella, D. 2005, A&A, 435, 471
Inoue, A. K., Shimizu, I., Iwata, I., & Tanaka, M. 2014, MNRAS, 442, 1805
Ishigaki, M., Kawamata, R., Ouchi, M., et al. 2015, ApJ, 799, 12
Iwata, I., Inoue, A. K., Matsuda, Y., et al. 2009, ApJ, 692, 1287
Izotov, Y. I., Orlitova, I., Schaerer, D., et al. 2016, Nature, 529, 178
Jensen, H., Laursen, P., Mellema, G., et al. 2012, MNRAS, 428, 1366
Khaire, V., Srianand, R., Choudhury, T. R., & Gaikwad, P. 2016, MNRAS, 457, 4051
Koekemoer, A. M., Ellis, R. S., McLure, R. J., et al. 2013, ApJS, 209, 3
Koekemoer, A. M., Faber, S. M., Ferguson, H. C., et al. 2011, ApJS, 197, 36
Kozhurina-Platais, V. 2014, Instrument Science Report WFC 2014-12 (Baltimore, MD: STScI)
Kozhurina-Platais, V., Cox, C., McLean, B., et al. 2009, Instrument Science Report WFC3 2009-33 (Baltimore, MD: STScI)
Kozhurina-Platais, V., Hammer, D., Dencheva, N., & Hack, W. 2013, Instrument Science Report WFC 2013-14 (Baltimore, MD: STScI)
Krumholz, M. R., & Dekel, A. 2012, ApJ, 753, 16
Kuhlen, M., & Faucher-Giguère, C.-A. 2012, MNRAS, 423, 862
Kulkarni, G., Hennawi, J. F., Rollinde, E., & Vangioni, E. 2014, ApJ, 787, 64
Kurk, J., Cimatti, A., Daddi, E., et al. 2012, A&A, 549, A63
Le Fèvre, O., Tasca, L. A. M., Cassata, P., et al. 2015, A&A, 576, A79
Le Fèvre, O., Vettolani, G., Paltani, S., et al. 2004, A&A, 428, 1043
Leitet, E., Bergvall, N., Hayes, M., Linné, S., & Zackrisson, E. 2013, A&A, 553, A106
Leitet, E., Bergvall, N., Piskunov, N., & Andersson, B.-G. 2011, A&A, 532, A107
Leitherer, C., Ferguson, H. C., Heckman, T. M., & Lowenthal, J. D. 1995, ApJL, 454, L19
Leitherer, C., Vacca, W. D., Conti, P. S., et al. 1996, ApJ, 465, 717
Lilly, S., Schade, D., Ellis, R., et al. 1998, ApJ, 500, 75
Loeb, A., & Barkana, R. 2001, ARA&A, 39, 19
Lusso, E., Worseck, G., Hennawi, J. F., et al. 2015, MNRAS, 449, 4204

Mack, J., Sabbi, E., & Dahlen, T. 2013, Instrument Science Report WFC3 2013-10 (Baltimore, MD: STScI), http://adsabs.harvard.edu/abs/2013wfc..rept...10M
Madau, P., Ferguson, H. C., Dickinson, M. E., et al. 1996, MNRAS, 283, 1388
Madau, P., & Haardt, F. 2015, ApJL, 813, L8
Madau, P., Rees, M. J., Volonteri, M., Haardt, F., & Oh, S. P. 2004, ApJ, 604, 484
Malkan, M., Webb, W., & Konopacky, Q. 2003, ApJ, 598, 878
Mallén-Ornelas, G., Lilly, S. J., Crampton, D., & Schade, D. 1999, ApJL, 518, L83
Massey, R., Schrabback, T., Cordes, O., et al. 2014, MNRAS, 439, 887
Masters, D., Capak, P., Salvato, M., et al. 2012, ApJ, 755, 169
Mathis, J. S. 1971, ApJ, 167, 261
Mathis, J. S. 1990, ARA&A, 28, 37
McGreer, I. D., Mesinger, A., & D'Odorico, V. 2014, MNRAS, 447, 499
Mesinger, A., Aykutalp, A., Vanzella, E., et al. 2014, MNRAS, 446, 566
Mesinger, A., & Haiman, Z. 2004, ApJL, 611, L69
Miller, N. A., Bonzini, M., Fomalont, E. B., et al. 2013, ApJS, 205, 13
Mirabel, I. F., Dijkstra, M., Laurent, P., Loeb, A., & Pritchard, J. R. 2011, A&A, 528, A149
MiraldaEscudé, J., Haehnelt, M., & Rees, M. J. 2000, ApJ, 530, 1
Momcheva, I. G., Brammer, G. B., van Dokkum, P. G., et al. 2016, ApJS, 225, 27
Moos, H. W., Cash, W. C., Cowie, L. L., et al. 2000, ApJL, 538, L1
Mostardi, R. E., Shapley, A. E., Nestor, D. B., et al. 2013, ApJ, 779, 65
Mostardi, R. E., Shapley, A. E., Steidel, C. C., et al. 2015, ApJ, 810, 107
Nestor, D. B., Shapley, A. E., Kornei, K. A., Steidel, C. C., & Siana, B. 2013, ApJ, 765, 47
Nestor, D. B., Shapley, A. E., Steidel, C. C., & Siana, B. 2011, ApJ, 736, 18
Noeske, K., Baggett, S., Bushouse, H., et al. 2012, Instrument Science Report WFC3 2012-09 (Baltimore, MD: STScI)
Oey, M., & Kennicutt, R. C. J. 1997, MNRAS, 291, 827
Oke, J. B., & Gunn, J. E. 1983, ApJ, 266, 713
Ouchi, M., Mobasher, B., Shimasaku, K., et al. 2009, ApJ, 706, 1136
Planck Collaboration, Ade, P. A. R., Aghanim, N., et al. 2016, A&A, 594, A13
Popesso, P., Dickinson, M., Nonino, M., et al. 2009, A&A, 494, 443
Putman, M. E., BlandHawthorn, J., Veilleux, S., et al. 2003, ApJ, 597, 948
Rachford, B. L., Snow, T. P., Tumlinson, J., et al. 2002, ApJ, 577, 221
Rafelski, M., Teplitz, H. I., Gardner, J. P., et al. 2015, AJ, 150, 31
Rangel, C., Nandra, K., Laird, E. S., & Orange, P. 2013, MNRAS, 428, 3089
Rauch, M., Becker, G. D., Haehnelt, M. G., et al. 2011, MNRAS, 418, 1115
Razoumov, A. O., & Sommer-Larsen, J. 2007, ApJ, 668, 674
Razoumov, A. O., & Sommer-Larsen, J. 2010, ApJ, 710, 1239
Reddy, N. A., & Steidel, C. C. 2009, ApJ, 692, 778
Reunanen, J., Kotilainen, J. K., & Prieto, M. A. 2003, MNRAS, 343, 192
Richings, A. J., Schaye, J., & Oppenheimer, B. D. 2014, MNRAS, 442, 2780
Ricotti, M. 2002, MNRAS, 336, L33
Ricotti, M., & Shull, J. M. 2000, ApJ, 542, 548
Robertson, B. E., Furlanetto, S. R., Schneider, E., et al. 2013, ApJ, 768, 71
Rutkowski, M. J., Scarlata, C., Haardt, F., et al. 2016, ApJ, 819, 81
Sabbi, E. 2009, Instrument Science Report WFC3 2009-19 (Baltimore, MD: STScI)
Salpeter, E. E. 1955, ApJ, 121, 161
Sandberg, A., Östlin, G., Melinder, J., Bik, A., & Guaita, L. 2015, ApJL, 815, L10
Schroeder, J., Mesinger, A., & Haiman, Z. 2012, MNRAS, 428, 3058
Scott, J. E., Kriss, G. A., Brotherton, M., et al. 2004, ApJ, 615, 135
Shapley, A. E., Steidel, C. C., Pettini, M., & Adelberger, K. L. 2003, ApJ, 588, 65
Shapley, A. E., Steidel, C. C., Pettini, M., Adelberger, K. L., & Erb, D. K. 2006, ApJ, 651, 688
Shull, J. M., Stevans, M., & Danforth, C. W. 2012, ApJ, 752, 162
Siana, B., Shapley, A. E., Kulas, K. R., et al. 2015, ApJ, 804, 17
Siana, B., Teplitz, H. I., Colbert, J., et al. 2007, ApJ, 668, 62
Siana, B., Teplitz, H. I., Ferguson, H. C., et al. 2010, ApJ, 723, 241
Silk, J. 2005, MNRAS, 364, 1337
Silk, J., & Norman, C. 2009, ApJ, 700, 262
Silverman, J. D., Green, P. J., Barkhouse, W. A., et al. 2008, ApJ, 679, 118
Silverman, J. D., Mainieri, V., Salvato, M., et al. 2010, ApJS, 191, 124
Skelton, R. E., Whitaker, K. E., Momcheva, I. G., et al. 2014, ApJS, 214, 24
Springel, V., Di Matteo, T., & Hernquist, L. 2005, MNRAS, 361, 776
Steidel, C. C., Pettini, M., & Adelberger, K. L. 2001, ApJ, 546, 665
Sternberg, A., McKee, C. F., & Wolfire, M. G. 2002, ApJS, 143, 419
Szalay, A. S., Connolly, A. J., & Szokoly, G. P. 1999, AJ, 117, 68
Szokoly, G. P., Bergeron, J., Hasinger, G., et al. 2004, ApJS, 155, 271
Tasca, L. A. M., Le Fèvre, O., Ribeiro, B., et al. 2017, A&A, 600, A110
Telfer, R. C., Zheng, W., Kriss, G. A., & Davidsen, A. F. 2002, ApJ, 565, 773
Teplitz, H. I., Rafelski, M., Kurczynski, P., et al. 2013, AJ, 146, 159
Tumlinson, J., Giroux, M. L., Shull, J. M., & Stocke, J. T. 1999, AJ, 118, 2148
van de Voort, F., Schaye, J., Altay, G., & Theuns, T. 2012, MNRAS, 421, 2809
Vanden Berk, D. E., Richards, G. T., Bauer, A., et al. 2001, AJ, 122, 549
Vanzella, E., Cristiani, S., Dickinson, M., et al. 2008, A&A, 478, 83
Vanzella, E., de Barros, S., Castellano, M., et al. 2015, A&A, 576, A116
Vanzella, E., Giavalisco, M., Inoue, A. K., et al. 2010a, ApJ, 725, 1011
Vanzella, E., Guo, Y., Giavalisco, M., et al. 2012, ApJ, 751, 70
Vanzella, E., Siana, B., Cristiani, S., & Nonino, M. 2010b, MNRAS, 404, 1672
Wilkins, S. M., Bunker, A. J., Lorenzoni, S., & Caruana, J. 2011, MNRAS, 411, 23
Willott, C. J., Delorme, P., Reylé, C., et al. 2010, AJ, 139, 906
Windhorst, R. A., & Cohen, S. H. 2010, in AIP Conf. Ser. 1294 First Stars and Galaxies: Challenges for the Next Decade, ed. D. J. Whalen, V. Bromm, & N. Yoshida (Melville, NY: AIP), 225
Windhorst, R. A., Cohen, S. H., Hathi, N. P., et al. 2011, ApJS, 193, 27
Windhorst, R. A., Keel, W. C., & Pascarelle, S. M. 1998, ApJL, 494, L27
Wise, J. H., & Cen, R. 2009, ApJ, 693, 984
Wise, J. H., Demchenko, V. G., Halicek, M. T., et al. 2014, MNRAS, 442, 2560
Wolf, C., Meisenheimer, K., Kleinheinrich, M., et al. 2004, A&A, 421, 913
Worseck, G., Prochaska, J. X., Hennawi, J. F., & McQuinn, M. 2016, ApJ, 825, 144
Wuyts, S., van Dokkum, P. G., Franx, M., et al. 2009, ApJ, 706, 885
Wyithe, J. S. B., Hopkins, A. M., Kistler, M. D., Yüksel, H., & Beacom, J. F. 2010, MNRAS, 401, 2561
Xue, Y. Q., Luo, B., Brandt, W. N., et al. 2011, ApJS, 195, 10
Xue, Y. Q., Luo, B., Brandt, W. N., et al. 2016, ApJS, 224, 15
Yajima, H., Choi, J.-H., & Nagamine, K. 2011, MNRAS, 412, 411
Zurita, A., Beckman, J. E., Rozas, M., & Ryder, S. 2002, A&A, 386, 801